Understanding 21st Century Hydroclimatic Trends in Western USA Mountain Ranges using Variable-Resolution CESM

By

ALAN MICHAEL RHOADES

B.S. (California State University, Chico) 2012

DISSERTATION

Submitted in partial satisfaction of the requirements for the degree of

DOCTOR OF PHILOSOPHY

in

Atmospheric Science

in the

OFFICE OF GRADUATE STUDIES

of the

UNIVERSITY OF CALIFORNIA

DAVIS

Approved:

_____

Dr. Paul Ullrich, Chair

_____

Dr. Kyaw Tha Paw U

_____

Dr. Sebastian Vicuña

Committee in Charge
2017

i

Doctoral Committee:

      Dr. Paul Ullrich, Chair

      Dr. Christopher Cappa

      Dr. Travis O'Brien

      Dr. Kyaw Tha Paw U

      Dr. Sebastian Vicuña

For Grandma and Grandpa and all those that have supported me.

"It is all really there. That is what really gets you. But you gotta stop and think about it to really get the pleasure about the complexity, the inconceivable nature of nature."
-Richard Feynman

Acknowledgements

Table of Contents

Alan Michael Rhoades

June 2017

Atmospheric Science

Understanding 21st Century Hydroclimatic Trends in Western USA Mountain Ranges using Variable-Resolution CESM

Abstract

Mountains have historically functioned as both natural dams and water towers as they block atmospheric moisture transport and store it in the form of snowpack. They are also unique natural sentinels of climate change with high susceptibility to fluctuations in radiation, surface temperature, and moisture concentrations. The nonlinear atmosphere-land interactions between the major mountain hydroclimate variables such as snowfall, snow cover, snow water equivalent, and surface temperature determine the ebb and flow of how mountains naturally manage water resources. Snowfall totals are representative of the storm composition, orographic forcing, and, ultimately, the initial placement of snow in mountains. Snow cover represents the areal extent of snowfall deposition and the modifications in radiative surface properties. Snow water equivalent is a measure of the vertical build-up of water over the snow covered area that can be stored and slowly released over a given time period. Finally, surface temperature regulates the total storage and release time of mountains in their role as natural reservoirs.

Thus, as anthropogenic climate change modifies nonlinear feedbacks at various elevation bands in mountain environments, a physically based model with dynamic feedbacks between the large-scale atmosphere drivers and regional-scale land surface processes is necessary to understand both historical and future trends in mountain hydroclimatology. To address this my research advances the use of a new modeling tool known as variable-resolution in the Community Earth System Model (VR-CESM) to better understand the historical evolution and potential climate change effects on the mountain hydroclimatology of California and the broader western USA, with a particular focus on snowpack. My dissertation represents the first application of this technique to explore scientific questions associated with mountain hydroclimatology and utilizes a suite of climate model,

observational, and reanalysis datasets to provide a comprehensive assessment of how western US water resources has and will continue to be shaped by climate change. This research topic sits at the boundary of the atmospheric, hydrologic and computer sciences with an overall goal to push the boundaries of both global climate modeling and regional climate modeling.

Chapter 1 explores the usability of VR-CESM in hydroclimate applications by assessing its relative performance to a suite of model, observational, and reanalysis datasets to represent historical snowpack life cycles and snow cover extents in the California Sierra Nevada. Chapter 2 utilizes VR-CESM to explore the effects of a "business-as-usual" climate change scenario on mountain hydroclimatological trends within the five major western US mountain ranges and explored the nonlinear feedbacks with elevation. Chapter 3 identifies the relative effects of horizontal grid refinement and sub-grid-scale physics in VR-CESM to understand what controls simulated precipitation, snowpack, and surface temperature trends and what systemic biases need to be addressed.

Introduction

The 21st century will continue to see unprecedented changes to the climate system associated with anthropogenic influence. Presently, climate system processes are most confidently attributed by the Intergovernmental Panel on Climate Change (IPCC) at global scales, however this does not necessarily translate to regional scales where most management and policy decisions are made (Field et al, 2014). Therefore, the scientific understanding of changes to the regional climate is an ongoing and pressing challenge. This challenge arises from the cascade of interactions that occur from the global-to-regional scale. To work across this multi-scale space, the climate modeling community has largely worked within one of two scientific paradigms, global climate modeling and regional climate modeling. Each presents unique benefits as well as major physical assumptions, computer hardware limitations and model biases when applied to work across the multitude of scales present in the climate system. Recent research has sought to push the boundaries of both global climate modeling and regional climate modeling via a recently developed approach known as variable-resolution global climate models (VRGCMs).

VRGCMs offer a new modeling platform that can work across the global-to-regional model divide and in a much more computationally efficient way than conventional global climate modeling techniques. By utilizing a globally coarse resolution grid which is only refined over a specific area of interest, these models often require only 10% of the computing power of uniform resolution global climate models to resolve fine-scale features. This allows today's supercomputing platforms to be leveraged to their fullest extent and affords a means by which model biases can be explored and remediated at resolutions not yet capable with conventional global modeling strategies. For example, a simple doubling of horizontal resolution from 111km (typical resolution) to 55km (current cutting-edge resolutions) would result in a computational demand eight times larger than the original model due to a halving of every GCM's grid cell in both horizontal directions and decreasing the model time step by half, to prevent numerical instability. This does not include a potential increase in grid cell resolution in the vertical which would add another factor of two to computational demand nor the cost associated with incorporating newly discovered climate processes. Thus, VRGCMs afford us with: a glimpse into the future of global climate modeling at a fraction

of the cost of conventional GCMs, more usable regional scale information for climate adaptation needs, and a climate model that will be scale-aware across a myriad of resolutions.

Over the last five years, several variable-resolution (VR) strategies have been developed and incorporated into atmospheric model dynamical cores that utilize hydrostatic and/or nonhydrostatic fluid equations and in which VR mesh refinement can be static or dynamic. Some examples of VR capable models include the work by Skamarock et al (2012) using the Model for Predication Across Scales (MPAS - nonhydrostatic and static mesh), the work by Harris and Lin (2013) using the Finite-Volume Cubed-Sphere Dynamical Core (FV3 - hydrostatic/nonhydrostatic and static mesh), the capability of VR in the Community Earth System Model (VR-CESM - hydrostatic and static mesh) presented in this dissertation and by Zarzycki et al (2014b), and, most recently, the experimental adaptive mesh refinement (AMR) dynamical core Chombo-AMR (nonhydrostatic and dynamic mesh) highlighted by the work of Park et al (2014b). Each VR enabled dynamical core presents a unique spin on how to formulate grid element shapes, discretize the equations of motion, and handle the unresolved processes at the sub-grid-scale. A detailed explanation of the VR-CESM dynamical core, grid, and sub-grid-scale parameterizations are discussed in greater detail within the Appendix. VRGCMs are only now being put to use, leading to Earth system models which both correctly capture regional-global interactions and reach the resolutions needed to understand regional climate change. Thus, VRGCMs have now progressed to the point where they can be vetted and used for applied research.

The western US is a unique scientific testbed to explore the utility of VRGCMs to work across the global-to-regional divide. The precipitation trends in the region are shaped by large-scale systems that originate from the Aleutian Gulf and warm, extreme and intermittent systems from the equator. Coupled with this, precipitation is closely connected with orography where the storm's location of landfall, perpendicularity to the topography, mountain upslope velocities, and integrated water vapor flux are crucial in determining the amount of seasonal snowpack that will be stored. Mountain snowpack storage is critical for water use in agricultural, environmental, and municipal sectors as half of all annual precipitation comes in 5-15 days (Dettinger et al, 2011), usually within a window of only a few months each year and where extreme storms (or atmospheric rivers) contribute

40% of mountain snowpack storage (Guan et al, 2013). To exacerbate the seasonal timing issue, climate change has and will continue to directly impact mountain snowpack via three physical drivers. First, warming temperatures lead to an earlier spring thaw, increasing runoff associated with spring melt and decreasing late summer water availability due to early depletion of snowpack. Second, according to the Clausius-Clapeyron equation, warmer air has the potential for higher concentrations of water vapor leading to possible increases in large-scale precipitation in areas with forced orographic uplift (e.g., mountain ranges of the western USA), although warmer temperatures also tend to favor rainfall over snowfall. This is of importance to the western US where Bales et al (2006) observed that 20-40% of precipitation events occur when surface temperatures are at or around freezing (-3 to 0 °C) and thus snowfall is more susceptible to projected regional warming (National Climate Assessment, accessed 2016). This is especially relevant for the leeward (eastern) portion of the Sierra Nevada where it has been shown that an increase of 6 °C would threaten most of the accumulated southern Sierra Nevada snowpack (even up to 3000 m) and a 2 °C could shorten the snow season by a full month, which is on the order of historical interannual variability (Bales et al, 2014). Furthermore, rising surface temperatures are particularly important in the spring months at mid- to high-elevations, which would normally be below freezing throughout the winter period (Cayan, 1996; Stewart, 2009). Last, the snow-albedo feedback, a process in which the freezing point threshold is augmented resulting in snow cover diminishment, plays a pivotal role in determining the local and/or global albedo (Hall, 2004; Qu and Hall, 2014). This is due to the radiative principle that as less solar radiation is reflected from snow (average shortwave albedo of 0.5 to 0.9 based on age), more shortwave radiation may be absorbed by bare soil/rock or vegetation and re-emitted as longwave radiation. The result could alter the local and/or global net radiative equilibrium (Anderson, 1976; Hall, 2004; Qu and Hall, 2014). Snow is a virtual blackbody in the longwave spectrum, therefore nonlinear cloud and moisture feedbacks could further diminish the resiliency of mountain snowpack in the future.

This dissertation explores the ability of a VRGCM model to represent the processes that shape mountain hydroclimatology, namely variable-resolution in the Community Earth System Model (VR-CESM). The focii of this dissertation are to explore the processes that shape mountain hydroclimatology in the western US, identify if the key-processes are effectively modeled within VR-

CESM, and, finally, understand how anthropogenic climate change may influence them in the future. Alan Rhoades was the primary author on all works and conducted the bulk of the work in relation to hypotheses generation, literature review, experimental setup, data acquisition, model simulation, data management, and in drafting of each manuscript. Paul Ullrich was the primary adviser and mentor on all works. In addition, his software suites allowed Alan to expedite and fine-tune his scientific methods. All other co-authors provided consistent commentary, technical guidance, and mentorship where needed via email and in-person meetings. Last, access to necessary computational resources were provided by several co-authors including Paul Ullrich, William Collins, Hans Johansen, and Colin Zarzycki.

Chapter 1 represents the first attempt at exploring the skill of VR-CESM in representing western US hydroclimatology at resolutions of 28km and 14km. The first goal is to evaluate historical (1980-2005) snowpack life cycles and snow cover extents in the California Sierra Nevada. The second goal is to identify model sensitivities to underlying topography, evaluate western US observational and reanalysis datasets, and assess VR-CESM performance against other widely used global and regional modeling techniques. A multitude of reanalysis and observational datasets, both spatially continuous and point-wise, are employed to explore model performance at climatological, seasonal, and daily climate temporal resolutions. The study is now published in the Journal of Applied Meteorology and Climatology under the DOI: http://dx.doi.org/10.1175/JAMC-D-15-0156.1.

Chapter 2 utilizes the best VR-CESM model representation from Chapter 1, considering both model efficacy and cost, to explore the effects of a "business-as-usual" climate change scenario (RCP8.5) on mountain hydroclimatological trends within the five major western US mountain ranges over the years 1980-2005 vs 2025-2100, with a particular focus on mountain snowpack. The changes in mid-century and end-century mountain snowpack tendencies are assessed and compared to other widely used climate change datasets over common historical and mid-century time frames to understand similarities and differences in the simulated climate change signal. Further analyses were conducted on VR-CESM results over 2025-2100 to understand how climate change may influence each mountain's climate average, seasonal variability, and elevational dependencies in precipitation, snowpack, and surface temperature. This work is now published in Climate Dynamics under the

Chapter 3 expands upon the VR-CESM sensitivities explored in Chapter 1 to assess the relative effects of horizontal grid refinement over the Sierra Nevada at 28km, 14km, 7km, and 3.5km to take advantage of the highest resolution surface datasets available and more realistically represent topography. Next, the effects of changing the sub-grid-scale physics that control precipitation from a standard diagnostic treatment to a new prognostic treatment at 28km and 14km over the Sierra Nevada was explored. Precipitation, snowpack, and surface temperature trends were assessed for the Sierra Nevada (total, windward, and leeward) to understand how VR-CESM resolution and sub-grid-scale physics changes the simulated climatological, seasonal, and daily climate trends across the six-member ensemble. Simulated differences in the magnitude, spatial correlation, elevation dependence, and windward/leeward distributions of each hydroclimate variable were highlighted and juxtaposed to several high-quality mountain hydroclimate datasets. Systemic bias associated with model resolution and/or sub-grid-scale microphysics were identified and hypothesized for future model development. The paper was submitted to the Journal of Hydrometeorology.

Chapter 1 - Characterizing Sierra Nevada Snowpack Using Variable-Resolution CESM

Abstract

The location, timing, and intermittency of precipitation in California makes the state integrally reliant on winter season snowpack accumulation to maintain its economic and agricultural livelihood. Of particular concern, winter season snowpack has shown a net decline across the western USA over the past 50 years resulting in a major uncertainty in water resource management heading into the next century. Cutting edge tools are available to help navigate and preemptively plan for these uncertainties. This paper uses a next-generation modeling technique, variable-resolution global climate modeling within the Community Earth System Model (VR-CESM), at horizontal resolutions of 0.125° (14km) and 0.25° (28km). VR-CESM provides means to include dynamically large-scale atmosphere-ocean drivers, limit model bias, provide more accurate representations of regional topography, while doing so in a more computationally efficient manner than conventional general circulation models. This paper validates VR-CESM at climatological and seasonal timescales for Sierra Nevada snowpack metrics by comparing them to the DAYMET, CAL-ADAPT, NARR, NCEP, and NLDAS reanalysis datasets, the MODIS remote sensing dataset, SNOTEL observational dataset, a standard practice global climate model (CESM) and regional climate model (WRF) dataset. Overall, considering California's complex terrain, intermittent precipitation, and that both of the VR-CESM simulations were only constrained by prescribed sea surface temperatures and sea ice extent data, a 0.68 centered Pearson product-moment correlation, negative mean SWE bias of <7 mm, interquartile range well within the values exhibited in the reanalysis datasets, and mean DJF SNOWC within 7% of the expected MODIS value, the efficacy of the VR-CESM framework is apparent.

Introduction

California receives half of its total annual precipitation in five to fifteen days of the year, making its precipitation patterns some of the most intermittent in the USA (Dettinger et al, 2011). Importantly, most of the state's precipitation falls during the winter months (December to February)

and two-thirds of it precipitates in the northern and mountainous parts of the state (Wise, 2012). The precipitation that falls in the mountainous region largely accumulates as snow (Pandey et al, 1999). Thus, winter snowpack acts as a natural surface reservoir for water that is then released during dry portions of the year. Snowpack provides approximately three-fourths of the annual fresh water supply in the western USA (Palmer, 1988; Cayan, 1996), and 60% of California's developed water supply originates from the snowpack dominated Sierra Nevada (Bales et al, 2011). Along with the Colorado River, this natural store of water contributes to the maintenance of California's economy and its stance as one of the largest agricultural providers in the world (Tanaka et al, 2006; Hanak and Lund, 2012). These water reserves also provide up to 21% of the energy found within California's diverse energy portfolio via hydroelectric plants (Stewart, 1996). Therefore, the integrity of California's economy, and agricultural identity, is largely dependent on ample snowpack accumulation in the Sierra Nevada.

A major cause of interannual variability in winter precipitation in California, and the greater western USA, are global teleconnections. Teleconnections are recurrent and persistent atmosphere-ocean patterns impacting large swaths of latitudinal and longitudinal bands (Wallace and Gutzler, 1981; Glantz et al, 1991). They are important from a water resources perspective because they determine overall temperature, precipitation, and snowpack trends within California. Atmosphere-ocean climate interactions have been found to vary annual precipitation by 20-45% in the western USA (Dettinger et al, 1998), and include the El Niño Southern Oscillation (ENSO), the Pacific Decadal Oscillation (PDO), the Pacific North American Pattern (PNA), the North American Monsoon, and the Aleutian Low, as well as more short term events known as atmospheric rivers (ARs) (i.e., equatorially generated whip-like water vapor bands) (Dettinger et al, 1998; Cayan et al, 1999; Ralph et al, 2004; Dettinger, 2011; Wise, 2012; Guan et al, 2013; Fang et al, 2014). The internal variability associated with teleconnections modulate the spatial and temporal variability of strong precipitation events in the western USA (Wise, 2012). Therefore, teleconnection modulation, on both yearly and decadal time frames, has a direct impact on the amount of total seasonal snowpack deposited in the Sierra Nevada. This modulation is also essential in resolving historical trends as well as projecting future snowpack tendencies. For example, atmospheric rivers alone account for around 30-40% of seasonal snowpack accumulation in the Sierra Nevada (Guan et al, 2010). Thus,

a representation of global processes, ideally via a global climate model, is necessary to accurately account for California's temperature, precipitation, and snowpack trends.

To observe how this crucial natural fresh water reserve is characterized, both spatially and temporally, snowpack metrics such as snow water equivalent (SWE), snow centroid date (SCD), and the extent of snow cover (SNOWC) have been developed to quantify the patterns of Sierra Nevada snowpack. SWE is used to determine the total water content for a given snow depth. It can be quantified by taking a given depth of snow and melting it; the resultant water content represents the SWE. This is useful since snow densities can fluctuate due to variations in snowfall as well as melt and ablation events in the snowpack. SCD represents the date of peak snowpack accumulation, which is useful in understanding snowmelt onset. SNOWC characterizes the total areal coverage of snow over a given region. This is helpful in quantifying shifts in regional to global albedo as well as the freezing line extent in mountainous environments. Over the historical record, the Sierra Nevada has shown a mean difference in April 1st SWE of 2.2% (i.e., northern Sierra decline of 50-75% and southern Sierra accumulation of 30%) (Mote et al, 2005), western USA SCD was found to shift 0.7 days earlier per decade (Kapnick and Hall, 2012), and total SNOWC declined by 9% across the Northern Hemisphere (Rupp et al, 2013). The shift in SCD appears to be eight days earlier per °C of warming in end of winter season (March and April) temperatures. Additionally, Bales et al (2006) found that the fraction of storms that occur with surface temperatures in the range of -3 °C to 0 °C account for up to 36% of the annual precipitation events in many parts of the Sierra Nevada, highlighting the sensitivity of snow storms in the Sierra Nevada to increasing temperatures due to anthropogenic global climate change. Using IPCC AR5 RCP 4.5 and 8.5 scenarios, projected end-of-the-century trends for snowpack highlight that western USA SWE may decline by 40-70% (Pierce and Cayan, 2013), snowfall may decrease by 25-40% (Pierce and Cayan, 2013), more winter storms may tend towards rain rather than snow (Bales et al, 2006), and relatively warmer storms (e.g., atmospheric rivers) may be more frequent and intense for California (Dettinger, 2011). In a review paper by Gimeno et al (2014), Dettinger et al (2011) represented the only western USA specific paper on the future projected trends of ARs. Of note, the authors expressed that the results in this study were a preliminary step and should be assessed more from a qualitative sense due to the small sample size of AR events in the CMIP5 archive and the various assumptions

associated with the relatively coarser temporal and spatial extents of the models in the CMIP5 archive. Therefore, if the aforementioned projected outcomes hold, mean precipitation is not expected to change dramatically, but interannual variability will likely increase through modulation in atmospheric river events. Since snowpack is affected by both precipitation and temperature, it is expected that increased end-of-century temperatures coupled with more intense warmer storms in the western USA will prevent snow accumulation and lead to changes in runoff timing that could be problematic for water management. Thus, an analysis of causal mechanisms of snowpack accumulation and snowmelt timing, with a dynamic inclusion of large-scale atmosphere-ocean drivers, and an accurate representation of the complex topography of California is needed to allow water managers to make more informative and preemptive decisions on Californias water future.

One key approach to address the aforementioned need is via climate models. However, both global and regional climate models have limitations in their predictive capacities. As demonstrated by the North American Regional Climate Change Assessment Program (NARCCAP), regional climate models (RCMs) were shown to produce too dry, too warm, and too little SWE conditions for the western USA and snow cover duration was found to start too late and end too early (Salzmann and Mearns, 2012). Model bias was associated with inadequate topography representation, imperfections in observational data, and differing land surface model components (Salzmann and Mearns, 2012). Similarly, Caldwell (2010) found that RCMs generally overpredict winter precipitation in California, whereas global climate models (GCMs) generally underpredict winter precipitation in California. The precipitation bias associated with GCMs was not solely related to model resolution (as this was standardized before comparison), but rather factors such as subgrid-scale parameterizations and coarse model topography too (Caldwell, 2010). The aforementioned RCM findings regarding precipitation and SWE appear contradictory to one another, but it should be noted that California hydroclimatic trends have shown dissimilarities from several of those shown in other parts of the western USA (Mote et al, 2005; Kapnick and Hall, 2012), likely due to a combination of relatively higher topographical elevation in the southern Sierra Nevada (compared to other western USA mountain ranges), proximity to the Pacific Ocean, and effects from ARs.

This paper aims to analyze the efficacy of variable-resolution modeling using the Community Earth

System Model (VR-CESM) at resolutions of 0.125° (14km) and 0.25° (28km) in representing Sierra Nevada snowpack, in comparison with observational, reanalysis and dynamically downscaled model results. Variable-resolution modeling is a novel tool for modeling the climate system and represents a hybrid of global and regional climate models. We envision that this new modeling framework will bring added value to the snowpack modeling community with the benefit of a global solution, accounting for major teleconnections, and regional high-resolution, better representation of winter storms and orographic forcings. This hypothesis has been corroborated for temperature and precipitation climatic trends within California in Huang et al (2016). These benefits will lead to a better representation of observed summary statistics for winter snowpack within a GCM framework. Further, several studies have shown that CESM has skill in representing the major wintertime teleconnections of the western USA including the ENSO (DeFlorio et al, 2013; Wang et al, 2014), the PDO (DeFlorio et al, 2013), and the Pacific-North American (PNA) pattern (Li and Forest, 2014). Teleconnection representation in these studies is expected to carry over into VR-CESM.

The structure of the remainder of the paper is as follows: Section 2 contains information about the CESM setup and experimental design, including VR-CESM grid implementation. Section 3 discusses the comparative datasets used to assess model efficacy. Section 4 provides summary statistic comparisons of seasonal to multidecadal snow trends, including SWE and SNOWC. Finally, section 5 provides further discussion and the conclusions of this study.

CESM Setup and VR-CESM Grid Implementation

CESM Setup

This project utilized version 1.2 of the Community Earth System Model (CESM), a widely used and community-supported climate model developed by the National Center for Atmospheric Research (NCAR) and the US Department of Energy (DoE). CESM is a fully coupled global climate model comprised of seven geophysical models that simulate the major components of the Earth system including the atmosphere, land-surface, land-ice, ocean, ocean-wave, river run-off and sea ice, all of which can be coupled dynamically. One of the F-component sets in CESM, FAMIPC5, is the standard protocol for the Atmospheric Model Intercomparison Project (AMIP) and was used for each of the CESM simulations in this study (Gates, 1992). This component set consists solely of the

atmosphere-land coupled model with prescribed sea-surface temperatures (SSTs) and sea ice extent. This limited configuration maximizes computational efficiency and inhibits model bias propagation. This is advantageous for a local server environment (<1000 processors per simulation), like the one used in this study. Although the oceanic and sea ice systems were not incorporated dynamically into this study, this component set ensures that interannual climate variability (mainly via SST anomalies) and global albedo effects from sea ice extent are incorporated into the simulations. Future research will target the VR-CESM simulation performance with and without a dynamic ocean model. Thus, for this study, only the atmosphere model (Community Atmosphere Model (CAM) version 5.3) (Neale et al, 2010) and the land-surface model (Community Land Model (CLM) version 4.0 with satellite phenology) (Oleson et al, 2010) were utilized.

CAM was run with the Spectral Element (SE) dynamical core with a cubed-sphere grid structure (Taylor et al, 1997; Dennis et al, 2012). CAM-SE uses a continuous Galerkin spectral finite-element method for solving the hydrostatic atmospheric primitive equations. CAM-SE provides several benefits over other CESM dynamical cores including linear scalability with increasing computer processor counts, machine precision conservation of mass and tracers, elimination of non-uniform grid spacings due to convergence zones at higher latitudes, and variable-resolution capabilities (Taylor and Fournier, 2010; Dennis et al, 2012; Zarzycki et al, 2014a,b; Zarzycki and Jablonowski, 2014). CAM5 physics are broken down into six main categories: shallow convection (Park and Bretherton, 2009), deep convection (Neale et al, 2008), microphysics (Morrison and Gettelman, 2008), macrophysics (Park et al, 2014a), radiation (Iacono et al, 2008), and aerosols (Ghan et al, 2012). Details on each of the physics schemes can be found in Neale et al (2010).

CLM subdivides each cell into land types such as glacier, lake, urban, vegetated, and wetland (Oleson et al, 2010; Lawrence et al, 2011). The vegetated component of the grid cell is further broken down into various soil types which are then characterized by 16 unique Plant Functional Types (PFTs), including non-vegetated. CLM4.0 PFTs include five evergreen species and six deciduous species for temperate, boreal, and tropical climates, three grasses for arctic and non-arctic climates (with C-3 and C-4 variations) and a few staple cereal crops. PFT cover is derived from the Moderate Resolution Imaging Spectroradiometer (MODIS) satellite data at $0.5°$ resolution

with canopy heights for each of the PFTs assumed to range from 0.5 meters (crops, grasses, and shrubs) to 35 meters (trees). PFT types and percent cover of PFTs within each vegetated land-unit play a crucial role in shaping snowpack trends. This is because the interaction between the canopy and snowpack are PFT specific for biogeochemical, radiative, and hydrological processes such as interception, throughfall, canopy drip, water removal via transpiration, and optical property interactions based on leaf angle and specific PFT (Lawrence et al, 2011).

The parameterizations of snowpack within CESM are based primarily on work done by Anderson (1976), Jordan (1991), and Yongjiu and Qingcun (1997). These parameterizations characterize several important state variables for snowpack including the mass of water, mass of ice, snowpack layer thickness, temperature profile of the snowpack layer, black carbon and mineral deposition, and snowpack aging and optical properties. The model is discretized using five snow layers with dynamic compaction, water transfer, and energy transfer.

VR-CESM Grid Implementation

The VR-CESM grids were generated using a freely available software package (SQuadGen) (Ullrich, 2014). To generate the variable-resolution grid files, SQuadGen interpolates a picture image file, with variations in its gray scale properties, creates a refinement map, and uses spring dynamics to smooth the transitional regions between various grid resolutions. VR-CESM 0.25° (28km resolution) and VR-CESM 0.125° (14km resolution) grids were constructed for both CAM and CLM (Figure 1). Topographic smoothing was varied between the two VR-CESM 0.25° simulations (VR-CESM 0.25° (smooth) and VR-CESM 0.25° (rough)) without modifying the grid structure to assess the sensitivity of topographical influences on VR-CESM simulations. This study further represents the first time variable-resolution grids were implemented into CLM.

Topographic Representation in the VR-CESM Simulations

Topographical datasets were generated for each variable resolution grid. The topographic smoothing was varied between the two VR-CESM 0.25° simulations by adjusting the c parameter from Eqn. (1) in Zarzycki et al (2015). In the case of the VR-CESM 0.25° (smooth) topography, this parameter was equal to 1.33 times that used for generating VR-CESM 0.25° (rough) case. This re-

sulted in the differences in topographical representation seen in Figs. 2a-b. Careful consideration is required when generating the VR-CESM topographical datasets due to the fact that CAM-SE uses terrain-following vertical coordinates that exhibit, with excessive terrain roughness, a tendency towards generation of spurious vertical velocities and numerical artifacts (Zarzycki et al, 2015). The topographical datasets were derived using bilinear interpolation with a linear smoothing operator on the 2-minute National Geophysical Data Center (NGDC) Gridded Global Relief Dataset (ETOPO2v2) (National Geophysical Data Center, 2006) coinciding with the variable-resolution grids surface geopotential and order of the hyperviscosity term. This provides more (less) topographical structure in the high (low) resolution region of the nest. For example, maximum Sierra Nevada topographical elevations (see Figure 2) in the 111 km, 28 km, and 14 km resolutions of CESM were 1583.31 meters, 2677.08 meters, and 3147.28 meters, respectively. When compared with the ETOPO2v2 NGDC dataset, topographical elevation in the Sierra Nevada matches more closely as model resolution increases (Figure 2).

Reference Datasets and Statistical Methods

Reference Datasets

Observational datasets for snowpack metrics such as snow water equivalent (SWE) and snow cover (SNOWC) are particularly difficult to develop in mountainous environments. The fractal nature of snowpack deposits, quick shifts in elevation, angular differences in topography, alpine vegetation cover, cloud cover, and large footprint radius associated with satellite instrumentation are key challenges. Additionally, many satellite products span less than a decade, preventing analysis of climate patterns over decadal timeframes. In situ measurements help alleviate some of the highlighted issues, yet they are irregularly located, and so may not be representative in regions of rapidly varying topography. Land surface models have been used to abate the discontinuous nature of in situ observations, but often contain their own biases. Therefore, to provide a rigorous assessment, a blend of the aforementioned data types will be used in this assessment.

The datasets that this study used for validation purposes are listed in Table 1. Datasets vary in snowpack product availability (i.e., SWE and SNOWC), spatial and temporal resolution, map projection, and temporal range. Therefore, all datasets were standardized to monthly averaged,

13

seasonally averaged (DJF), and climate averaged (DJF from 1980-2005) temporal resolutions during the assessment of the VR-CESM simulations. In order to accomplish this task, utilities from the NetCDF Operators (NCO), Climate Data Operators (CDO), and the NCAR Command Language (NCL) were used.

The North America Land Data Assimilation System Phase 2 (NLDAS-2) produced 0.125° datasets by incorporating large quantities of observational and model reanalysis datasets into three non-atmosphere coupled land-surface models (i.e., Princeton's implementation of VIC, NOAA's Noah, and NASA's Mosaic) over the continental United States. The three datasets provide SWE and SNOWC and are extensively analyzed by Xia et al (2012a,b). For the 2008 California climate change assessment, four GCM (i.e., CCSM3, CNRM, GFDL, and PCM1) datasets were downscaled using Bias Corrected Statistical Downscaling (BCSD) methods along with the VIC model at a resolution of 0.125°. This dataset, known as CAL-ADAPT, provides SWE values over the entirety of California, with the methodology discussed in Maurer and Hidalgo (2008). The DAYMET dataset provides SWE estimations based on meteorological stations. The station data is then extrapolated, using a truncated Guassian weighting filter, to create a high resolution gridded output (Thornton et al, 2014). The Moderate Resolution Imaging Spectroradiometer (MODIS) satellite remote sensing dataset (MODIS/Terra Snow Cover Monthly 0.05° (5 km), Version 5 (MOD10CM V005)) provides SNOWC using a snow mapping algorithm with a Normalized Difference Snow Index (NDSI) (Hall et al, 2006). The NDSI is used to distinguish between snow and other features (such as cloud cover) by using visible and short-wave near-IR spectral bands. A comprehensive analysis and validation of the MODIS dataset for a region of the Sierra Nevada was conducted in Hall and Riggs (2007). The SNOwpack TELemetry (SNOTEL) in situ dataset is comprised of 32 automated observational stations spread throughout the Sierra Nevada mountain range measuring SWE (Serreze et al, 1999). The areal extent of the SNOTEL stations range from 38.07° to 42.99° latitude by -120.79° to -119.23° with an average elevation of 2,343 meters. Of the 32 stations, only 19 were utilized as they spanned the entire 1980-2005 temporal range. The North American Regional Reanalysis (NARR) dataset provides monthly averaged SNOWC output variables using a high resolution atmospheric model (Eta Model) forced by a Regional Data Assimilation System (RDAS) (Mesinger et al, 2006). The other reanalysis dataset used (NCEP - CFSV2) is an updated version

(2013) of its predecessor (2004) and provided SNOWC data (Saha et al, 2014). The NCEP dataset provides better representations of 2m surface temperature, Madden-Julian Oscillation (MJO), and SST forecasts while upgrading overall performance in seasonal to subseasonal forecasting results, compared to its predecessor, and has been advised for decision makers in the water management and agricultural sectors (Saha et al, 2014).

A 0.25° (finite volume) and 1° (spectral element) uniform resolution CESM run were used for comparison to the VR-CESM simulations as well. The 0.25° simulation is described in Wehner et al (2014) and the 1° simulation was performed by the research team with the same component set and dynamical core as the VR-CESM simulations. The final datasets utilized for this assessment were a pair of simulations conducted at UC Davis using the Weather Research and Forecast (WRF) model, which has been used extensively for regional climate studies. Several common parameterization combinations (including different cumulus schemes and radiation schemes) were tested over a one-year simulation period and compared with gridded observations. Those final options were chosen for climate applications that balance long-term reliability and computational cost, representing a typical RCM configuration. Subgrid parameterizations include: the Kain-Fritsch cumulus scheme (Kain, 2004), the WSM 6-class graupel microphysics scheme (Hong and Lim, 2006), and the CAM short-wave and long-wave radiation schemes (Collins et al, 2004). The simulations used a nested domain with a coarse resolution of 27km (WRF-27) and a finer resolution domain of 9km (WRF-9) situated over the western USA (centered over the Sierra Nevada). The initial, boundary conditions, and sea surface temperatures were all provided by ERA-Interim reanalysis data, a widely used and validated dataset for this type of work (Dee et al, 2011). Both WRF domains provide SWE and SNOWC output variables via the Noah Land Surface Model (Chen and Dudhia, 2001) coupled with the Yonsei University (YSU) boundary layer scheme (Hong et al, 2006).

The Noah and CLM4.0-SP land surface models (LSMs) derive from similar snow model formulations (i.e., Anderson (1976)), yet deviate in several ways too. The Noah LSM pulls primarily from Yen (1965), whereas CLM4.0-SP draws from Jordan (1991). This creates differences in both of the snow model's fundamental equations and parameterizations. Differences include number of snow layers (Noah LSM has three, whereas CLM4.0-SP has five), snow thermal conductivity (CLM4.0-

SP uses a snow density function and Noah LSM uses a constant), snow cover hyperbolic functions (CLM4.0-SP utilizes a slightly more complicated formulation) and snowpack-canopy interactions (Oleson et al, 2010; Yang et al, 2011). Of relevance to this paper's overall conclusions, snow depths (and thus SWE) estimations in the Noah LSM have been noted to be significantly overestimated in certain cases due to the assumption that snowpack density, physical characteristics, and thermal conductivity are constant, therefore neglecting heat transfers via meltwater movement in the snowpack (Yang et al, 2011).

Statistical Methods

The DJF climatological mean state and seasonal variability in snow products found within the Sierra Nevada were analyzed. The assessment aimed to understand the efficacy of the new VR-CESM approach in representing snowpack trends against observation, reanalysis and other widely used GCMs and RCMs. In order to do this, the datasets were remapped to similar map projections and resolutions using both the Earth System Modeling Framework (ESMF) capabilities in the NCAR Command Language (NCL) and TempestRemap (Ullrich and Taylor, 2015) software suites. The observational and reanalysis datasets were further remapped to all possible resolutions used in the models (i.e., $0.125°$, $0.25°$, and $1°$). The climate averages and seasonal averages were computed using a mask of the Sierra Nevada (see Figure 3). This mask was developed by the EPA's Ecoregions classification system (Ecoregion Level III - 6.2.12). Summary statistics of the Sierra Nevada were calculated for each of the datasets for SWE and SNOWC including mean, standard deviation, lower quartile, median, upper quartile, and maximum.

For most of the datasets assessed, 25 seasons of average DJF values were used. WRF-9 had 22 DJF seasons. Additionally, MODIS had 12 DJF seasons, many of which fall outside the historical period (1980-2005 vs 2000-2012), but due to the scope of this paper in analyzing the climatological and seasonal mean trends (rather than precise seasonal forecasting) this was assumed to be largely irrelevant.

Seasonal and Multidecadal Snow Trends in the Sierra Nevada

Snow Water Equivalent Summary Statistics

A panel plot of the DJF average SWE is shown across datasets for California (Figure 4). Clear resolution dependence is apparent across all modeling platforms. Each of the datasets highlighted an overall increasing trend in SWE with an increase in model resolution, likely correlated with topographical representation (see Figure 2) and resultant orographic forcing on weather fronts as well as sustained below-freezing temperatures. Of note, the NCEP dataset didn't characterize enough SWE for the Sierra Nevada region to be further assessed in greater statistical detail. Each of the model datasets are compared to the average of the reanalysis datasets at their closest respective resolution of 0.125°, 0.25°, or 1°. Within the Sierra Nevada masked region, VR-CESM 0.125° and VR-CESM 0.25° (rough) demonstrated the closest statistical match across all observational and reanalysis datasets with mean DJF SWE absolute bias values of 6.4 and 2.7 mm, respectively (the reanalysis dataset average SWE value was 97.4 mm), and median values within 8 to 13 mm (Table 2). Maximum DJF SWE values were most closely represented by CESM-FV 0.25° and VR-CESM 0.25° (rough), both within 68 mm. It should be noted that an artificial cap on maximum SWE at 1,000 mm is imposed in CLM4.0 which impacted maximum SWE values for all VR-CESM and UNIFORM CESM simulations. CESM-FV 0.25° and WRF-9 both showed a positive bias in DJF SWE values for mean and median compared to the reanalysis dataset average. CESM-FV 0.25° had a positive bias of 1.8 times the mean DJF SWE and 2.4 times the median value for the Sierra Nevada mask. WRF-9 exhibited a similar response with a positive bias of 2.4 times the mean and 1.4 times the median DJF SWE. The coarser resolution version of VR-CESM and WRF had a negative bias with VR-CESM 0.25° (smooth) at half the mean for DJF SWE in the Sierra Nevada and WRF-27 at 74%. CESM-SE 1°, the model resolution used in most IPCC simulations, was unable to represent both climatological and seasonal DJF SWE trends in the Sierra Nevada with a maximum DJF SWE value of 41.7 mm (<5% of the reanalysis dataset average maximum value), with similar tendencies seen in the mean and median values as well.

Seasonal Variability in Snow Water Equivalent

SWE DJF mean seasonal variability is represented via a plot of standard deviation at each grid point across all datasets (Figure 5). Characterization of interseasonal variability, in comparison to the reanalysis datasets, was shown to be more difficult for most of the modeling platforms. VR-CESM simulations were best represented by VR-CESM 0.25° (rough) which exhibited a slight positive bias of 1% to the reanalysis dataset average (Table 2). VR-CESM 0.125° and VR-CESM 0.25° (smooth) were at 87% and 36% of the standard deviation, respectively. CESM-FV 0.25° had a large discepency in standard deviation tendency with a positive bias of two times the reanalysis dataset average of the reanalysis datasets. WRF-9 showed an exceedingly high variability with 6.8 times the standard deviation of the reanalysis dataset average, although this could be partially amplified by the fact that DAYMET and CESM SWE values were capped at 1,000 mm. Although the standard deviation values were highly variable across modeling platforms in comparison to the reanalysis dataset average, the average seasonal interquartile ranges (IQR) were more closely aligned (Figure 6). The IQR for VR-CESM 0.125° and VR-CESM 0.25° (rough) were closest to the reanalysis dataset average with a slightly negative bias of 11 mm and 7.8 mm, respectively. WRF-9 and CESM-FV 0.25° had a positive bias in IQR, with exceedingly high 75th percentiles, whereas VR-CESM 0.25° (smooth) and WRF-27 were conservative in their higher quartile marks.

Pattern Correlation and Bias in Snow Water Equivalent

The average DJF centered Pearson product-moment coefficients, or the average statistical similarity between two datasets at identical locations for SWE across the 25 seasons (with removal of the mean), for all of the simulations were computed against each of the remapped reference datasets for the Sierra Nevada masked region (Table 3). The Pearson product-moment coefficients are calculated by computing the covariance of the two datasets and dividing by the product of their standard deviations. Averaging all of the Pearson product-moment coefficients across all gridpoints within the mask is useful in showing the seasonal similarity in SWE trend across the entire Sierra Nevada. Interestingly, the VR-CESM simulations were almost identical in average seasonal correlation compared to the reanalysis datasets (at around 0.67 to 0.71) for the Sierra Nevada. WRF-9, remapped to 0.125° (14km) resolution, showed the highest seasonal correlation at 0.83.

However, this was not unexpected considering the WRF simulations were forced by ERA-interim data. Both CESM-FV 0.25° and CESM-SE 1° had the lowest correlation with 0.28 and 0.19, respectively.

Additionally, seasonal average bias was computed across model simulations for the Sierra Nevada (Table 3). VR-CESM 0.25° (rough) had the smallest average seasonal bias to the reanalysis dataset average with a slight negative bias of -2.7 mm, with VR-CESM 0.125° the next closest at -6.4 mm. Although WRF-9 showed best agreement with the NLDAS reanalysis datasets. The WRF and UNIFORM CESM simulations had similar tendencies to one another with a positive seasonal bias occurring in the higher resolution simulations and a negative trend in the coarser resolution simulations, much the same as Caldwell (2010) indicated for winter precipitation tendencies in California. Figure 7 shows the average climatological difference in snow water equivalent between model and reanalysis datasets. Bluer (redder) colors represent a more positive (negative) model bias over the simulation period. In general, higher resolution models tend to overproduce SWE whereas lower resolution models tend to underproduce SWE. This is likely due to the underrepresentation of topography within the model simulations. Interestingly, in several of the simulations a positive bias appears on the western slopes of the Sierra Nevada and a negative bias occurs on the eastern slopes. This may be caused by an oversensitivity to orographically forced upslope winds that push the model to overproduce snowfall as the storms move from the windward to leeward side of the Sierra Nevada. In addition, increased topographic height that does not preserve the fractal peaks and valleys in more detailed representations (see ETOPO2v2 in Figure 2) could artificially enhance orographic uplift. For example, in Figure 7 the orographic uplift bias was shown in the northern Sierra Nevada for VR-CESM 0.125° and less so in VR-CESM 0.25° (rough), a potential reason why nominal improvement was seen in snowpack characteristics for the Sierra Nevada when VR-CESM model resolution was increased.

Climatology of Total Snowpack over the Water Year

The mean daily climatological total SWE (in kg) within the Sierra Nevada was calculated in order to characterize the total water content of the region provided by snowpack (Figure 8). By averaging the total SWE each day over all years (1980-2005) and then multiplying by the area of the mask

$(53,102,699,313 \text{ m}^2)$, the average snowpack mass is shown for the Sierra Nevada across model and reference datasets. Each of the datasets were grouped according to their comparable resolution counterparts (i.e., a) $0.125°$ (14km), b) $0.25°$ (28km), and c) $1°$ (111km)) to better showcase relative magnitudes of Sierra Nevada SWE found within a given climatological day. It should be noted that DAYMET has biases introduced during the dataset formulation that impacts its overall ability to characterize mid-season snowpack and thus alters the SCD and timing of snowmelt. Further, the CAL-ADAPT datasets were not used because daily resolution outputs were not available (only monthly and annual) and the first hour (00 or 12:00 am) of each day within the NLDAS datasets were used within the analysis. In general, VR-CESM $0.125°$ and VR-CESM $0.25°$ (rough) appear to most closely match all of the reanalysis datasets in relative magnitude (Figure 8). A bimodal profile in VR-CESM $0.125°$ is likely indicative of the artificial 1,000 mm cap in SWE imposed within CLM4.0 to prevent excessive snow accumulation over Antarctica - future simulations will attempt to alleviate this by removing the cap away from the polar regions. WRF-9, remapped to 14km, had a high bias associated with total SWE in the Sierra Nevada, with a SCD value of around 21.4×10^{12} kg (more than twice the value shown in most of the reanalysis datasets as well as VR-CESM $0.125°$). In the 28km datasets, the magnitude of total SWE is consistent with the 14km results. VR-CESM $0.25°$ (rough) matched most closely to the NLDAS VIC $0.25°$ reanalysis dataset at 8.0×10^{12} kg, with all other datasets falling under that mark ($<6.0 \times 10^{12}$ kg). The 111km resolution datasets differed greatly from one another, with the peak accumulation of CESM-SE $1°$ values falling much further below the remapped reanalysis datasets. This further highlights the inability of standard-practice $1°$ GCM simulations to capture Sierra Nevada snowpack characteristics, especially with respect to total water content.

Snowpack Timing and Melting Patterns

Peak timing of western USA snowpack accumulation (or SCD) is traditionally thought to occur around April 1st (water day 182), although this has shifted due to regional warming trends in the western USA (Kapnick and Hall, 2012; Montoya et al, 2014). Since most of the reanalysis datasets had discrepancies in representing the total water content and SCD within the Sierra Nevada, normalized values of average climate day SWE are shown in Figure 9 for all datasets in comparison to 19 SNOTEL stations (Figure 3). These stations were chosen based on daily observation avail-

ability spanning the years 1980-2005. Further, the SNOTEL locations are representative of several elevations found within the Sierra Nevada, spanning from 1864 m (Spratt Creek) to 2879 m (Virginia Lakes Ridge). Of note, the SNOTEL stations are clustered in the northern to central Sierra Nevada, with no stations present in the south. As such, a subregion of the Sierra Nevada was made to compare model results with observations from SNOTEL stations (see solid black subregion in Figure 3). This subregion was created using 12 of the USGS Hydrologic Units in the Sierra Nevada (Seaber et al, 1987). If a SNOTEL station was located within or near an adjoining hydrologic unit then the entire unit was kept (within the boundary of the Sierra Nevada Ecoregion). Further, since the lowest elevation SNOTEL station was located at 1864 m (Spratt Creek), a topographical threshold of 1824 m was imposed to create the subregion (this altitude was chosen to provide a buffer around Spratt Creek). The normalizations were computed by removing the relative mean from all climatological days within a given dataset and then dividing the resultant values by the standard deviation. Like the plots for the mean daily climatological sums of SWE, all datasets are grouped according to resolution, with added comparison to SNOTEL in each plot (Figure 9). Among models, VR-CESM 0.125° and WRF-9 matched most closely to SNOTEL. However, both had an early SCD bias. The SCD in VR-CESM 0.125° falls around water year day 170 (March 21st), the closest match to SNOTEL across all model datasets. SCD for WRF-9 falls around water year day 160 (March 11th), around two weeks before the expected date. Melt rate and the date at which the complete melt of SWE occurs differentiated VR-CESM 0.125° and WRF-9, with WRF-9 more closely matching SNOTEL. The melt rate in VR-CESM 0.125° was too rapid resulting in a complete melt occuring around 30 days sooner than in the SNOTEL dataset. DAYMET had a late SCD around day 191 (April 10th), 10 days after SNOTEL. The melt rate in the DAYMET dataset was much slower than all other datasets. Further, since DAYMET analyzed each year in isolation, the snowpack was discontinuous at water year day 91 (Thornton et al, 2014). Snowpack accumulation onset matched fairly well across all datasets, with the onset date around water year day 36 (November 5th). Within the 28km simulations, most model datasets seem to match in terms of having an earlier expected SCD clustered on water year day 151 (March 1st), around 30 days sooner than SNOTEL. The remapped version of DAYMET at 0.25° showed a similar late SCD bias (water year day 191) and showed a more drastic slow down in melt rate. All 0.25° datasets matched fairly well in snowmelt rate and accumulation onset, matching well with SNOTEL. Full

melt generally occured earlier (water year day 240) across models compared to SNOTEL (water year day 270). In the 1° datasets, CESM-SE 1° had a physically unreasonable SCD (water year day 90), snowmelt rate, and accumulation onset date. Interestingly, at the 1° resolution, the biases in DAYMET are minimized and the SCD, snowmelt rate, date of complete melt, and accumulation onset date all are well within the range of SNOTEL.

Linear Trends in DJF Seasonal Snowpack

Figure 10 highlights the linear trend in DJF seasonal mean SWE values for the historical period in the Sierra Nevada SNOTEL subregion. For comparison, the 19 SNOTEL station datasets are plotted in the upper left panel. The gray lines indicate individual SNOTEL stations with the mean SNOTEL station seasonal trend shown in black and the linear trend line in red. Each of the model and reanalysis datasets are plotted using similar axis bounds, except for WRF-9 which exhibited larger values of SWE. SNOTEL stations are plotted with a larger axis, representative of these observations being pointwise measurements in regions of greater snow accumulation. The general trend across VR-CESM simulations is a slight decrease in DJF seasonal mean SWE. VR-CESM 0.125° had the largest negative trend at -0.198 mm/year, with VR-CESM 0.25° (smooth) at -0.093 mm/year and VR-CESM 0.25° (rough) at -0.029 mm/year. Except when compared to CAL-ADAPT which shows a dramatic increase in SWE and DAYMET which shows a faster decrease in SWE, the general trend for VR-CESM datasets are slightly more negative than the SNOTEL and NLDAS reanalysis datasets. This result is corroborated by Mote et al (2005) who found a 2.2% decline in mean April 1st SWE across the in situ snowpack observational stations within the Sierra Nevada over the historical record (i.e., 1990-1997 (final period) minus 1945-1950 (initial period)), with inclusion of snow course data too. Interestingly, the 19 sampled SNOTEL stations showed a nearly flat trend (0.016 mm/year) in DJF mean seasonal SWE over the study period. WRF simulations showed differing results, with WRF-9 showing an exceedingly strong positive trend (0.410 mm/year) in mean seasonal SWE and WRF-27 having a stagnant to slightly positive trend (0.011 mm/year) matching most closely with SNOTEL. CESM-SE 1° and CESM-FV 0.25° both had a negative trend in mean seasonal SWE, with magnitudes of -0.259 mm/year and -0.200 mm/year.

Snow Cover (SNOWC) Summary Statistics

Figure 11 represents average climatological DJF SNOWC plotted for all datasets over California. Similar to SWE, an increase in resolution results in a much more heterogeneous representation of SNOWC properties that is more closely matched to observations, indicated by 12 seasons of MODIS (MODIS-5) data. A topographic influence is clearly seen as resolution is increased, with higher resolution models capturing lower elevation basins that are otherwise smoothed out. This resolution dependence manifests itself in statistical calculations of average DJF SNOWC within the Sierra Nevada (Table 4). WRF-9 showed the closest match to mean seasonal SNOWC with a value only 1.5% lower than the MODIS dataset. VR-CESM 0.25° (rough) and VR-CESM 0.125° were the next closest with a slightly more conservative estimate (7% below MODIS) of SNOWC. All other datasets, except CESM-FV 0.25° which had a positive bias of around 8%, had much smaller estimates of mean seasonal SNOWC. CESM-SE 1° provided the largest underestimate among the model datasets with mean seasonal values at a quarter of the comparable remapped version of MODIS. Interestingly, two of the best available high resolution reanalysis datasets (NCEP and NARR) seem unable to properly capture the Sierra Nevada SNOWC characteristics in the MODIS dataset, with most of the reanalysis datasets showing a negative bias for SNOWC. NARR-32 and NCEP-35 had mean SNOWC values at half to two-thirds of the value indicated by MODIS and NLDAS VIC, NOAH, and MOSAIC were at 84%, 74%, and 47% of MODIS, respectively. The median values for DJF SNOWC for VR-CESM 0.125° and VR-CESM 0.25° showed a close approximation to those seen in NLDAS VIC. As expected, since SNOWC is capped at 100%, maximum DJF SNOWC was reached by most modeling platforms.

Seasonal Variability in Snow Cover

Mean seasonal variability (interannual standard deviation of the seasonal mean) in SNOWC is shown over California (Figure 12). Standard deviation values for each of the simulations are given in Table 4. As with the mean seasonal SNOWC values, WRF-9 had the best representation of seasonal variability within the Sierra Nevada, with a close approximation to standard deviation values in the remapped MODIS dataset (although it underestimates standard deviation in the lee of the Sierra Nevada). VR-CESM 0.25° (rough) also was able to characterize seasonal variability at

a realistic level, with a standard deviation only 14% below MODIS. All other modeling platforms had a conservative estimate of variability ranging from half to three-fourths of the observed standard deviation, when comparing to common remapped resolutions. This result is apparent in Figure 13 for each dataset and analyzing the IQRs. All datasets, save for WRF-9 and CESM-FV 0.25°, had a conservative estimate of SNOWC summary statistics when compared to MODIS. Median values, along with IQRs, are too low with a noticeable bias in the 75th percentiles.

Pattern Correlation and Bias in Snow Cover

The average seasonal centered Pearson product-moment coefficients and mean climatological bias for SNOWC are exhibited in Table 5. MODIS was not used in the centered Pearson calculations as it only spanned five years of the historical period (2000-2005). A close match was seen across both VR-CESM and WRF modeling platforms when compared to the three NLDAS datasets. Most values fell around 0.74 for the VR-CESM simulations and 0.84 for the WRF simulations. The CESM-FV and CESM-SE had the lowest correlations at 0.53 and 0.15, respectively. The smallest mean climatological bias in DJF SNOWC between MODIS and the model datasets was VR-CESM 0.125°, VR-CESM 0.25° (rough) and WRF-27, with negative baises of approximately 6-7%. CESM-SE 1° produced the worst match across model datasets with a -28.5% bias. Of note, the NLDAS reanalysis datasets also widely varied in their ability to characterize mean climatological SNOWC bias when compared to MODIS with consistent negative biases ranging between -9.2% (NLDAS VIC) to -29.4% (NLDAS MOSAIC).

Discussion and Conclusion

The primary goal of this paper has been to assess the efficacy of VR-CESM in simulating the mean climatological state and seasonal variability within Sierra Nevada snowpack metrics (i.e., SWE, SCD, and SNOWC). It was determined that the efficacy of the VR-CESM framework in simulating climatological mean and seasonal variability in both SWE and SNOWC was competitive with traditional dynamical downscaling. Overall, considering California's complex terrain and intermittent climate, a 0.68 centered correlation (less correlated, yet similar to values seen in WRF), negative mean SWE bias of <7 mm, and an IQR well within the range of values exhibited in the best available spatially continuous datasets for SWE, the ability of both VR-CESM 0.25° (rough) and

24

VR-CESM 0.125° to simulate SWE on both climatological and seasonal scales was confirmed. Of note, both of the VR-CESM simulations were solely constrained by prescribed SST and sea ice data, whereas WRF simulations were further constrained at lateral boundaries by ERA-interim data (in addition to SST and sea ice), yet both showed comparable statistical properties. This was similarly confirmed for the climatological mean for DJF SNOWC where both the VR-CESM 0.125° and VR-CESM 0.25° (rough) simulations were within 7% of the expected mean MODIS value. VR-CESM 0.25° (rough) was able to characterize MODIS' standard deviation well (86% match). WRF-9 had the best representation of SNOWC with a near identical representation in mean, standard deviation, and IQR, compared to MODIS, but at the cost of unreasonably high SWE values. This is likely indicative of the over-exaggeration of topography at higher resolutions in the model, where the fractal nature of peaks and, importantly, valleys are misrepresented (compare ETOPO2v2 to model topography in Figure 2) leading to a bias in overall snowpack characterizations. VR-CESM, as well as WRF, conveyed mixed results in representing seasonal variability in SWE (average standard deviation value at each grid point), with generally conservative estimates across all assessed modeling platforms except WRF-9 and CESM-FV 0.25° which had much higher estimates. The total water content of snowpack within the Sierra Nevada was best represented in both VR-CESM 0.125° and VR-CESM 0.25° (rough) when compared to the remapped NLDAS VIC reference dataset at their respective resolutions. VR-CESM 0.125° and WRF-9 showcased the best representation, across datasets, of SCD timing, snowmelt rate, and snowpack accumulation onset, in comparison to SNOTEL. The two datasets differed in the date at which complete melting of SWE occured with VR-CESM 0.125° occuring too early, whereas WRF-9 had a slightly late onset. Interestingly, both SWE and SNOWC didn't show a significant enhancement in snowpack properties when VR-CESM resolution was moved from 0.25° to 0.125°; in fact the 0.25° simulation (VR-CESM 0.25° (rough)) was slightly more skillful when considering all metrics. Topographical roughness was found to play a much more significant role in representing snowpack properties with VR-CESM 0.25° (rough) seeing a sixteen-fold decrease in average seasonal SWE bias, threefold increase in SWE seasonal variability, an IQR increase from 48.9 to 64.1, and a considerable increase in the SCD total water content for the Sierra Nevada. This is an improvement when compared to the average of all of the reanalysis datasets. Furthermore, DJF temperature characteristics may have played a role in modulating which of the simulations performed most optimally. Figure 14 highlights

average climatological DJF 2m surface temperatures for only the model simulations. Below freezing (< 273 K) temperatures are shown to be maintained over greater areas for the climatic period across all higher resolution ($\leq 0.25°$) simulations, likely because of increased topographic elevations in those areas. This temperature maintenance likely drives winter season snowpack accumulation and sustainment.

The VR-CESM framework provides greatly enhanced representation of snowpack properties compared to widely used GCMs (i.e., CESM-FV 1° and CESM-FV 0.25°). Simulation of Sierra Nevada snowpack in the VR-CESM framework is competitive with traditional dynamical downscaling techniques, but has the additional means of providing dynamic interaction with large-scale atmosphere-ocean drivers and teleconnections that might not otherwise manifest in an RCM constrained by boundary conditions. These two points lend them themselves well to using certain versions of VR-CESMs (namely VR-CESM 0.25° (rough) and VR-CESM 0.125°) in projecting future climate change scenarios and their resultant impacts on water resources over the western USA.

The topographical smoothing between the two VR-CESM 0.25° simulations had the most dramatic influence on snowpack product tendencies found within the VR-CESM framework, even when compared to changes resulting from a doubling of model resolution from 0.25° to 0.125°. As shown in Table 2, mean seasonal SWE for the Sierra Nevada nearly doubled from 50.4 mm to 95.2 mm between VR-CESM 0.25° (smooth) and VR-CESM 0.25° (rough), with a decrease in average DJF climate bias in SWE from -52% to -2.3% when compared to the reanalysis dataset average. This tendency was similar for the lower quartile, median, and higher quartile values. Similarily, the seasonal variability, indicated by the standard deviation plots (Figure 5) and standard deviation values in Table 2, nearly tripled, making the VR-CESM 0.25° (rough) simulation the closest match to the reanalysis dataset average within all model simulations. Changes in SNOWC trends were also apparent, although less dramatic than SWE (Table 4). Average seasonal SNOWC increased by 9% and the IQR increased from 48.9 to 64.1, matching more closely to the MODIS dataset value of 74.5, with the higher quartile less conservatively biased.

Improved topographical resolution also resulted in better representation of the snow characteristics of the maritime mountain ranges (e.g., the Cascades and the Coastal Range) (Figure 4). Maritime

mountain ranges have shown some of the greatest snowpack decreases over the historical record (Serreze et al (1999); Mote (2003); Mote et al (2005)) and are in need of the best available climate change impact analysis due to a greater susceptibility to climate change trends (i.e., warmer and potentially more precipitous weather fronts originating from relatively warmer ocean waters). This is important because conventional GCM simulations are generally performed at resolutions too coarse to properly resolve the aforementioned topographical forcings and, thus, may bias evaluations used to guide climate impact studies and climate policy formulation. This isn't to say that the VR-CESM framework provides perfect representation of these ranges, but that it provides a more realistic and computationally effective means to characterize these ranges in a changing climate. This subject will be the target of further research.

A higher resolution surface dataset for PFT type would have been beneficial for this study, to capitalize on the higher resolution ($<0.5°$) VR-CESM grids implemented into CLM, however none were available at the time of writing. An extensive review of the North American and European snowpack-canopy interaction literature by Varhola et al (2010) argued that snowpack accumulation and melting patterns can be significantly altered by changes in forest cover, accounting for relative variance changes of 57% in snow accumulation and 72% in snow ablation. After discussion with the CLM development team at NCAR, a two minute PFT dataset for the year 2000 was identified. This dataset will be used in future simulations to assess the effects of canopy interactions on snowpack metrics within a VR-CESM framework.

Added benefits of the VR-CESM framework, not discussed previously, include the large enhancement in computational efficiency. For example, the $0.25°(0.125°)$ VR-CESM grid had approximately 8,400 (11,300) elements. When compared to conventional uniform resolution grids at $1.00°$, $0.25°$ or $0.125°$, which have 5,400, 86,400, and 345,600 elements respectively, a theoretical speedup in computation time of 10 to 30 times is expected for the VR-CESM framework, with the assumption of linear computational scalability highlighted in Dennis et al (2012) and Zarzycki et al (2014a). Therefore, for a relatively similar computational cost of a uniform $1.00°$ grid, one can get vastly improved snowpack product characteristics over a limited region of interest, especially within the California Sierra Nevada. This is a function of not only resolving smaller scale mete-

orological features, but also due to better representations of topography and, in some cases, land surface properties. Therefore, for only a fraction of the cost of a high resolution uniform GCM run, the VR-CESM approach can be performed on a local server (<1000 processors), with 20-40 day turnarounds on 25 year simulation periods, and provide model resolutions of $0.25°$ (28 km) to $0.125°$ (14 km), which decision makers (especially in the western USA water sector), may find more useful in regional planning endeavors. The enhanced representation of snowpack and relative computational efficiency of VR-CESM lends itself well to future investigations of other SWE dependent regions of the western USA, as well as ensemble-based climate change scenario analysis.

Tables

Table 1: Datasets, and associated metadata, used to analyze the accuracy of the Variable Resolution Global Climate Model (VR-CESM) simulations

Datasets	Snowpack Product	Spatial Resolution	Temporal Resolution	Projection	Years Assessed
VR-CESM 0.25° (smooth)	SWE and SNOWC	28km	Daily	VR-CESM in CAM and CLM - Equidistant	1980-2005
VR-CESM 0.25° (rough)	SWE and SNOWC	28km	Daily	VR-CESM in CAM and CLM - Equidistant	1980-2005
VR-CESM 0.125°	SWE and SNOWC	14km	Daily	VR-CESM in CAM and CLM - Equidistant	1980-2005
UNIFORM CESM (SE and FV)	SWE and SNOWC	111 km and 28 km	Daily	Equidistant	1980-2005
WRF	SWE and SNOWC	27km, 9km	Daily	Lambert Conformal	1980-2005
DAYMET	SWE	1km	Daily	Lambert Conformal Conic	1980-2005
CAL-ADAPT	SWE	14km	Monthly	Equidistant	1980-2005
SNOTEL	SWE	Point Source (19 stations)	Daily	Point Source (Automated Station)	1980-2005
NLDAS-2	SWE and SNOWC	14km	Hourly, Monthly	Equidistant	1980-2005
NCEP (CFSv2)	SWE and SNOWC	35km	Daily	Equidistant	1980-2005
NARR	SNOWC	32km	Daily	Lambert Conformal	1980-2005
MODIS/Terra	SNOWC	5km	Monthly	Geographic Lat Lon or Climate Modeling Grid (CMG)	2000-2013

Table 2: Summary Statistics of Seasonally Averaged Snow Water Equivalent (SWE) in the Sierra Nevada

Model	DJF Seasons	Mean	Standard Deviation	Lower Quartile	Median	Upper Quartile	Max	Sierra Mask Points
VR-CESM 0.25° (smooth)	25	50.4	80.1	3.10	19.8	60.9	663	2175
VR-CESM 0.25° (rough)	25	95.2	134	5.30	32.9	132	750	2175
VR-CESM 0.125°	25	91.0	125	7.40	37.6	125	751	8775
WRF-27	25	71.6	102	6.20	29.2	91.0	701	2175
WRF-9	22	233	365	5.60	48.8	314	3090	14058
WRF-9 (REGRID 0.125°)	22	231	349	7.60	63.2	317	2850	7721
CESM-SE 1°	25	3.40	7.50	0.00	0.50	2.40	41.7	150
CESM-FV 0.25°	25	179	188	23.6	111	291	875	2175
DAYMET	25	109	176	1.40	36.9	141	1000	1202620
DAYMET (REGRID 0.125°)	25	107	173	1.60	35.1	140	1000	8678
DAYMET (REGRID 0.25°)	25	102.3	168.4	1.90	32.0	127	1000	2156
DAYMET (REGRID 1°)	25	28.0	36.8	2.00	12.1	39.8	174	149
NLDAS VIC 0.125°	25	72.9	103	2.90	29.1	101	777	8748
NLDAS VIC (REGRID 0.25°)	25	73.8	102	3.10	29.4	105	629	2169
NLDAS VIC (REGRID 1.00°)	25	38.1	71.3	1.50	7.80	30.8	345	149
NLDAS NOAH 0.125°	25	56.3	84.2	1.50	19.7	75.5	616	8775
NLDAS NOAH (REGRID 0.25°)	25	57.4	84.4	1.70	21.1	75.9	518	2175
NLDAS NOAH (REGRID 1°)	25	28.7	56.4	0.70	5.60	23.0	321	150
NLDAS MOSAIC 0.125°	25	59.5	98.6	0.60	11.3	76.3	773	8748
NLDAS MOSAIC (REGRID 0.25°)	25	60.5	98.2	0.70	11.6	79.2	647	2171
NLDAS MOSAIC (REGRID 1°)	25	27.1	60.9	0.19	2.40	14.2	325	149
CAL-ADAPT CCSM3 0.125°	25	134	154	9.60	80.7	202	1060	8775
CAL-ADAPT CCSM3 (REGRID 0.25°)	25	136	155	9.90	80.8	206	944	2175
CAL-ADAPT CCSM3 (REGRID 1°)	25	73.4	88.1	1.20	48.4	107	416	150
CAL-ADAPT CNRM 0.125°	25	125	157	8.10	67.3	185	1210	8773
CAL-ADAPT CNRM (REGRID 0.25°)	25	127	158	8.60	68.5	191	1090	2174
CAL-ADAPT CNRM (REGRID 1°)	25	66.4	88.2	2.40	27.4	89.8	544	149
CAL-ADAPT GFDL 0.125°	25	95.0	121	5.40	49.1	141	959	8775
CAL-ADAPT GFDL (REGRID 0.25°)	25	96.3	122	5.60	49.3	141	855	2175
CAL-ADAPT GFDL (REGRID 1°)	25	47.0	65.2	1.90	26.0	67.6	448	150
CAL-ADAPT PCM1 0.125°	25	129	151	14.2	75.2	186	926	8775
CAL-ADAPT PCM1 (REGRID 0.25°)	25	131	153	15.4	75.8	188	861	2175
CAL-ADAPT PCM1 (REGRID 1°)	25	73.8	90.5	6.60	45.4	99.1	426	150
Reanalysis Dataset Average 0.125°	N/A	97.4	134	5.50	45.9	138	915	N/A
Reanalysis Dataset Average 0.25°	N/A	97.9	134	5.90	46.1	139	818	N/A
SNOTEL	25	237	186	103	195	308	1220	19 stations

Table 3: Snow Water Equivalent (SWE) Climatological Bias and DJF Seasonal Pearson Product-Moment Coefficients (Centered) within the Sierra Nevada. Absolute value averages are computed to eliminate sign dependency in bias comparisons across datasets.

Model	VR-CESM 0.125°	VR-CESM 0.25° (rough)	VR-CESM 0.25° (smooth)	WRF-9	WRF-27	CESM-FV 0.25°	CESM-SE 1°
DJF Climate Bias (units - mm)							
NLDAS VIC	18.1	21.4	23.4	158	2.20	106	34.7
NLDAS NOAH	34.7	37.8	7.00	175	14.2	122	25.3
NLDAS MOSAIC	31.5	34.7	10.1	172	11.1	119	23.7
CALADAPT CCSM3	42.8	40.3	85.1	97.3	63.9	43.9	70.0
CALADAPT CNRM	34.4	31.8	76.6	105.7	55.4	52.4	63.0
CALADAPT GFDL	4.00	1.10	45.9	136	24.7	83.1	43.6
CALADAPT PCM1	37.9	35.3	80.1	102	58.9	48.9	70.4
DAYMET	16.3	7.10	51.9	124	30.7	77.1	24.6
Reanalysis Dataset Absolute Value Average	27.5	26.2	47.5	134	33.8	81.3	44.5
DJF Pearson Pattern Correlation							
NLDAS VIC	0.72	0.75	0.72	0.90	0.78	0.33	0.09
NLDAS NOAH	0.69	0.71	0.68	0.88	0.74	0.35	0.07
NLDAS MOSAIC	0.68	0.73	0.69	0.86	0.73	0.25	0.06
CALADAPT CCSM3	0.71	0.75	0.75	0.85	0.75	0.32	0.32
CALADAPT CNRM	0.71	0.75	0.73	0.85	0.75	0.31	0.29
CALADAPT GFDL	0.70	0.74	0.75	0.84	0.73	0.29	0.32
CALADAPT PCM1	0.72	0.76	0.73	0.86	0.76	0.35	0.33
DAYMET	0.45	0.48	0.42	0.63	0.48	0.04	0.08
Reanalysis Dataset Average	0.67	0.71	0.68	0.83	0.71	0.28	0.19

Table 4: Summary Statistics of Seasonally Averaged Snow Cover (SNOWC) in the Sierra Nevada

Model	DJF Seasons	Mean	Standard Deviation	Lower Quartile	Median	Upper Quartile	Max	Sierra Mask Points
VR-CESM 0.25° (smooth)	25	40.0	30.1	13.6	36.5	62.5	100	2175
VR-CESM 0.25° (rough)	25	48.9	33.5	17.5	46.7	81.6	100	2175
VR-CESM 0.125°	25	48.7	30.3	22.0	47.8	74.1	100	2175
WRF-27	25	42.9	30.1	15.3	40.0	67.2	98.0	2175
WRF-9	22	55.0	37.3	16.3	58.6	96.7	98.0	14058
WRF-9 (REGRID 0.125°)	22	54.3	35.6	19.1	56.3	92.3	98.0	7721
CESM-SE 1°	25	9.10	12.3	0.60	4.40	11.9	60.3	150
CESM-FV 0.25°	25	62.8	32.2	36.6	69.9	92.3	100.0	2175
NCEP-35	25	37.1	25.5	15.3	33.7	56.5	96.6	1350
NARR-32	25	22.5	27.5	0.60	9.60	37.5	100	1175
MODIS-5	12	56.7	36.6	18.0	65.0	93.0	100	25932
MODIS-5 (REGRID 0.125°)	12	55.8	35.8	18.5	62.8	90.7	100	4188
MODIS-5 (REGRID 0.25°)	12	55.0	36.0	16.3	61.4	90.8	100	1032
MODIS-5 (REGRID 1°)	12	37.6	33.1	3.80	34.0	69.1	95.7	60
NLDAS VIC 0.125	25	46.6	33.0	15.0	45.9	75.9	100	8742
NLDAS VIC 0.25	25	46.8	33.3	14.9	45.1	78.4	100	2166
NLDAS VIC 1.00	25	32	25.4	11.6	26.6	45.8	87.5	149
NLDAS NOAH 0.125	25	41.5	33.8	7.60	37.5	71.6	100	8720
NLDAS NOAH 0.25	25	42.1	34.3	8.30	38.4	73.4	100	2164
NLDAS NOAH 1.00	25	25.9	25.4	4.10	18.3	40.7	85.0	149
NLDAS MOSAIC 0.125	25	26.4	29.6	1.40	13.1	45.4	98.8	8722
NLDAS MOSAIC 0.25	25	26.8	30.1	1.40	13.1	47.6	98.2	2163
NLDAS MOSAIC 1.00	25	12.8	18.8	0.30	4.20	14.4	66.7	149
Reanalysis Dataset Average 0.125°	N/A	42.6	33.1	10.6	39.8	70.9	99.7	N/A
Reanalysis Dataset Average 0.25°	N/A	42.7	33.5	10.2	39.5	72.6	99.6	N/A

Table 5: Snow Cover (SNOWC) Climatological Bias and DJF Seasonal Pearson Product-Moment Coefficients (Centered) within the Sierra Nevada. Absolute value averages are computed to eliminate sign dependency in bias comparisons across datasets.

Model	VR-CESM 0.125°	VR-CESM 0.25° (rough)	VR-CESM 0.25° (smooth)	WRF-9	WRF-27	CESM-FV 0.25°	CESM-SE 1°
DJF Climate Bias (units - mm)							
NLDAS VIC	2.10	2.10	-6.80	-3.70	1.90	16.0	-22.9
NLDAS NOAH	7.20	6.80	-2.10	1.40	6.60	20.7	-16.8
NLDAS MOSAIC	22.3	22.1	13.2	16.5	21.9	36.0	-3.70
MODIS-5	-7.10	-6.10	-15.0	-12.9	-6.30	7.80	-28.5
Reanalysis Dataset Absolute Value Average	9.70	9.30	9.30	8.60	9.20	20.1	18.0
DJF Pearson Pattern Correlation							
NLDAS VIC	0.76	0.79	0.77	0.92	0.84	0.56	0.24
NLDAS NOAH	0.78	0.80	0.77	0.92	0.85	0.60	0.17
NLDAS MOSAIC	0.65	0.69	0.68	0.78	0.76	0.44	0.04
Reanalysis Dataset Average	0.73	0.76	0.74	0.87	0.82	0.53	0.15

Figures

VR-CESM 0.25°

VR-CESM 0.125°

110km

110km
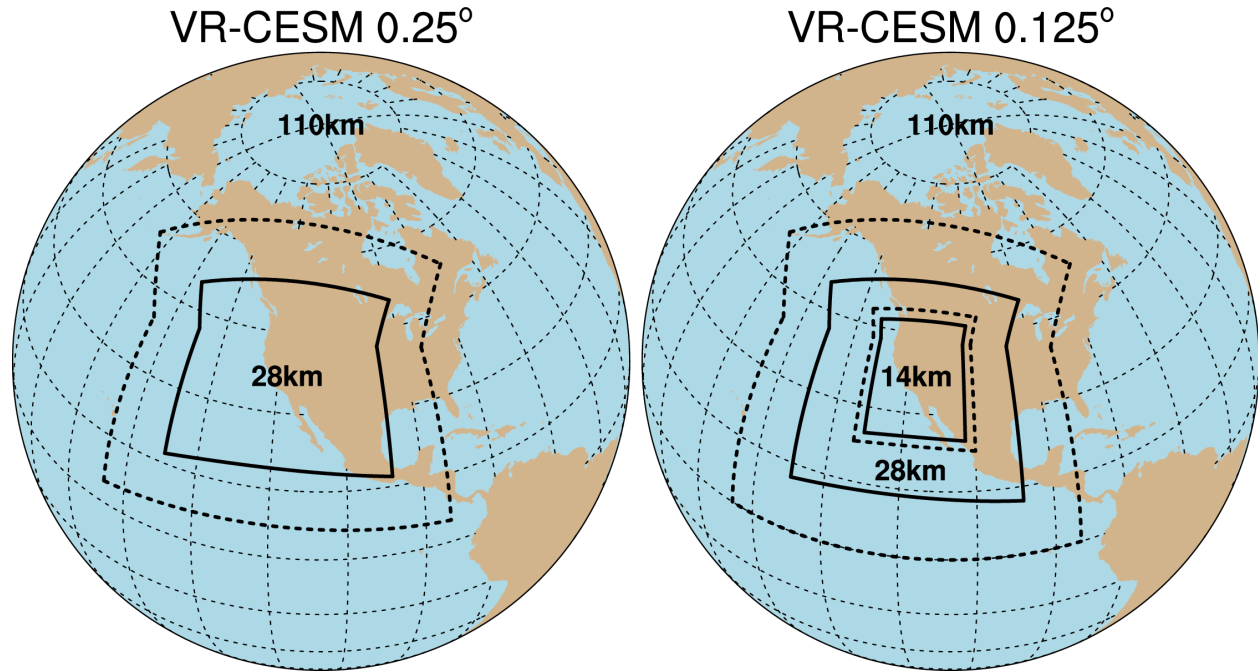
28km

14km

28km

Figure 1: The two variable-resolution global climate model grids (0.25° (28km), left and 0.125° (14km), right) used for this study. Both grids are developed on a cubed-sphere with a 1.00° quasi-uniform resolution (111km). The dashed lines highlight the model transition region and the solid lines indicate the higher resolution regions.
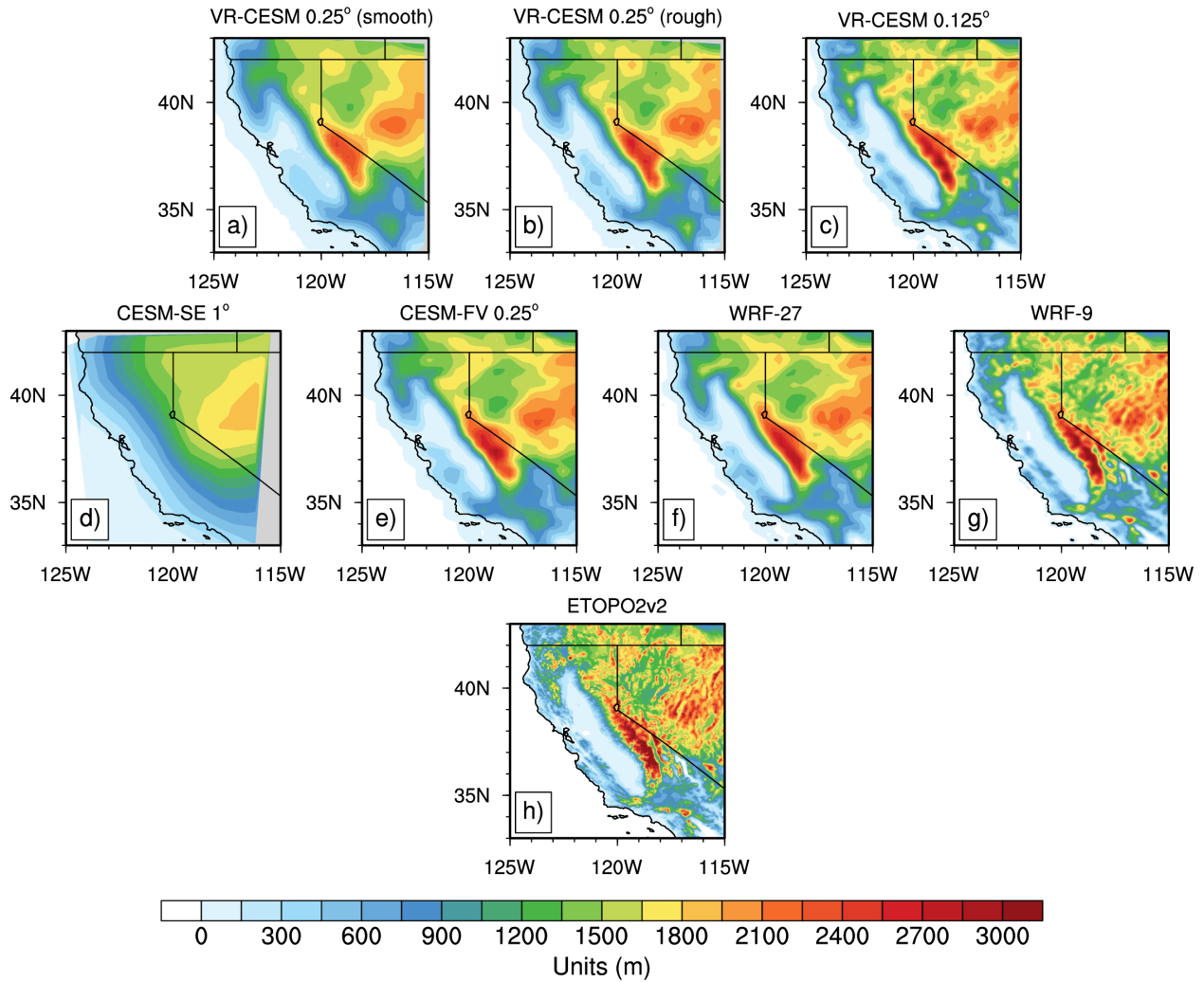
Figure 2: Topographical representation of the Sierra Nevada mountain range and surrounding regions across model datasets. Topography from variable-resolution CESM is displayed in order of increasing grid resolution from (a) to (c). The standard CESM and WRF simulations are displayed in order of increasing resolution from (d) to (g). The ETOPO2V2 dataset, representing 2-minute (2 km) gridded topographic relief is depicted in (h).
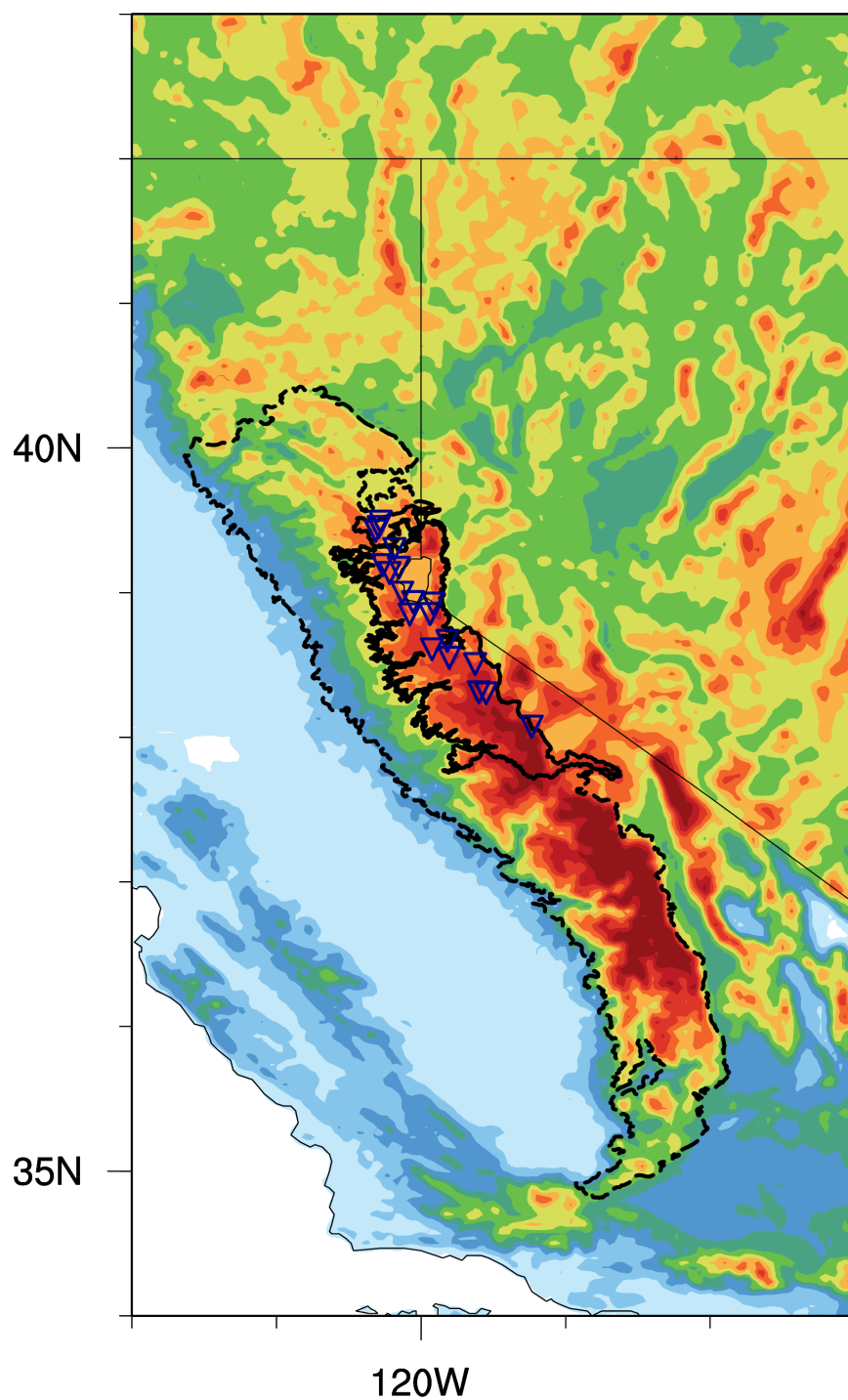
Figure 3: The EPA's Ecoregion Level III (6.2.12) shapefile mask used for summary statistic calculations of the Sierra Nevada mountain range (dashed black outline). SNOTEL station locations (blue triangles) are overlaid onto the ETOPO2v2 topography. The solid black outline is used to indicate the subregion used to compare model and reanalysis data to SNOTEL stations.
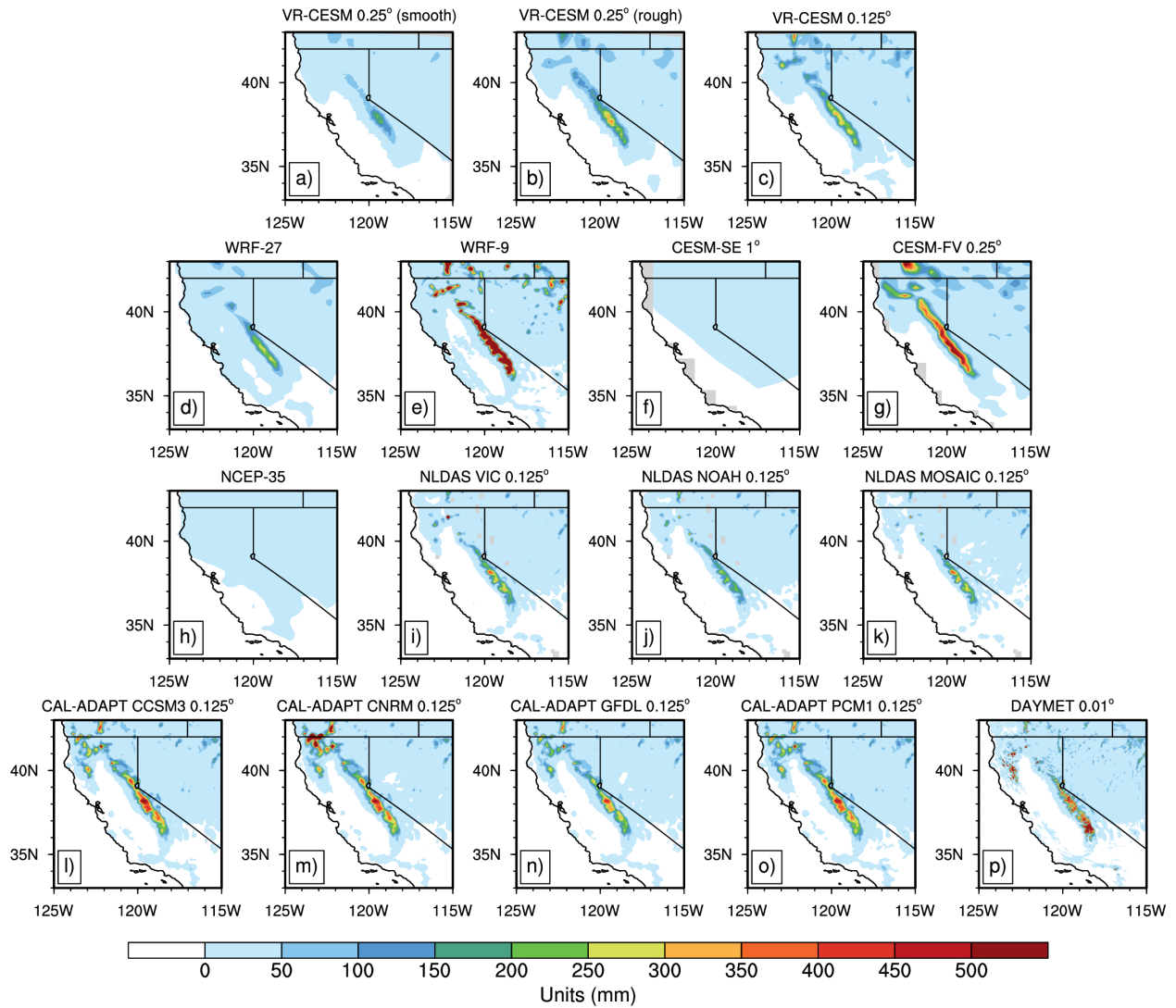
Figure 4: Average climatological DJF snow water equivalent (SWE) across model and observational datasets over California.

Figure 5: Average DJF variability (interannual standard deviation of the seasonal mean) of snow water equivalent (SWE) across model and observational datasets over California.
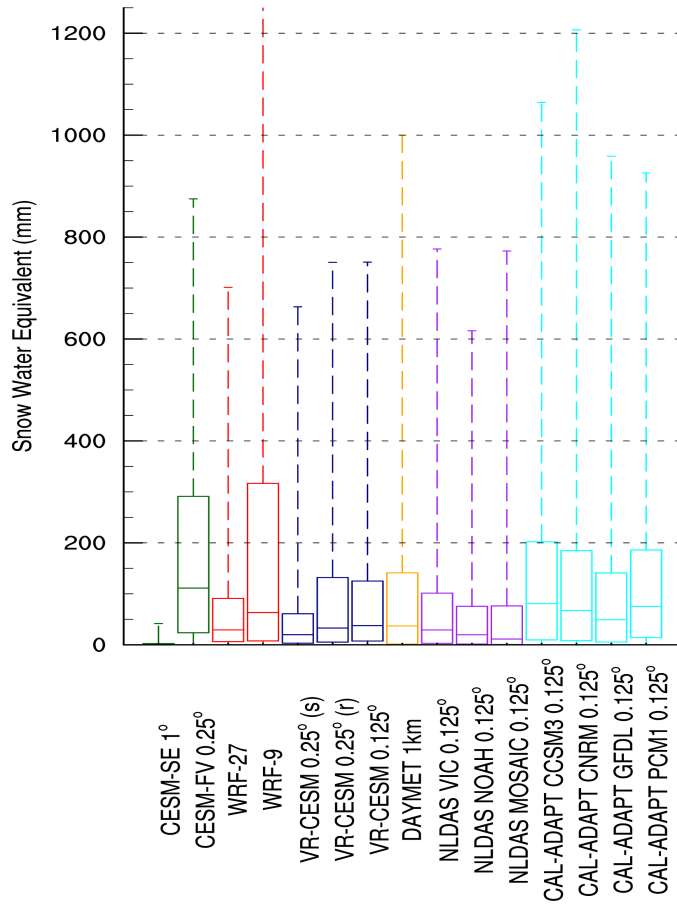
Figure 6: Boxplots of seasonal (DJF) Sierra Nevada snow water equivalent (SWE) across modeling platforms and observational datasets. The boxes represent the 25th and 75th percentile values within the Sierra Nevada masked region, with the median value indicated in between. The minimum and maximum range is depicted by vertically dashed lines. Regridding of reanalysis datasets to $0.25°$ (or $0.125°$ for DAYMET) had no noticeable effect on the statistics and so are not shown.
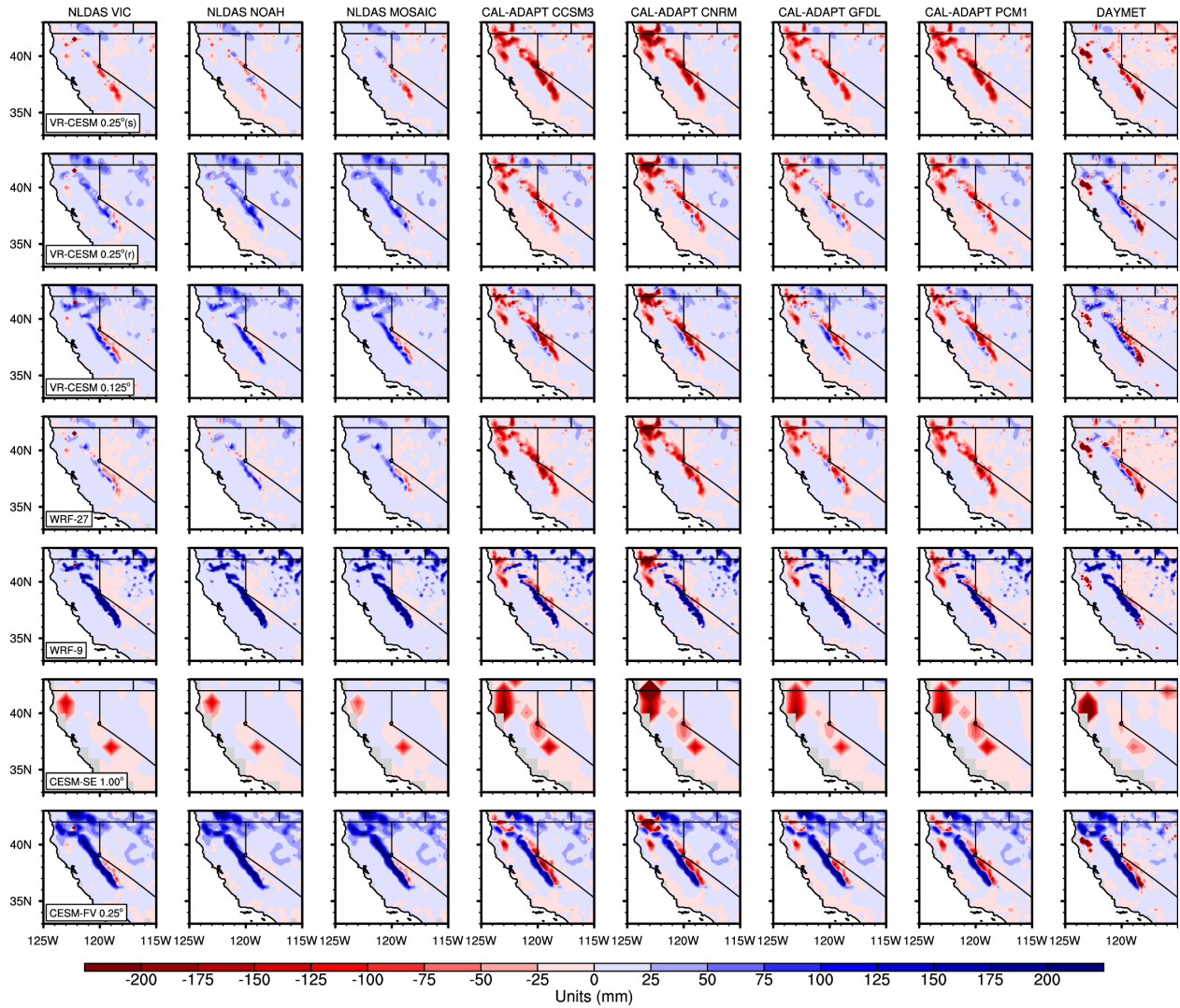
Figure 7: Average difference in DJF SWE between model and reanalysis datasets over California. Rows indicate model output and columns represent gridded or reanalysis datasets. Blue (red) indicates a model positive (negative) difference in SWE compared to the given reanalysis dataset.
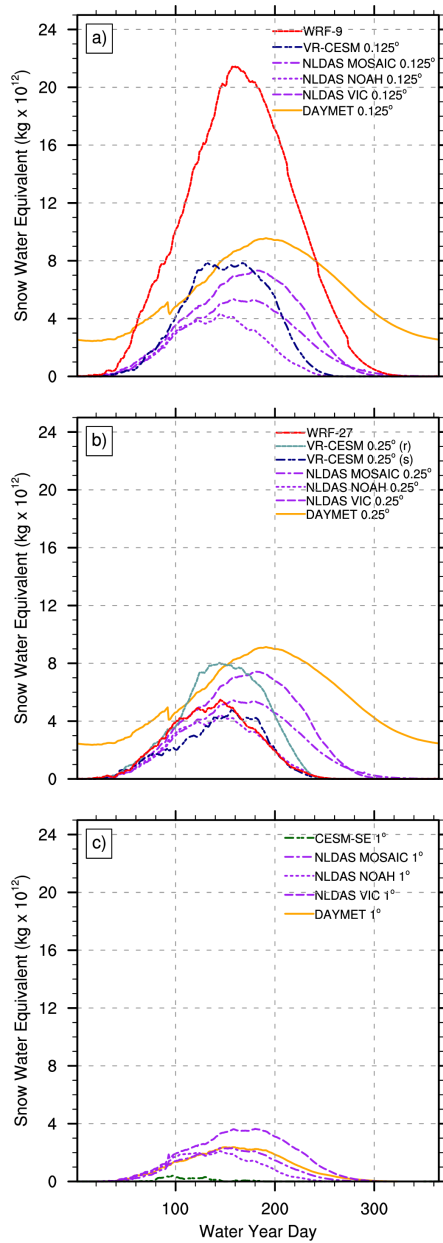
Figure 8: Average water year day totals for SWE within the Sierra Nevada SNOTEL subregion. Plots are sorted according to the resolution of the models - namely, (a) 0.125° (14km), (b) 0.25° (28km), and (c) 1° (111km). The Sierra Nevada SNOTEL station datast (19 locations) is plotted in black within each diagram. The horizontal axis represents Water Year Day (beginning October 1st through September 31st).

Figure 9: Normalized average SWE within the Sierra Nevada SNOTEL subregion. Plots are sorted according to the resolution of the models - namely, (a) 0.125° (14km), (b) 0.25° (28km), and (c) 1° (111km). The Sierra Nevada SNOTEL station dataset (19 locations) is plotted in black within each diagram. The horizontal axis represents Water Year Day (beginning October 1st through September 31st).
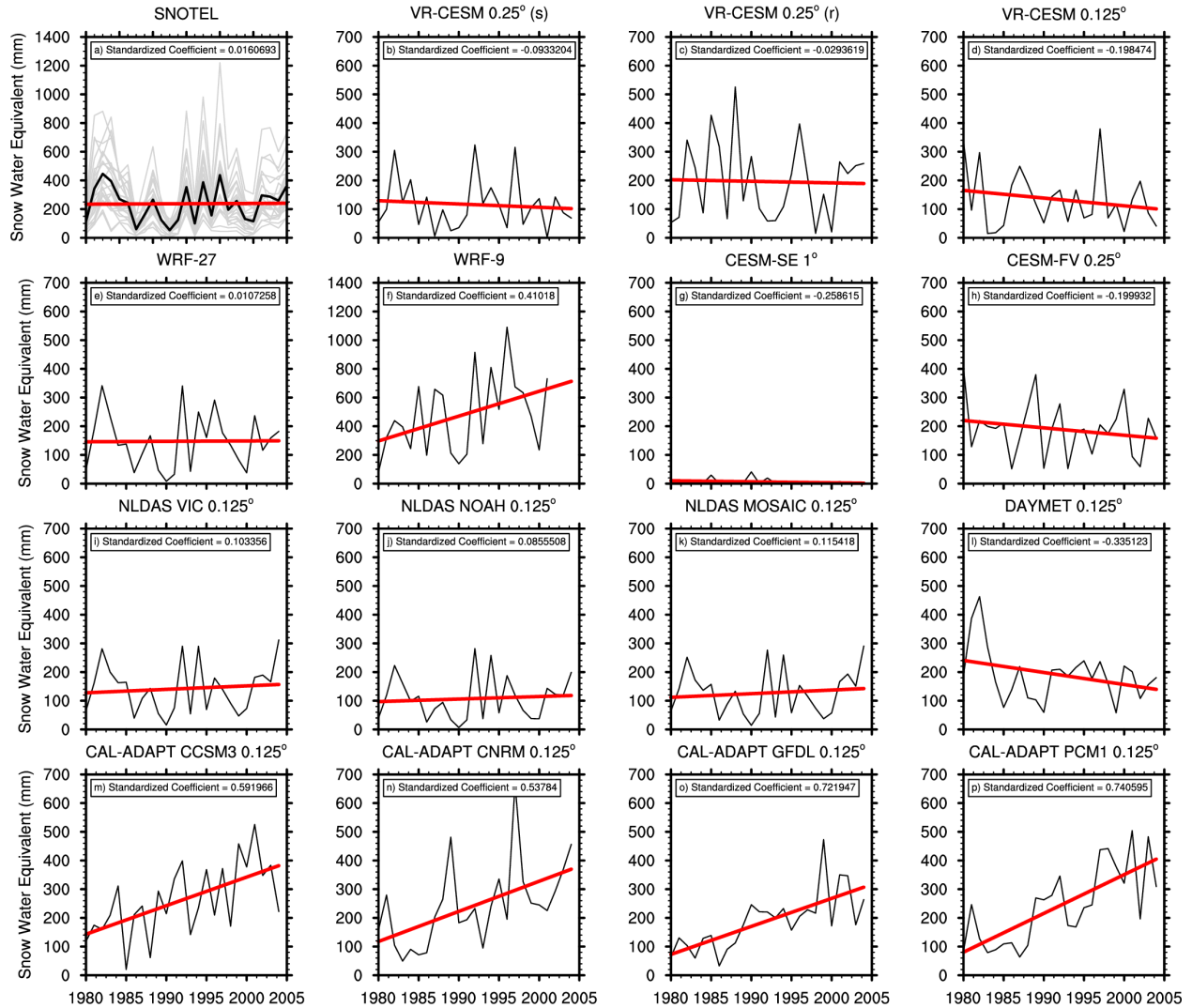
Figure 10: Linear trend in average seasonal DJF SWE within the Sierra Nevada SNOTEL comparison subregion across model, observational, and reanalysis datasets over the historical period (DJF season 1980 to 2005). The SNOTEL dataset, plot (a), incorporates 19 SNOTEL stations spread throughout the Sierra Nevada that contained 25 DJF seasons of observations. Gray lines indicate individual SNOTEL station with the average seasonal DJF SWE value represented by the black line. Standardized regression coefficient is shown in the upper left corner of each plot.
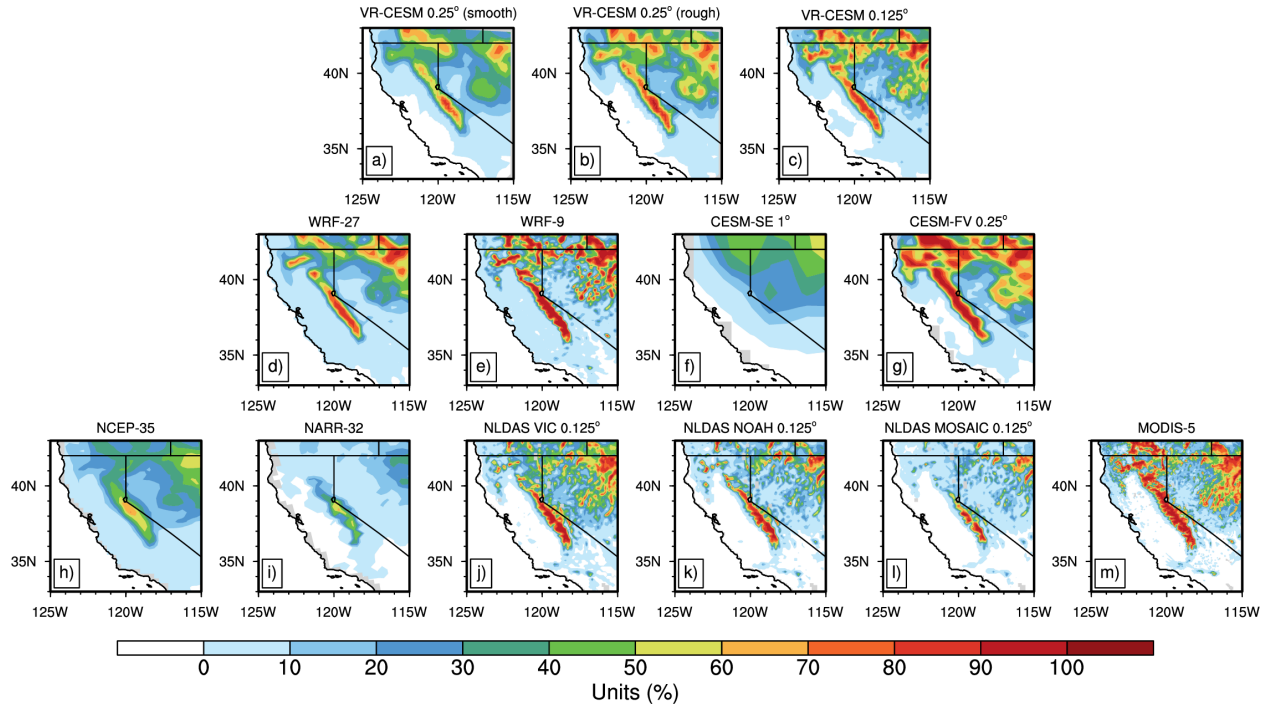
Figure 11: Average climatological DJF snow cover (SNOWC) across model, observational, and reanalysis datasets over California. The MODIS dataset spans the years 2000-2012.
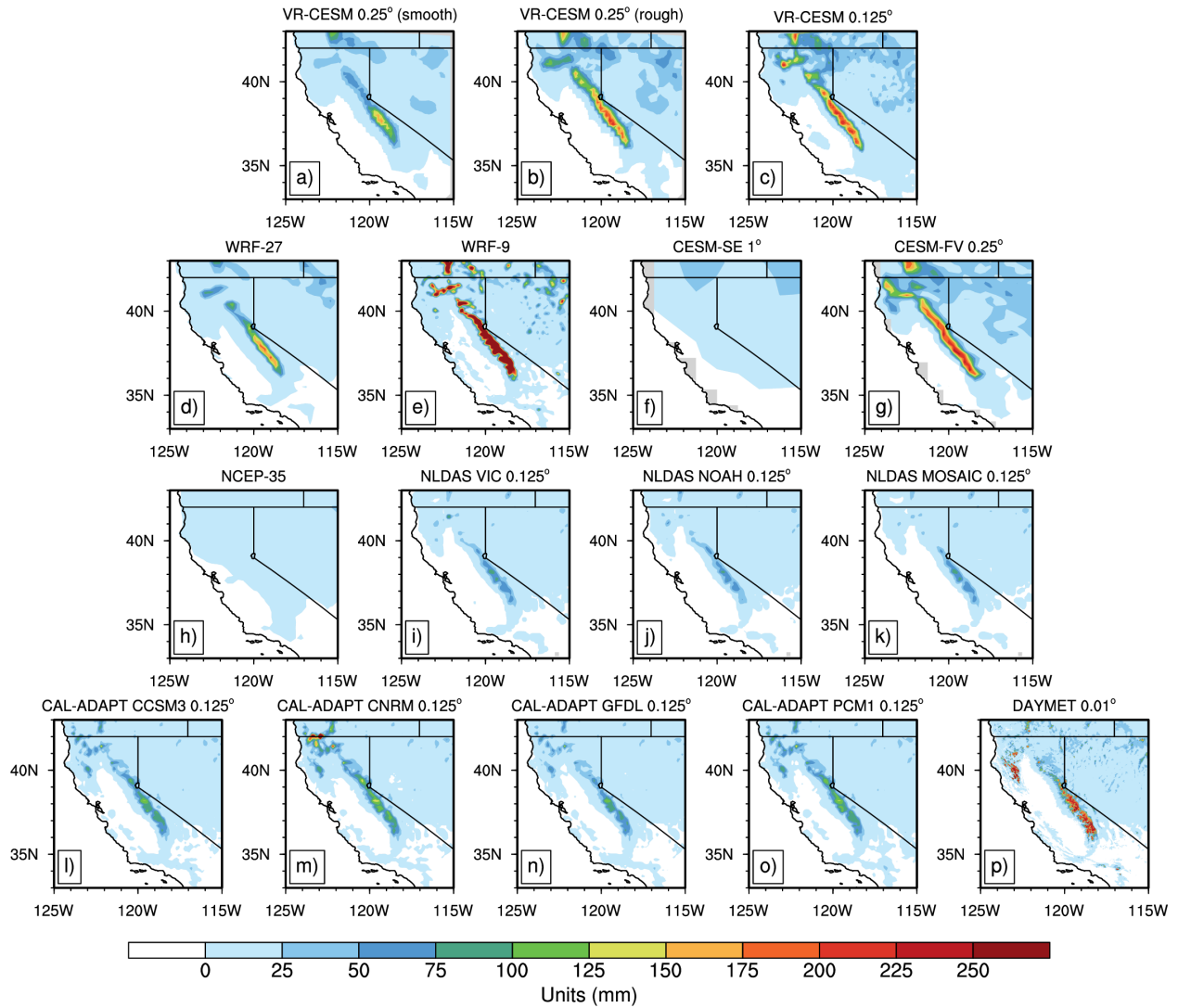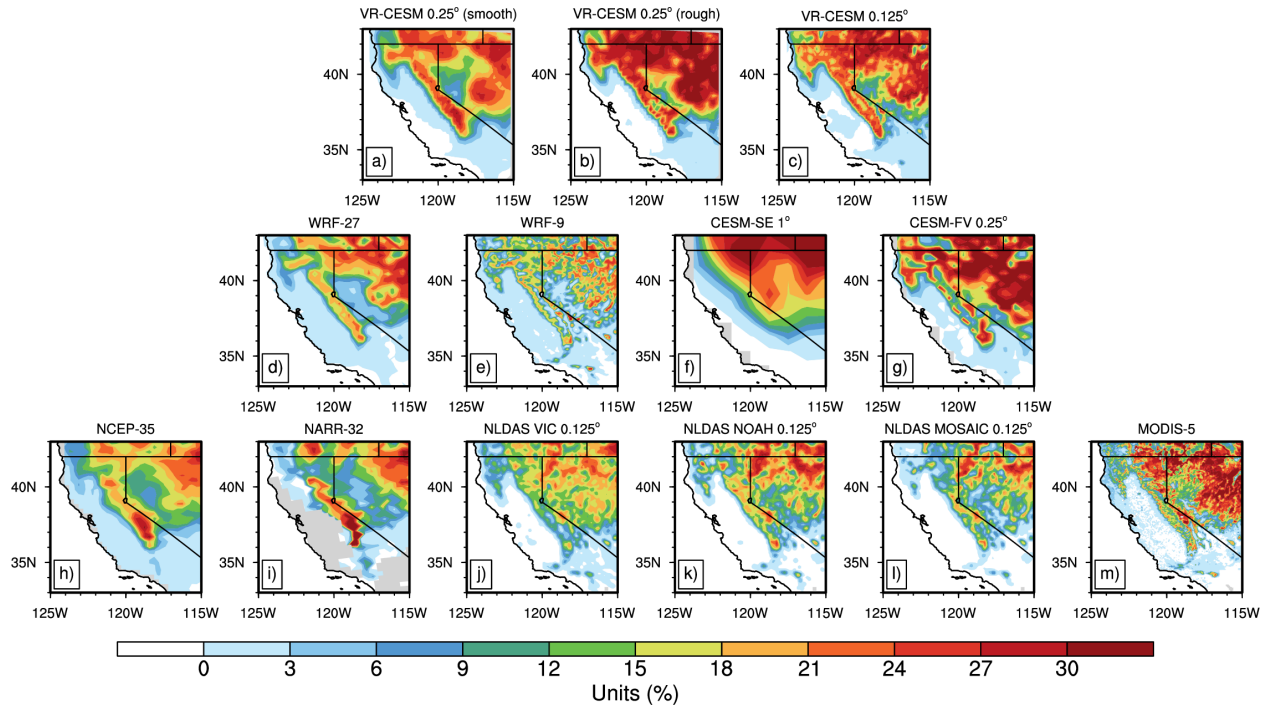

Figure 12: Average DJF variability (interannual standard deviation of the seasonal mean) of snow cover (SNOWC) across model, observational, and reanalysis datasets over California. The MODIS dataset spans the years 2000-2012.
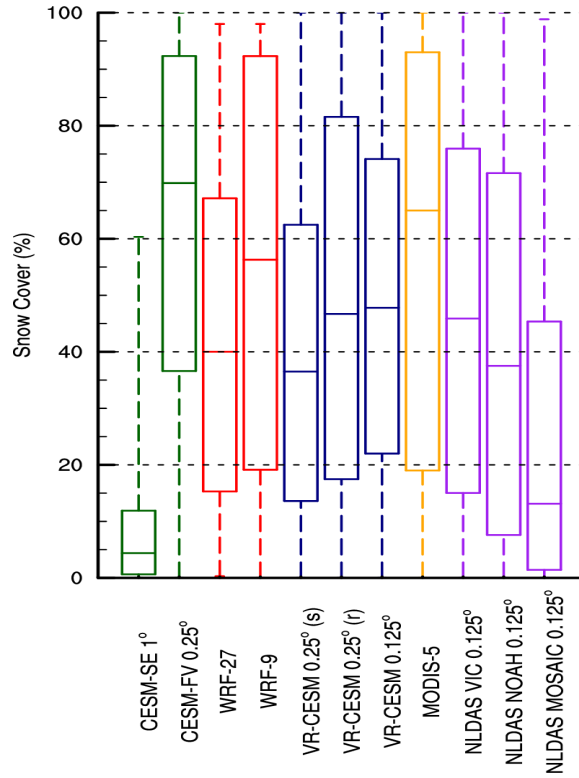
Figure 13: Boxplots of seasonal (DJF) Sierra Nevada snow cover (SNOWC) across modeling platforms and observational datasets. The boxes represent the 25th and 75th percentile values within the Sierra Nevada masked region, with the median value indicated in between. The minimum and maximum range is depicted by vertically dashed lines. Regridding of reanalysis datasets to $0.25°$ (or $0.125°$ for MODIS) had no noticeable effect on the statistics and so are not shown. The MODIS dataset spans the years 2000-2012.
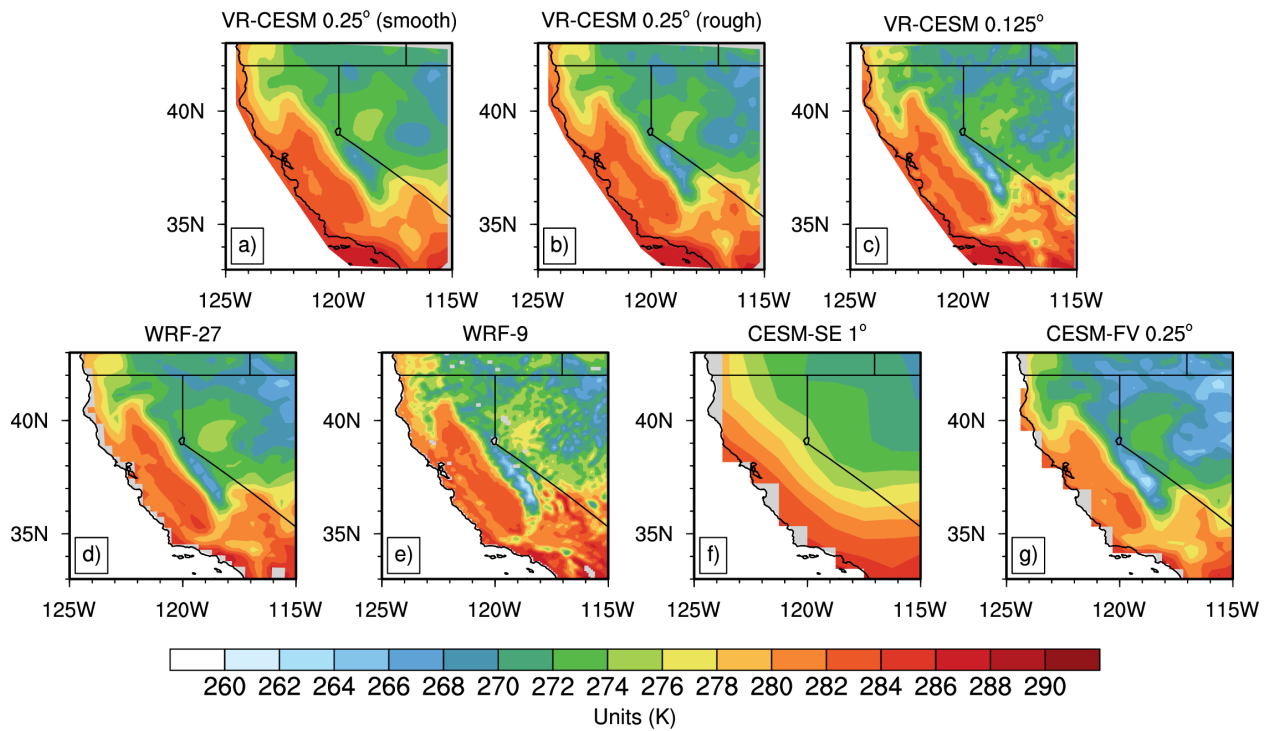
Figure 14: Average climatological DJF 2m surface temperature across model datasets over California.

Chapter 2 - Projecting 21st Century Snowpack Trends in Western USA Mountains Using Variable-Resolution CESM

Abstract

Climate change will impact western USA water supplies by shifting precipitation from snow to rain and driving snowmelt earlier in the season. However, changes at the regional-to-mountain scale is still a major topic of interest. This study addresses the impacts of climate change on mountain snowpack by assessing historical and projected variable-resolution (VR) climate simulations in the Community Earth System Model (VR-CESM) forced by prescribed sea-surface temperatures along with widely used regional downscaling techniques, the Coupled Model Intercomparison Projects Phase 5 Bias Corrected and Statistically Downscaled (CMIP5-BCSD) and the North American Regional Climate Change Assessment Program (NARCCAP). The multi-model RCP8.5 scenario analysis of winter season SWE for western USA mountains indicates by 2040-2065 mean SWE could decrease -19% (NARCCAP) to -38% (VR-CESM), with an ensemble median change of -27%. Contrary to CMIP5-BCSD and NARCCAP, VR-CESM highlights a more pessimistic outcome for western USA mountain snowpack in latter-parts of the 21st century. This is related to temperature changes altering the snow-albedo feedback, snowpack storage, and precipitation phase, but may indicate that VR-CESM resolves more physically consistent elevational effects lacking in statistically downscaled datasets and teleconnections that are not captured in limited area models. Overall, VR-CESM projects by 2075-2100 that average western USA mountain snowfall decreases by -30%, snow cover by -44%, SWE by -69%, and average surface temperature increase of +5.0 °C. This places pressure on western USA states to preemptively invest in climate adaptation measures such as alternative water storage, water use efficiency, and reassess reservoir storage operations.

Introduction

The 21st century will continue to see unprecedented and irrefutable changes to the climate system (Field et al, 2014). These trends are well understood at the global scale but can be difficult or impossible to use for informing conclusions at regional and/or local scales, in large part because of topographically-driven microclimatic effects. Unfortunately, the majority of presently available

climate projections using global climate models (GCMs) are constrained to resolutions of 1° for multi-decadal and large ensemble modeling endeavors (Taylor et al, 2012; Kay et al, 2015). In recent years there has been a push towards finer resolutions, and some long-term simulations have achieved resolutions of 0.5° to 0.25°; however, for many of these studies the output fields and focus are limited to a specific scientific inquiry (Wehner et al, 2010; J. L. Kinter et al, 2013; Bacmeister et al, 2014; Small et al, 2014; Harris et al, 2016). This resolution barrier has largely been due to constraints in computing power, simulation throughput and data storage. Thus, climate projections necessary for management and planning at the regional level are still needed.

The unmet need for local-scale data poses additional risks within the western USA where regional climate change is directly altering snowpack totals. Snowpack is intrinsic to western USA hydrology representing three-fourths of the freshwater supply (Palmer, 1988; Cayan, 1996). Under global climate change projections over the coming century, temperatures will continue to rise, snowpack totals will decline, higher precipitation-to-snowfall ratios will occur, peak snowpack accumulation will occur earlier in the season, record-setting low snowpack totals will continue to be set, and natural freshwater storage (i.e., snow water equivalent (SWE)) will continue to diminish (Mote et al, 2005; Bales et al, 2006; Barnett et al, 2008; Pavelsky et al, 2011; Kapnick and Hall, 2012; Pavelsky et al, 2012; Salzmann and Mearns, 2012; Wise, 2012; Ashfaq et al, 2013; Diffenbaugh et al, 2013; Pierce and Cayan, 2013; Rupp et al, 2013; Berghuijs et al, 2014; Klos et al, 2014; Berg et al, 2015; Lute et al, 2015; Belmecheri et al, 2016). This will impact both the timing and magnitude of summer streamflows, which are essential in meeting agricultural water demand, providing a steady energy supply, and sustaining ecosystem function. For example, the 2014-2015 snow season was the driest year on record in California (5% of normal) over a 500 year period (Belmecheri et al, 2016), with water reserves at record lows and repercussions felt throughout California, especially in low-income agricultural communities in the Central Valley such as the Tulare Basin. Snowpack decline is especially important in the western USA energy sector where renewables (e.g., hydroelectric power) provide 56% of generating capacity and energy development plans haven't included future climate impacts, potentially disrupting the ability of energy providers to consistently meet future electricity demand (Bartos and Chester, 2015). If anthropogenic emissions continue unabated, the drivers of hydroclimatic change could accelerate (Ashfaq et al, 2013), resulting in an increased

number of low-to-no snow total years (Diffenbaugh et al, 2013) by the late 21st century.

Climate change will directly impact mountain snowpack in three ways. First, warmer temperatures will lead to an earlier spring thaw, increasing spring season runoff from snowmelt and decreasing late summer water availability. Second, in accordance with the Clausius-Clapeyron relationship, warmer air holds more water and so leads to potential increases in large-scale precipitation in areas with forced orographic uplift and warmer temperatures also tend to favor rainfall over snowfall. This is of particular importance to the western USA where 20-40% of precipitation events occur at or around freezing (-3 to 0°C) (Bales et al, 2006), making snowfall particularly susceptible to end-of-century projections of warming between +1.4 to 5.4 °C (National Climate Assessment, accessed 2016). Along the leeward (eastern) portion of the Sierra Nevada, an increase of 6°C would threaten the majority of Sierra Nevada snowpack (above 3000 m) and a 2°C increase could shorten the snow season by a full month (Bales et al, 2014). Rising surface temperatures are particularly important in the spring months at mid- to high-elevations, which would normally be below freezing throughout the winter period (Cayan, 1996; Stewart, 2009). These changes are further enhanced by the snow-albedo feedback, which plays a pivotal role in determining the local and global radiative balances (Anderson, 1976; Hall, 2004; Qu and Hall, 2014). The global radiative forcing associated with this feedback, shown in recent GCM simulations for the IPCC (CMIP5), was found to be between 0.03 to 0.16 $W/m^2/K$ (Qu and Hall, 2014). Although not as substantive as the cloud-albedo (-0.55 W/m^2) and aerosol (-0.27 W/m^2) feedbacks, the snow-albedo feedback is nonetheless important, especially in the northern latitudes (Field et al, 2014).

Regional climate models (RCMs) have been an instrumental stopgap in addressing the discrepancy between coarse-resolution global simulations and the need for local-scale climate information. However, these models have their own limitations (and associated uncertainties) derived from the necessity of using a GCM forcing dataset (bias propagation), lateral boundary relaxation strategies (introducing artificial noise), and lack the global-to-regional dynamic coupling that may be required to understand multi-decadal climate change feedbacks, such as atmosphere-ocean teleconnections. Methods such as bias correction have been employed to alleviate some of the uncertainty associated with coupling global datasets with regional models (Ashfaq et al, 2013; Pierce and Cayan, 2013), but

these corrective techniques are often only applicable in a limited context and are difficult to apply to future projections without assuming stationarity (i.e., that historical trends can describe future trends; Velázquez et al (2015)), or adding compensating biases (Cannon et al, 2015; Pierce et al, 2015). Statistical downscaling has also been useful for generating climate data at high resolutions, and has been invaluable to management and planning organizations due to its low computational cost (Groves et al, 2008; Maurer et al, 2010; Pierce et al, 2013; Chen et al, 2014c; Berg et al, 2015). However, statistical downscaling typically relies on stationarity assumptions which may not hold under a changing climate. Further, it has been shown that using relatively coarse GCM data can lead to incorrect statistical inference and biased regional information, especially for precipitation (Chen et al, 2014c; Berg et al, 2015) due to differences in seasonality and phenomenon causing extreme precipitation at different GCM resolutions (van der Wiel et al, 2016). Thus, the development of accurate regional climate change projections remains a major scientific problem and the associated uncertainties associated have yet to be fully constrained, especially in the hydrologic sector (Groves et al, 2008).

To advance the scientific understanding on this topic, and further constrain the magnitude, extent, and spatial distribution of snowpack change, the authors have utilized a global-to-regional downscaling technique known as variable-resolution (VR) within the Community Earth System Model (VR-CESM). This technique utilizes a global coarse resolution grid which is then horizontally refined over a specific area of interest; hence, VR-CESM often requires 10% of the computing power of a conventional uniform resolution global model simulated at high resolution. VR capabilities have now been incorporated in operational GCMs across many major modeling centers (Skamarock et al, 2012; Harris and Lin, 2013; Zarzycki et al, 2014b; McCorquodale et al, 2014). To date, VR has been proven effective for assessing regional climate (Rauscher et al, 2013; Huang et al, 2016; Rhoades et al, 2016; Huang and Ullrich, 2016), large-scale weather systems (Rauscher and Ringler, 2014), and tropical cyclones (Zarzycki and Jablonowski, 2014; Zarzycki et al, 2014a, 2015). The multi-scale approach of VR-CESM allows it to serve as a bridge between GCMs and RCMs and overcome many of the known issues with conventional downscaling methods. Namely, VR has the ability to provide high-resolution in a desired area, eliminates multi-model lateral boundary forcings (and propagated bias) used in conventional global-to-regional modeling pursuits, captures global

teleconnections, and has a higher simulation throughput and smaller data storage demand when compared to standard uniform-resolution GCMs. Added benefits of VR-CESM are also discussed in greater detail in Rhoades et al (2016), where multi-year climate integrations were performed using a small university server (<1000 cores), with 20-40 day turnarounds on 25 year simulation periods at resolutions of 0.25° (28 km) to 0.125° (14 km). The VR grid used for this study focuses on the western USA and is shown in Figure 15, telescoping from a globally quasi-uniform 1° resolution to a refined 0.25° region. Like other downscaling strategies, VR-CESM sub-grid-scale physics are still being vetted down to extremely high-resolutions (i.e., <28 km) to assess scale sensitivity (Zarzycki et al, 2014b) and, currently, VR-CESM is not supported to be run at non-hydrostatic (<10 km) scales. Therefore, if VR-CESM data is to be used for assessment and planning at local scales it may be advantageous to use a bias-correction technique prior to using the VR-CESM data in any impact study.

The structure of the remainder of the paper is as follows: Section 2 contains information about the experimental design including specifications about VR-CESM, the VR-CESM forcing datasets, and the ensemble of datasets used to intercompare the magnitude, extent, and spatial distribution of change facing western USA snowpack totals in relation to VR-CESM. Section 3 highlights the pre-2005 climate daily average comparisons between the various datasets to identify potential bias originating from structural uncertainties. Section 4 presents the graphical and statistical intercomparion of SWE between the global-to-regional datasets. Section 5 provides a more comprehensive analysis of VR-CESM snowpack trends at both seasonal and multidecadal time frames. Lastly, section 6 discusses conclusions and future work.

Experimental Design

CESM Specifications

The Community Earth System Model (CESM), version 1.2.2, was utilized for this research. CESM is a widely-used and community-supported climate model developed at the National Center for Atmospheric Research (NCAR) and the US Department of Energy (DoE). Representations of each of the major Earth system components, including the atmosphere, land surface, land-ice, ocean, ocean-wave, river run-off and sea-ice, are available in CESM. This study used the F-component

set, FAMIPC5, which is standard practice for the Atmospheric Model Intercomparison Project (AMIP) (Gates, 1992). The F-component set couples the prognostic atmosphere (Community Atmosphere Model version 5.3, CAM5) (Neale et al, 2010) and land-surface (Community Land Model version 4.0 with satellite phenology, CLM4-SP) (Oleson et al, 2010) while using prescribed sea-surface temperatures (SSTs) and sea-ice extent in place of dynamic ice and ocean models. The use of prescribed SSTs allows for more accurate surface forcing when compared to simulations with dynamic ocean and sea-ice and reduces computational and data storage space requirements.

Within CAM5, the Spectral Element (CAM5-SE) dynamical core was used for this work (Taylor et al, 1997; Dennis et al, 2012). CAM5-SE is built with a continuous Galerkin spectral finite-element method to solve the hydrostatic atmospheric primitive equations. CAM5-SE has several demonstrable benefits compared with the other CAM dynamical cores, including unstructured grid support that eliminates grid singularities at higher latitudes, and near-perfect multi-processor scalability (Taylor and Fournier, 2010; Dennis et al, 2012; Zarzycki et al, 2014a,b; Zarzycki and Jablonowski, 2014). Physical parameterizations in CAM5, which simulate forcing due to sub-grid scale processes, include aerosols (Ghan et al, 2012), deep convection (Neale et al, 2008), macrophysics (Park et al, 2014a), microphysics (Morrison and Gettelman, 2008), radiation (Iacono et al, 2008), and shallow convection (Park and Bretherton, 2009). Further details regarding CAM5-SE can be found in Neale et al (2010).

CLM4-SP uses a subdivision scheme to represent the heterogeneous distribution of glaciers, lakes, urban landscapes, vegetation, and wetlands (Oleson et al, 2010; Lawrence et al, 2011). To accurately describe each grid cell's unique land surface distribution, the Moderate Resolution Imaging Spectroradiometer (MODIS) satellite data at 0.5° resolution is used for vegetation and high-resolution surface datasets for soil types, urban expanse, and water bodies. The satellite-derived values for vegetation are aggregated into 16 unique Plant Functional Types (PFTs), including non-vegetated. A detailed PFT representation within each land-unit is critical in capturing snowpack trends, as interactions between the canopy and snowpack are PFT specific for biogeochemical, radiative, and hydrological processes such as interception, throughfall, canopy drip, water removal via transpiration, and optical property interactions based on leaf angle (Lawrence et al, 2011).

The CLM4-SP snowpack model is based on several well established methods including Anderson (1976), Jordan (1991), and Yongjiu and Qingcun (1997). The snowpack model is regarded as one of the more complex (Cai et al, 2014) and is among the best at representing key snowpack variables, such as SWE (Chen et al, 2014b), in the suite of available coupled land-surface models. This is due, in large part, to the discretization of five distinct snow layers that dynamically compact and exchange energy and water. The five-layer model simulates the total life cycle of snowpack including aging and compaction, black carbon and mineral deposition, ice mass, layer thickness, optical properties, temperature profiles, and, importantly for water resources, water mass. As shown, CLM4-SP accounts for many of the key drivers and processes that influence the snowpack life-cycle, however the CLM4-SP snowpack module does have limitations in its ability to represent peak snowpack timing (too early) and melt rate (too fast), especially when compared to point-location in-situ observations (Chen et al, 2014b; Toure et al, 2016; Rhoades et al, 2016).

VR-CESM Forcing Datasets

For the VR-CESM simulations, historically prescribed SST and sea-ice fractions were derived from the Hadley Centre sea ice and SST dataset version 1 (HadISST1) and version 2 of the National Oceanic and Atmospheric Administration (NOAA) weekly optimum interpolation (OI) SST analysis (Hurrell et al, 2008) and the future SSTs and sea-ice forcings were derived from a future 1° RCP8.5 bias-corrected dataset (Small et al, 2014), both of which were developed at NCAR. The bias-correction compares simulated and observed SSTs and assumes that model errors from the historical simulation will be similarly present in future simulations (i.e., quantile mapping). After the bias-correction is applied, the SST and sea-ice fractions were then assessed and quality controlled to ensure consistency between temperature and fractional area coverage were satisfied. Careful consideration of how to best represent future SSTs and sea-ice are crucial as they influence ocean-forced teleconnections that are simulated by the global dynamic atmosphere-land framework of VR-CESM. Teleconnections are key drivers of regional scale variability in western USA wintertime precipitation and snowpack trends (Wallace and Gutzler, 1981; Glantz et al, 1991; Dettinger and Cayan, 1995; Cayan, 1996; Cayan et al, 1999; Pandey et al, 1999). Importantly, several studies have shown that CESM has skill in representing the El Niño Southern Oscillation (ENSO) (DeFlorio et al, 2013; Wang et al, 2014), the Pacific Decadal Oscillation (PDO) (DeFlorio et al, 2013), and

the Pacific-North American (PNA) pattern (Li and Forest, 2014), all important for the western USA. These teleconnection representations are expected to carry over into VR-CESM.

VR-CESM Model Grid and Topographical Fields

The VR grid was generated using SQuadGen (Ullrich, 2014), which uses paving to apply localized refinement to a basic equiangular cubed-sphere followed by spring dynamics for smoothing. An identical grid is used for both CAM and CLM in this research (Figure 15). To generate the topography for the VR-CESM28 simulation, the ETOPO2v2 (2 km resolution) satellite derived dataset was employed (National Geophysical Data Center, 2006). Due to the high-order properties of the dynamical core, smoothing is required to avoid spurious high-frequency noise from the sampled topography. Thus, the original ETOPO2v2 dataset resolution (2km) was regridded and smoothed slightly beyond the native VR grid resolution (28km) for numeric stability. This particular issue was discussed in Zarzycki et al (2015) where excessive terrain roughness in CAM5-SE was shown to produce spurious vertical velocities and numerical artifacts. Therefore, to alleviate this artificial noise the c parameter from Eqn. (1) in Zarzycki et al (2015) was used to smooth the ETOPO2v2 topographic dataset along with repeated applications of fourth-order hyperviscosity. This process produces a topographic representation of the western USA with more smoothing applied in regions of coarser grid resolution. The resulting topography is a vast improvement over the excessively smoothed topography typically employed by $1°$ uniform-resolution GCMs (Figure 16).

Statistical Methods

A key objective of this assessment is to understand the snowpack trends produced by VR-CESM28 from the 2025-2100 and compare them to widely-used GCM and RCM ensembles. A tabulation of the established climate change datasets used for this intercomparison can be found in Table 6. To standardize the various datasets, Climate Data Operators (CDO), NetCDF Operators (NCO), and the NCAR Command Language (NCL) were used (Schulzweida et al, 2007; Zender, 2008). The climate and seasonal averages were computed using a mask of the Cascades, Klamath, Rockies, Sierra Nevada, and Wasatch and Uinta (see Figure 17). These masks were derived from the EPA's Ecoregions classification system (Ecoregion Level III).

The datasets were further remapped to similar map projections and to the highest resolution needed for proper intercomparison (i.e., 4km for pre-2005 PRISM comparisons and 14km for NLDAS/BCSD-CMIP5 RCP8.5 climate change comparisons). Remapping from coarser to finer horizontal resolution was chosen to allow for equal comparisons between western USA mountain shapefile masks without degrading high-resolution spatial information and to ensure that proper statistical sampling of 250m to 500m elevational band trends could be made. To do this, the Earth System Modeling Framework (ESMF) capabilities in the NCAR Command Language (NCL) and TempestRemap (Ullrich and Taylor, 2015; Ullrich et al, 2016) software suites were used. Summary statistics for the five mountain ranges were calculated for each of the datasets, including mean, standard deviation, lower quartile, median, upper quartile, and maximum. The Wilcoxon-Mann-Whitney Rank-Sum Test was applied to assess statistical significance of differences between time periods.

Climate Change Datasets Used for Western USA Intercomparison

To robustly assess the range of potential outcomes that the RCP8.5 scenario may have on western USA mountain snowpack an intercomparison of the various modeling methodologies (e.g., dynamical, statistical and traditional GCM) was conducted. The datasets were chosen based on public availability and use in the literature. Brief descriptions of the various climate datasets are outlined below.

VR-CESM28 was executed on the local UC Davis Climate Cluster from 1980-2005 and 2025-2100, under the IPCC RCP8.5 scenario. Daily average outputs were created for select variables in CAM and CLM, including those featured in the analysis of this paper. Additional climatological simulations have been produced by varying the initial conditions, but are not included in this analysis (Rhoades et al, 2016; Huang et al, 2016; Huang and Ullrich, 2016). Importantly, in the VR-CESM analyses mentioned it was found that it takes approximately 20-30 DJF simulated months (seven to 10 simulated years) for the median California precipitation trends to converge around a median value (across a multitude of VR-CESM resolutions). Thus, it is inferred that these trends will hold throughout all western USA mountain ranges and the 26 year historical baseline simulation is sufficient to ensure that natural variability (e.g., ENSO and PDO) is taken

into account.

The Coupled Model Intercomparison Project, Phase 5, (CMIP5) incorporates over 20 modeling centers worldwide. For the model intercomparison, the eight CESM family ensemble members were utilized to create an ensemble average. The ensemble consists of six Community Climate System Model (CCSM) 4.0 members (an earlier version of CESM), one CESM1 Biogeochemistry (BGC) member (the full carbon cycle version of CESM), and one CESM1 CAM5 member (the latest production version of CESM).

The North American Regional Climate Change Assessment Program (NARCCAP) is an RCM ensemble composed of a matrix of five driving GCMs with six RCMs over the Continental United States (CONUS) at 0.5° (55 km) resolution (Mearns et al, 2009). In Phase I (Mearns et al, 2012), pre-2005 simulations (1970-2000) were performed and in Phase II (Mearns et al, 2013), the future projections (2040-2070) were simulated. All of the available RCM-GCM coupled members were utilized to create an ensemble average for the intercomparison.

The Downscaled CMIP3 and CMIP5 Climate and Hydrology Projections dataset consists of an ensemble of model projections using a monthly bias-corrected and spatial disaggregation (BCSD) technique (Maurer et al, 2007; Brekke et al, 2013). For the CMIP5 hydrologic projections (BCSD-CMIP5), the BCSD method was utilized along with the use of the Variable Infiltration Capacity (VIC) hydrologic model, version 4.1.2, to provide 0.125° (14 km) resolution model outputs for both pre-2005 (1970-2000) and future (2040-2070) timeframes. Three of the CESM family ensemble members (i.e., CCSM4, CESM1 BGC, and CESM1 CAM5) were used to create an ensemble average for the model intercomparison.

The North America Land Data Assimilation System Phase 2 (NLDAS) reanalysis dataset was created via the incorporation of observational and model reanalysis datasets into three non-atmosphere coupled land-surface models (i.e., NASA's Mosaic Land Model, NOAA's Noah Land Model, and Princeton's implementation of the VIC Land Model) over the continental United States at 0.125° (14 km) resolution for the years 1980-2005 (Xia et al, 2012b,a). Rhoades et al (2016) showed that the NLDAS ensemble closely approximated the SWE lifecycle (i.e., accumulation, peak timing, and

melt rate) of 19 SNOTEL stations in the central Sierra Nevada over 1980-2005, warranting its use in this current analysis.

The Parameter-elevation Relationships on Independent Slopes Model (PRISM) was developed at Oregon State University and consists of a spatially continuous high-resolution (800m and 4km) dataset spanning 1970 to present day for the United States (Daly et al, 2008). Using a digital elevation model (DEM), 13,000 precipitation and 10,000 temperature observational stations, and several key regional climate indicators (i.e., location, elevation, coastal proximity, topographic orientation and position, vertical atmospheric layer, and terrain slope) the PRISM precipitation and surface temperature dataset was constructed. Of interest to western USA hydroclimatological research in coastal and mountainous regions, PRISM showed great improvement compared to other reanalysis datasets (e.g., Daymet and WorldClim) due to its better characterization of coastal effects, cold air drainage, elevational gradients, inversion layers, and rain shadows in these environments (Daly et al, 2008). Although PRISM is widely regarded and used in the mountain climate community it still has known biases, particularly over the California Sierra Nevada at high-elevations on windward facing slopes, when streamflow observations are utilized as a check on the PRISM total water mass balance (Henn et al, 2016).

It should be cautioned that all of the SWE datasets available have inherent bias. This is due to the use of land-surface models to address the discontinuity of in-situ measurements which only represent a small sub-sample of the total snow covered area. Thus, they should not be viewed as exact "truths". Interestingly, a few new high-resolution spatially continuous observational datasets are becoming more readily available for select mountain regions (in particular the Sierra Nevada and Rockies), but at this time are not yet publicly available. These datasets utilize new techniques including an 50m resolution airplane lidar measurement (Painter et al, 2016) and a Landsat-era reanalysis product that utilizes the remotely sensed fractional snow cover area along with Bayesian statistical inference techniques to derive a 90m spatially continuous product (Margulis et al, 2016a,b).

Hydroclimate Trends in Western USA Mountain Ranges within VR-CESM28

Constraining historically simulated model bias is important in understanding how to best represent the processes governing mountain snowpack within a model. To this end, the VR-CESM28 1980-2005 simulation is assessed against the best available datasets for all western USA mountain ranges regions for total precipitation (PRECT), SWE, and two-meter surface temperature (2mST). Positive (negative) simulated model biases compared to the 4km-resolution PRISM data are highlighted in Figure 18 in blue (red) for daily climate averages of accumulated PRECT and 2mST. For SWE, several datasets are presented, including the NLDAS three-member ensemble (14 km), the NARCCAP nine-member ensemble (55 km) and the three-member BCSD-CMIP5 ensemble (14 km).

PRISM, used for PRECT and 2mST, is both a widely used and high quality reanalysis dataset for mountainous regions. Agreement between VR-CESM28 and PRISM is apparent for accumulated daily climate average precipitation in the western USA mountains. A slight positive bias is apparent and consistent across most mountain ranges, but the bias is low, with peak accumulated precipitation of 818 mm for PRISM and 872 mm for VR-CESM28 (+7% bias). Otherwise there is general agreement within the 1980-2005 daily climate normal accumulated precipitation rates for the entire western USA mountain region. Within individual mountain ranges, the Klamath had the highest negative bias (-16%), which can be attributed to the Klamath being the smallest mountain range within the western USA with rapidly varying orography that is poorly represented even at 28km.

A wide spread among different models is apparent in total simulated SWE, indicative of the difficulty in accurately representing mountainous precipitation deposition and phase as well as the life cycle of mountain snow processes. This variability in simulated vs observed SWE is in part due to the fact that snowpack datasets at sufficiently high resolution and quality are non-existent (notably, models from both the NLDAS and NARCCAP ensemble exhibit unphysically persistent SWE even through the summer season). As highlighted in Rhoades et al (2016), the NLDAS three-member ensemble was found to be one of the best quality datasets when compared to 19 SNOTEL stations in the Sierra Nevada; however, this may not hold throughout the western USA as each mountain range

has a distinct character with respect to aspect, orientation, slope, proximity to the ocean, source precipitation region, and vegetation cover. Thus, it is particularly difficult to assess bias in SWE with no accurate and validated "truth". Nonetheless, it is encouraging to observe that VR-CESM28 appears to fall in the mid-range of the available high-resolution datasets. VR-CESM28 had a peak DJF average accumulation SWE value of 135 mm within the total western USA mountain region, well within the range of values shown by other regional downscaling techniques. The three-member NLDAS ensemble had the lowest peak DJF average accumulation SWE value at 73 mm, followed by the NARCCAP nine-member ensemble at 148 mm and the BCSD-CMIP5 at 172 mm (although this value was derived from monthly, rather than daily averages). As noted by Rhoades et al (2016), VR-CESM28 also tends to have a early peak accumulation bias associated with an enhanced melt rate leading to total melt occurring too early.

For 2mST, VR-CESM28 generally shows an enhanced seasonal cycle with increased bias in summer (JJA, max of +1.9 °C) and winter (DJF, min of -2.7 °C) throughout the western USA mountain region, except for the Klamath region where a cold bias is found throughout (min of -2.1 to max of -2.7 °C). For the 2025-2050 period, the VR-CESM28 RCP8.5 simulation still oscillates within the range of bias for PRISM 2mST, however over the 2075-2100 period temperature values are well outside the 1980-2005 range for simulation bias. This suggests that the climatological signal by end-of-century is beyond the range associated with model bias. The amplified end-of-century warming leads to dramatic reductions in western USA mountain SWE (-69%), with an associated earlier peak snow accumulation and complete melt a month earlier (May), a slightly amplified total accumulated precipitation (+15%), with more rain and less snow (discussed later), and an amplified minimum (+5.8 °C), average (+5.0 °C), and maximum (+4.9 °C) 2mST.

SWE Climate Change Dataset Intercomparison for the Western USA

To quantify the magnitude and variability of changes in snowpack (SWE) and how VR-CESM28 fits among already widely used downscaling strategies, the VR-CESM28, BCSD-CMIP5, NARCCAP, and CMIP5 climate change datasets were assessed over their overlapping simulation temporal range of 2040-2065 (under RCP8.5) for SWE within the five major western USA mountain ranges. For each of the datasets only CESM derived ensemble members were used, save for NARCCAP where

all ensemble members were used. Each of the datasets were separately averaged over their pre-2005 and 2040-2065 periods. Summary statistics across the four global-to-regional downscaling datasets are provided in Table 7 and the pre-2005 vs 2040-2065 percent change summary statistics are provided in Table 8.

The winter season (DJF) climate average for each dataset is plotted in Figure 19. The datasets all highlight a net-negative change in SWE by 2065, although the magnitudes of change and seasonal variability exhibit some differences. The net change in SWE among the three regional datasets varied from -19% (NARCCAP) to -38% (VR-CESM28). Individual mountain ranges exhibited even more variation in the near-coastal regions (e.g., Cascades and Klamath) with the Klamath showing the most disagreement. The Cascades, Klamath, and Sierra Nevada mean net-SWE loss ranged from -36% (BCSD-CMIP5) to -63% (VR-CESM28), -22% (BCSD-CMIP5) to -74% (VR-CESM28), and -30% (BCSD-CMIP5) to -60% (NARCCAP), with an ensemble mean change of -50%, -49%, and -44%, respectively. Conversely, more resiliency in snowpack to climate change was seen in the interior mountain ranges (e.g., Rockies and Wasatch and Uinta) across all of the regionally downscaled datasets with net-average changes in SWE ranging from -8% (NARCCAP) to -33% (VR-CESM28) and -21% (NARCCAP) to -41% (BCSD-CMIP5), with an ensemble mean change of -20% and -33%.

The ensemble of CMIP5 simulations poorly characterize the magnitude of 1980-2005 SWE depths (maximum depth of 18.9 mm) and thus highlight an inaccurate and dramatic change (-69%) in SWE totals by 2065. This is largely a consequence of the poor topographic representation which inhibits orographic precipitation and an inaccurate 0 °C isotherm.

Winter season (DJF) variability (standard deviation) for SWE is plotted in Figure 19 and quantified in Table 8. Compared to the pre-2005 time-frame, most datasets and mountain ranges exhibit a diminished seasonal variability with an overall net-change in SWE variability ranging from +0.3% (NARCCAP) to -20% (BCSD-CMIP5), with an ensemble mean change of -9.4%. This effect was most pronounced in coastal ranges, especially in the Klamath which exhibited a net-change of -9.8% (BCSD-CMIP5) to -43% (VR-CESM28). This is explained by the negative shift in maximum SWE coupled with an overall collapse of the lower-to-upper quartile ranges in most of the regional

downscaling datasets, highlighted in the DJF seasonal averages in Figure 20. To further quantify this, uncentered Pearson pattern correlations were computed for the ratio of the DJF climate average and seasonal variability for pre-2005 and 2040-2065 for the entire western USA mountain region. Across all datasets, a high-correlation (>0.91) was found for the aforementioned ratio, indicating that a decrease in the climate average DJF SWE corresponds to a decrease in the seasonal variability (i.e., collapse of the interquantile ranges).

DJF Climate Trends in Snowfall, Snow Cover, SWE and 2mST in VR-CESM

Changes in SWE are a function of a number of topographically dependent variables including snowfall, snow cover, and 2mST (and their associated variabilities). To better understand the character of the western USA snowpack, the impact of climate change on these quantities must also be understood. Summary statistics for these quantities from VR-CESM28 are given in Table 9 and are only representative of the mountainous regions in Figure 17.

An assessment of the statistical significance (p=0.05) of the VR-CESM28 simulated winter (DJF) season frequency change for the 1980-2005 compared to the RCP8.5 2025-2050 and 2075-2100 simulation results within the western USA mountain region across all hydroclimate variables was performed using the Wilcoxon-Mann-Whitney Rank-Sum Test. This statistical significance test is useful for data that may not be normally distributed and helps to identify when significant changes associated with RCP8.5 begin to take effect on the simulated results. As can be seen in Table 9, significant (p<0.05) changes from the 1980-2005 PDFs for each of the hydroclimate variables are varied in the 2025-2050 results, but are unanimous in the 2075-2100 results across all mountain ranges. As expected, this implies a significantly more pronounced climate change signal by 2075-2100 compared with 2025-2050.

DJF climatological averages for snowpack variables are plotted in Figure 21 for 1980-2005, 2025-2050, and 2075-2100 under the RCP8.5 scenario in VR-CESM28. Additionally, the DJF seasonal average summary statistics are provided in Table 9 which represent only the mountainous regions depicted in Figure 17. The climatological anomalies (difference between 1980-2005 and post-2025) are plotted in the bottom two rows. Clear trends are seen throughout the western USA for all of the

hydroclimate variables, with an amplified trend by 2075-2100. For snowfall (d-e), a small decrease (-4%) is projected for the entire western USA mountain region by 2025-2050, with both positive (Intermountain West) and negative (Coastal Ranges) tendencies. By 2075-2100, the climate change signal is more apparent with an average decrease of -30% in total western USA mountain snowfall that is amplified along the Pacific coast due to a precipitation transition from snow-to-rain. This net decrease in snowfall helps to explain the substantial decrease in both snow cover (i-j) and SWE (n-o). As with snowfall, snow cover (-10%) and SWE (-25%) only exhibit a weak response to climate change through 2025-2050; however, by 2075-2100 average snow cover decreases by nearly half (-44%) and SWE by two-thirds (-69%) throughout the study domain. These changes are associated with an average increase in western USA 2mST anomalies (s-t) of +1.3 °C over the 2025-2050 period and +5.0 °C over the 2075-2100 period. Notably, there is a clear spatial signal in the surface temperature anomaly, with larger increases in average temperature at high elevation associated with elevation-dependent warming (discussed later).

An expected shift in precipitation phase from snow to rain has been posited throughout the literature due to climate change induced increases in air temperature (Bales et al, 2006; Berghuijs et al, 2014; Klos et al, 2014; Lute et al, 2015). This result is apparent in the VR-CESM28 simulations (Figure 22), which exhibit a clear shift from snow-to-rain (a-e) along with more wet snow deposition (f-j) (i.e., decreased liquid-to-snow ratio). The snow-to-rain plots (a-c) are DJF climate average ratios of snowfall over total precipitation and the liquid-to-snow ratio plots (f-h) are DJF climate average ratios of snow water equivalent to snow depth. 1980-2005 DJF climate average VR-CESM28 total precipitation was 3.5 mm/day and snowfall was 2.3 mm/day, but by 2025-2050 (2075-2100) DJF climate average total precipitation increased to 3.6 mm/day (4.00 mm/day) and DJF climate average snowfall decreased to 2.2 mm/day (1.6 mm/day). The alteration in the precipitation phase within the western USA mountainous region resulted in a -4% (-24%) drop in the snow-to-rain ratio by 2025-2050 (2075-2100) coupled with a mean increase in total precipitation of +7% (+20%). The statistical significance of the change in snow-to-rain and liquid-to-snow ratios for 2025-2050 were mixed in all of the mountain ranges; however, by 2075-2100 the statistical significance in these changes become unanimous across all mountain ranges at the p=0.05 and p=0.01 threshold. Sensitivity of coastal ranges to precipitation phase alterations was evident. By 2075-

2100, both the Cascades and Sierra Nevada showed a drop of -32% and -30% in their snow-to-rain ratios. A slightly wetter snowpack emerges as the DJF climate average liquid-to-snow ratio drops by -3%, with a decrease of -5% (lower quartile) to -11% (minimum) in parts of the study domain by 2075-2100.

Winter Season Variability in 2mST, Snowfall, SWE, and Snow Cover

Winter season snowpack interannual variability plays a crucial role in water resource planning in the western USA. An understanding of this variability is required to ensure sufficient water availability during inevitable drought periods. The DJF interannual variability from VR-CESM28 for the four hydroclimate variables of interest is apparent in Figure 23 for several of the western USA mountainous regions as a Hovmöller diagram of DJF latitudinal averages. The Hovmöller diagrams are useful in characterizing not only the seasonal variability, but the latitudinal dependence of these changes too. The anomalous deviations from the 1980-2005 DJF average are represented in each figure with the 1980-2005 time period on the left, a gap filled 2005-2025 in the middle (not simulated), and, finally, the RCP8.5 scenario results from 2025-2100 on the right. Anomalously high (low) DJF seasons compared to the 1980-2005 climate average are represented via blue (red), whereas the 2mST anomaly trend colors are flipped for reader intuition.

In Figure 23, historical (1980-2005) hydroclimate trends within the region oscillate from season-to-season about the mean with even distributions of high and low events. As the RCP8.5 climate change signal intensifies by the mid-to-end of century, a clear reduction in anomalously high winter season snowfall, snow cover, and SWE occurs with a coupled increase in anomalously high 2mST. Notably, by the 2050s anomalously high winter season snowfall, snow cover, and SWE become effectively non-existent with anomalously high 2mST ($+3$ °C to $+6$ °C) becoming the new normal. The anomalously high 2mST in the western USA mountainous region is correlated with the demise of snow cover.

Elevation-Dependent Warming

Elevation-dependent warming is associated with an increased warming signal in mountain regions due to a combination of the snow-albedo feedback, changes in vertical humidity profiles of the lower

atmosphere, and/or cloud-feedback processes (Group et al, 2015). To understand the character of this phenomena within our simulations, Figures 24 and 25 show 250m interval elevational profile plots of the DJF climate average and 500m elevational band trends for the DJF seasonal average time-series, respectively. For the 250m elevational profile plots, three selected mountain ranges (Cascades (e-h), Rockies (i-l), and Sierra Nevada (m-p)) are included with the total western USA mountainous region (a-d). These three mountains were selected as they represent the major mountainous regions for water management and each spans the largest range of latitudes within the western USA. Additionally, the 500m elevational band summary statistics were compiled in Table 10, along with the standardized regression coefficients, for each of the time-series and hydroclimate variable. Historically, it is the case that elevations with maximum snowfall often do not co-locate with maximum snow cover. In fact, western USA snowfall seems to be most pronounced around an elevation of ∼ 1000 meters (except for the Sierra Nevada), whereas snow cover increases approximately monotonically with elevation. The California Sierra Nevada trends may differ from the other mountain ranges of the western USA as it has a unique combination of atmosphere-ocean factors which could alter precipitation phase and deposition location. These features include its close proximity to the ocean, high perpendicularity to the coastline, highest elevations in the conterminous United States and precipitation trends dependent on the semi-permanent large-scale meteorological pattern (e.g., Aleutian Low), association with extreme meteorology (e.g., atmospheric rivers), and, in the southern portion, precipitation that is highly dependent on teleconnection patterns (e.g., the ENSO and the North American Monsoon).

Several hydroclimatic trends further emerge from this dataset. Examining Figure 24, although it is clear that the RCP8.5 climate change signal is much more apparent in the 2075-2100 DJF climate average than the 2025-2050 period, the actual impacts are not distributed uniformly across elevation categories. Throughout most of the western USA, only elevations below 2000m exhibit a clear climate signal with respect to snowfall (again except for the Sierra Nevada). Over the entire western USA mountainous region (a), peak average snowfall at 1250m elevation is diminished from 3.16 mm/day (1980-2005) to 2.87 mm/day (2025-2050), or -9%, and finally to 1.85 mm/day, or -41% (2075-2100). Interestingly, peak snowfall elevation (1250m) is maintained across all of the time-series in the total western USA mountainous region; however, in 2075-2100 the peak snowfall

magnitude is maintained over a broader range of elevation bands with a slight increase in snowfall at higher elevations compared to the 1980-2005 and 2025-2100 time periods. In response to the decrease in low-elevation snowfall, snow cover and SWE also decrease dramatically below $\sim$ 2000m. Higher elevations are also impacted by warmer surface temperatures which reduce snow cover and SWE, but these regions appear to be more strongly buffered against climate change.

Elevation-dependent warming is also apparent in the simulations as a consequence of the snow-albedo feedback. Namely, an increased DJF climate average 2mST warming emerges by 2075-2100 (Figure 24d) which is maximal around an elevation of 2000m (Figure 25). The freezing line (highlighted with a dotted line at 273.14 K) shifts upwards in elevation from 750m to 1500m from 1980-2005 to 2075-2100 within the total western USA mountainous region. However, the elevation-dependent sensitivity to increases in 2mST is not uniformly distributed. Interior mountain ranges (e.g., Rockies) maintain their freezing line at elevations that the coastal ranges (e.g., Cascades) showed an increased sensitivity to warming. For example, the 1980-2005 freezing line moved up in the Cascades from 750m to 1750m, in the Rockies from 500m to 1000m, and in the Sierra Nevada from 1500m to 2250m by 2075-2100. By 2075-2100, the Cascades' DJF climate average 2mST was above the freezing line throughout all elevations, with the Sierra Nevada showing a similar trend save for the highest elevation class.

The upslope shift in elevation of the freezing line directly impacted the snow covered area and, importantly, the stored water content (SWE) of the snowpack. From 1980-2005 to 2075-2100, the average accumulated SWE (i.e., stored water content or the area under the curve) is diminished by -21% by 2025-2050 and -63% by 2075-2100 within the total western USA mountain region. Further, 1980-2005 accumulated SWE diminished in the Cascades by -43% (-89%), in the Rockies by -22% (-63%), and in the Sierra Nevada by -18% (-82%) within 2025-2050 (2075-2100).

The 500m elevational band winter (DJF) climate average anomaly trends for 1980-2005 and 2025-2100 are plotted in Figure 25 and statistically summarized in Table 10. As anticipated with 2mST increases due to climate change, the largest decreases found in the VR-CESM28 simulations from 2025-2100 were at lower elevations, likely due to the phase shift from snow-to-rain seen in Figure 22 and upward shift in freezing line elevation. Resiliency of snowfall to climate change was shown

at higher elevations starting at around 2000m to 2500m where nominal positive or negative trends occurred. Elevational trends indicated a nonlinear negative change in snowfall of -10.7% from 2000m to 1500m, -16.6% from 1500m to 1000m, and, finally, -20.9% from 1000m to 500m. This was further shown in the standardized regression coefficients which steadily decreased towards negative one with every 500m decent with coefficients ranging from 0.04 (>3000m) to -0.64 (500-1000m).

As shown in Figure 25 (b-c), from 2025-2100 a clear negative trend in SWE and snow cover, regardless of elevation, was found. This is further shown in the standardized regression coefficients in Table 10. Interestingly, when compared to snowfall, both SWE and snow cover more linearly decreased downslope. Winter season average snow cover trends indicated a -5.7%/500m to -6.8%/500m, save for the change from 1000m to 500m of -18.9%/500m, and SWE trends showed a -11%/500m to -15%/500m.

Anti-correlated to the aforementioned trends, average winter season 2mST anomalies showed a steady increase and plateau upslope in the western USA mountain region (Figure 25). Average winter season 2mST anomalies highlighted a +0.97 °C from 500m to 1000m and then a more rapid increase of +2.85 to +3.81 °C from 1000m to >3000m. Further, the average maximum 2mST anomaly at the 500m to 1000m elevation band was +2.35 °C; whereas, the 1000m to >3000m ranged from +7.01 °C to +9.43 °C. As shown in Table 10, the magnitude of the interquantile ranges (i.e., an indication of seasonal variability) for 2mST increased by 101% to 210% from 1980-2005 to 2025-2100 from 1000m to >3000m and decreased by 30% from 500m to 1000m.

Discussion and Conclusion

Water managers, particularly in the Western USA, have been increasingly demanding accurate projections of mountain snowpack in the coming century. To address this need, this paper has leveraged the highest quality publicly available snowpack projections (e.g., BCSD-CMIP5, CMIP5, and NARCCAP) to understand historical and projected 21st-century western USA mountain snowpack, augmented by cutting-edge climate simulations of the coming century with the variable-resolution CESM model at 28km (0.25°). The conclusions from this analysis are as follows.

First, the multi-model analysis of winter season SWE for the entire western USA mountain region

showed that by 2040-2065 average SWE could decrease between -19% (NARCCAP) to -38% (VR-CESM). More resiliency in snowpack to climate change was seen in the interior mountain ranges (e.g., Rockies and Wasatch and Uinta) compared to the coastal ranges (e.g., Cascades, Klamath, and Sierra Nevada) across all of the regionally downscaled datasets. This resiliency to the climate change signal is likely due to higher average elevation in the Rockies and Wasatch and Uinta mountain ranges, a larger distance to relatively warm ocean waters (which stabilizes surface temperatures), and less dependence on equatorial derived winter storm systems (particularly atmospheric rivers) compared to the coastal mountain ranges. Last, all of the regional downscaling models exhibited a diminished interquartile ranges and maximum values, meaning that the snow distributions will diminish and snow deposition magnitudes will also decrease. This implies that seasonal snow deposition will become more predictable (as the variation collapses around the median), but total snow deposition will diminish overall. Regardless of the winter season variability differences, the collective median SWE value from all three datasets dropped by 27% throughout the western USA mountain ranges by 2065. The CMIP5 CESM global model ensemble, with no regional downscaling strategy, had negligible snowpack totals and was unusable for this analysis.

Second, the VR-CESM28 1980-2005 results were compared to several of the most high-quality and high-resolution spatially continuous datasets within the mountain research community. Compared to PRISM, peak accumulated precipitation within the total western USA mountain region was found to be positively biased in VR-CESM28 by +7% (818 mm for PRISM and 872 mm for VR-CESM28) and 2mST is minimally biased in transitory seasons (i.e., Northern Hemisphere spring (MAM) and fall (SON)) and maximized in summer (JJA) and parts of the winter (DJF). By 2025-2050, the VR-CESM28 RCP8.5 climate change signal is within the range of bias for PRISM for PRECT and 2mST, whereas by 2075-2100 the observed signal was outside this range. No quantitative conclusions were made about SWE bias in our simulations due to the lack of coherence in available datasets. The wide model spread is likely attributed to the use of land-surface models to abate spatial discontinuities in in-situ observations, the sparsity of in-situ observations in sampling the range of elevations and latitude/longitudes within a given mountain range, and, specifically to regional climate models, a lack of resolution of both topography and vegetative cover. In Rhoades et al (2016), VR-CESM28 showed the tendency to have a early peak accumulation bias associated

with too fast of a melt rate and too early total melt in a sub-region of the California Sierra Nevada when compared to SNOTEL in-situ observations. With that said, the VR-CESM28 SWE results fell in the middle of the available high-resolution SWE climate datasets analyzed, although deviations in the overall snowpack lifecycle (i.e., accumulation, peak timing and melt-rates) were observed. Therefore, the biased timing of peak snow accumulation and complete snow melt may partially explain the lack of agreement between simulated and observed hydroclimate variables. The simulated bias may be directly modulating 2mST which in turn impacts the snow-albedo feedback.

Third, VR-CESM28 results were further analyzed over the 2025-2100 time period across several hydroclimate variables including snowfall, snow cover, SWE, 2mST, and total precipitation. This was done to ensure a comprehensive assessment of the winter season western USA mountain hydro-logic changes associated with RCP8.5 within a global-to-regional modeling framework. According to the Wilcoxon-Mann-Whitney Rank-Sum Test, significant ($p<0.05$) change from the 1980-2005 PDFs for each of the hydroclimate variables varied by mountain range when assessing the 2025-2050 results, but were unanimous in the 2075-2100 results. Overall, VR-CESM28 projects a two-thirds reduction (-69%) in average mountain SWE with associated decrease in snow cover by nearly-half (-44%), an associated earlier peak snow accumulation and complete melt a month earlier (May), an uptick in mountainous total precipitation (+20%), with more rain and less snow (-24% drop in snow-to-rain ratio) and, lastly, and an amplified minimum (+5.8 °C), average (+5.0 °C), and max-imum (+4.9 °C) mountain 2mST. Notably, by the 2050s anomalously high winter season snowfall, snow cover, and SWE become almost non-existent with anomalously high 2mST (+3 °C to +6 °C) becoming the new normal. The nonlinear jump in 2mST found in the VR-CESM28 projection simulations are likely indicative of a shift in the variability of the freezing line and a modification of the local snow cover. This variability is explained, in part, by the increase in magnitude of the interquartile ranges (i.e., the variability between colder and warmer seasons) and the diminished minimum anomalies (i.e., historically cold years). The increased variability of the freezing line and modification of snow cover creates a positive feedback loop by which the regional albedo is diminished and leads to more radiation being absorbed at the surface, positively amplifying the 2mST.

Fourth, VR-CESM28 hydroclimate variables were further analyzed for elevational dependency within western USA mountain ranges. A notable nonlinear change in temperatures among the highest mountainous regions (i.e., the Rocky Mountains and the southern portion of the Sierra Nevada) was evident and supports the hypothesized phenomena known as elevation-dependent warming. For example, average (maximum) winter season 2mST anomalies were +0.97 °C (+2.35 °C) from 500m to 1000m and +2.85 °C (+7.01 °C) to +3.81 °C (+9.43 °C) from 1000m to >3000m, with a maximized elevational warming between 2000-3000m. In addition, the snowfall maxima didn't always co-locate with the maxima snow cover elevation. This is likely a result of the variability of 2mST around the freezing-line where peak snowfall is deposited in a region of high variability where at-or-below freezing 2mST weren't maintained and snow cover becomes more ephemeral. Snowfall at higher elevations (2000m to >2500m) was nominally positive or negative; however, nonlinear negative change in snowfall was found as you progress downslope. Over 500m intervals, snowfall dropped by -10.7% from 2000m to 1500m, -16.6% from 1500m to 1000m, and -20.9% from 1000m to 500m. Interestingly, when compared to snowfall, both SWE and snow cover more linearly decreased downslope. Winter season average snow cover trends indicated a -5.7%/500m to -6.8%/500m, save for the change from 1000m to 500m of -18.9%/500m, and SWE trends showed a -11%/500m to -15%/500m. The average freezing line elevation in the western USA mountainous region shifted upwards from 750m to 1500m from 1980-2005 to 2075-2100. The 750m upslope migration of the 1980-2005 freezing line wasn't uniform throughout each mountain range. Interior mountain ranges (e.g., Rockies and Wasatch and Uinta) maintain their freezing line at lower elevations compared to coastal ranges (e.g., Cascades, Klamath and Sierra Nevada). For example, the 1980-2005 average freezing line in the Cascades moved from 750m to 1750m, the Rockies from 500m to 1000m, and the Sierra Nevada from 1500m to 2250m by 2075-2100. Overall, this implies that cities that fall within 750m to 1500m (2450 ft to 4920 ft), such as those in the foothills of the western USA mountains (e.g., Reno, NV, Salt Lake City, UT, Idaho Falls, ID, and Yosemite Valley, CA), will experience less maintained snow accumulation than historically observed.

To continue the assessment of VR-CESM and its applicability to real world problems further research is needed. VR-CESM28 was only run at one resolution (28km) with one topographic representation with the maximum elevation for these simulations at 3274m across the western USA

mountain region, or 1150m below the highest peak in the western USA (Mt. Whitney). This singular topography choice was largely due to computational restraints as the focus was placed on running longer simulation time-frames. Therefore, the effects of orographic resolution and its associated forcing sensitivity will be assessed in future research. As shown in this study, VR-CESM28 may be too sensitive to orographic uplift as snowfall precipitates out too quickly at lower elevations and is not disbursed over larger bands of elevation, save for the Sierra Nevada. Thus, work is needed to understand how the variation in topographic resolution in VR-CESM impacts the hydroclimate trends in mountainous regions and the associated sensitivity to orographic uplift, rainfall transport and deposition. Coupled to this, a bias in the lifecycle of simulated SWE was found, but a complete analysis of the origin and development of this bias was out of the scope of this paper. As such, a targeted resolution increase in VR-CESM will be utilized over a selected mountain range to understand how CAM and CLM perform at a myriad of resolutions and where simulated bias begins to originate (or diminish).

Overall, VR-CESM28 results highlight a stronger climate change signal than other conventionally used datasets and, if the projections hold, will result in large ramifications for hydrologic managers of the western USA in the near-future. These changes will undoubtedly pressure western USA states to preemptively invest in climate adaptation measures such as alternative water storage, water-use efficiency, and reassess reservoir storage operations to ensure that a proper balance of allocations between the human-energy-environment nexus are maintained. Some of these climate adaptation strategies have already started in states such as California with the onset of its recent 2011-to-present unprecedented drought. With strong backing of policy and management, coupled with insights from the research community, California has taken pro-active steps to work towards better water management strategies. These strategies include more informed and targeted agricultural water allocations, mandatory reductions in urban water use, more stringent groundwater management and monitoring, and, finally, the reassessment of dated water right law from the 18th to 19th century Spanish settlement era which lead to large guaranteed appropriations of surface and groundwater to present day land owners and large cities (Hanak et al, 2011). More water management initiatives like this will be needed to ensure proper resiliency to unprecedented hydroclimate changes due to anthropogenic climate change.

68

Tables

Table 6: Western USA climate datasets.

Climate Dataset	Snowpack Variable	Spatial Resolution	Temporal Resolution	Assessed Timeframes
VR-CESM28	SNOWFALL, SNOWC, SWE, 2mST	28km	Daily	1980-2005, 2025-2100
NLDAS	SWE	14km	Daily	1980-2005
PRISM	PRECT, 2mST	4km	Daily	1980-2005
BCSD-CMIP5	SWE	14 km	Monthly	1975-2000, 2040-2065
NARCCAP	SWE	55 km	Hourly	1975-2000, 2040-2065
CMIP5	SWE	111 km	Monthly	1980-2005, 2040-2065

Table 7: Summary statistics for the winter season (DJF) average snow water equivalent (SWE) within the western USA mountain ranges. Note that BCSD-CMIP5 was capped at 1500 mm due to anomalously high SWE values in select grid points (e.g., Cascades). The ensemble value is the average of the three-regionally downscaled datasets (i.e., VR-CESM28, BCSD-CMIP5, and NARCCAP).

	Climate Dataset	Mean (mm)	Standard Deviation (mm)	Min (mm)	Lower Quartile (mm)	Median (mm)	Upper Quartile (mm)	Interquartile Range (mm)	Max (mm)	Range (mm)
Western USA Mountains										
Pre-2005	VR-CESM28	90.0	5.47	49.7	61.3	83.2	93.8	32.5	163	113
	BCSD-CMIP5	94.7	5.93	22.6	67.0	96.2	114	46.9	197	174
	NARCCAP	106	5.28	60.8	83.3	103	118	35.0	164	103
	CMIP5	2.21	0.70	1.51	1.86	2.19	2.34	0.48	3.69	2.18
	Ensemble	96.8	5.57	44.4	70.5	94.1	109	38.1	174	130
2040-2065	VR-CESM28	56.3	5.07	19.4	39.9	57.5	68.4	28.5	130	111
	BCSD-CMIP5	70.2	4.75	31.8	53.0	68.9	77.7	24.8	113	81.7
	NARCCAP	85.7	5.29	40.1	66.4	81.0	89.9	23.5	155	115
	CMIP5	0.69	0.49	0.36	0.48	0.65	0.74	0.26	1.20	0.83
	Ensemble	70.7	5.04	30.4	53.1	69.1	78.7	25.6	133	102
Cascades										
Pre-2005	VR-CESM28	64.8	7.32	12.1	32.6	47.3	63.8	31.2	220	208
	BCSD-CMIP5	123	7.34	18.1	81.6	117	158	76.1	247	229
	NARCCAP	111	7.06	32.2	73.5	112	137	63.7	201	169
	CMIP5	0.88	0.78	0.18	0.36	0.77	0.98	0.62	2.72	2.55
	Ensemble	99.6	7.24	20.8	62.6	92.0	120	57.0	223	202
2040-2065	VR-CESM28	23.7	5.42	0.45	6.83	16.1	27.3	20.5	146	146
	BCSD-CMIP5	78.1	5.86	23.6	53.2	73.1	94.9	41.7	160	137
	NARCCAP	47.1	5.97	9.47	20.9	36.1	57.8	37.0	162	153
	CMIP5	0.08	0.30	0.01	0.03	0.06	0.09	0.06	0.42	0.41
	Ensemble	49.6	5.75	11.2	27.0	41.8	60.0	33.0	156	145
Klamath										
Pre-2005	VR-CESM28	13.8	3.84	1.33	3.05	7.87	18.1	15.1	63.3	61.9
	BCSD-CMIP5	61.7	6.13	10.7	34.1	59.5	78.0	43.9	151	140
	NARCCAP	50.9	5.16	8.79	24.9	54.8	58.7	33.7	121	112
	CMIP5	0.24	0.46	0.02	0.09	0.14	0.28	0.19	0.80	0.77
	Ensemble	42.2	5.13	6.94	20.7	40.7	51.6	30.9	112	105
2040-2065	VR-CESM28	3.58	2.20	0.09	0.64	2.28	3.71	3.07	23.6	23.5
	BCSD-CMIP5	47.9	5.53	9.37	18.2	38.8	65.2	47.0	113	104
	NARCCAP	13.5	3.67	1.26	3.66	8.66	14.7	11.0	51.4	50.1
	CMIP5	0.01	0.12	0.00	0.01	0.01	0.01	0.01	0.06	0.06
	Ensemble	21.7	4.04	3.57	7.50	16.5	27.9	20.4	62.7	59.1
Rockies										
Pre-2005	VR-CESM28	102	5.65	56.2	74.1	94.5	125	51.1	159	103
	BCSD-CMIP5	91.3	5.71	26.7	71.1	93.0	103	31.7	197	171
	NARCCAP	114	5.29	64.9	92.3	112	127	34.5	183	118
	CMIP5	2.71	0.81	1.80	2.29	2.56	2.83	0.54	4.76	2.96
	Ensemble	102.2	5.55	49.3	79.2	99.7	118	39.1	180	131
2040-2065	VR-CESM28	68.2	5.37	21.5	50.8	74.3	79.8	29.0	140	119
	BCSD-CMIP5	71.1	4.60	31.4	58.1	68.5	81.7	23.5	115	83.8
	NARCCAP	105	5.49	52.3	87.5	104	114	26.0	180	127
	CMIP5	0.88	0.55	0.46	0.62	0.83	0.94	0.31	1.45	0.99
	Ensemble	81.5	5.17	35.1	65.5	82.4	91.7	26.2	145	110
Sierra Nevada										
Pre-2005	VR-CESM28	79.4	6.98	2.70	32.8	86.9	106	72.7	203	200
	BCSD-CMIP5	119	8.92	11.5	45.7	110	158	112	264	252
	NARCCAP	63.8	5.92	13.3	32.0	54.3	81.8	49.8	128	115
	CMIP5	0.48	0.62	0.04	0.22	0.34	0.58	0.36	1.64	1.60
	Ensemble	87.4	7.38	9.17	36.8	83.8	115	78.1	198	189
2040-2065	VR-CESM28	38.6	6.22	2.61	10.7	25.3	33.5	22.8	160	157
	BCSD-CMIP5	83.4	6.47	17.8	41.9	81.4	108	66.5	176	158
	NARCCAP	25.2	4.74	3.75	5.81	19.2	26.2	20.4	89.7	86.0
	CMIP5	0.03	0.19	0.00	0.01	0.02	0.04	0.03	0.17	0.17
	Ensemble	49.1	5.86	8.07	19.5	42.0	56.0	36.5	142	134
Wasatch and Uinta										
Pre-2005	VR-CESM28	90.6	5.77	25.7	64.9	89.4	99.2	34.3	175	149
	BCSD-CMIP5	74.6	6.51	4.84	41.3	64.2	101	59.4	181	176
	NARCCAP	88.8	5.65	38.2	64.6	88.4	106	41.2	156	117
	CMIP5	1.12	0.66	0.43	0.86	1.09	1.15	0.28	2.45	2.02
	Ensemble	84.7	5.99	22.9	56.9	80.6	102	45.0	171	148
2040-2065	VR-CESM28	56.3	5.52	13.5	27.9	56.3	65.5	37.6	115	102
	BCSD-CMIP5	44.4	4.45	12.0	28.0	41.9	56.3	28.3	82.9	70.9
	NARCCAP	69.8	5.73	21.1	40.9	64.4	87.9	46.9	157	136
	CMIP5	0.24	0.33	0.08	0.15	0.20	0.30	0.15	0.48	0.40
	Ensemble	56.8	5.26	15.5	32.3	54.2	69.9	37.6	118	103

Table 8: Pre-2005 vs 2040-2065 percent change for the winter season (DJF) average snow water equivalent (SWE) within the western USA mountain ranges. The ensemble value is the average of the three-regionally downscaled datasets (i.e., VR-CESM28, BCSD-CMIP5, and NARCCAP).

	Climate Dataset	Mean (% Change)	Standard Deviation (% Change)	Min (% Change)	Lower Quartile (% Change)	Median (% Change)	Upper Quartile (% Change)	Interquartile Range (% Change)	Max (% Change)	Range (mm)
Western USA Mountains										
Pre-2005 vs 2040-2065	VR-CESM28	-37.5	-7.25	-60.9	-34.9	-30.9	-27.1	-12.3	-20.1	-2.20
	BCSD-CMIP5	-25.9	-19.9	40.6	-20.9	-28.4	-31.7	-47.2	-42.3	-53.0
	NARCCAP	-18.9	0.28	-34.0	-20.4	-21.2	-24.0	-32.8	-5.54	11.3
	CMIP5	-68.6	-29.7	-75.9	-74.1	-70.3	-68.2	-45.0	-67.5	-61.7
	Ensemble	-26.9	-9.38	-31.4	-24.7	-26.5	-27.6	-32.9	-23.9	-21.3
Cascades										
Pre-2005 vs 2040-2065	VR-CESM28	-63.4	-26.0	-96.3	-79.0	-66.0	-57.3	-34.5	-33.4	-29.8
	BCSD-CMIP5	-36.3	-20.1	30.5	-34.8	-37.3	-39.8	-45.2	-35.2	-40.4
	NARCCAP	-57.7	-15.4	-70.6	-71.6	-67.7	-57.9	-42.0	-19.4	-9.60
	CMIP5	-90.6	-62.0	-94.5	-91.4	-91.7	-90.7	-90.3	-84.7	-84.0
	Ensemble	-50.2	-20.5	-46.3	-56.9	-54.6	-49.8	-42.1	-29.9	-28.2
Klamath										
Pre-2005 vs 2040-2065	VR-CESM28	-74.1	-42.8	-93.3	-79.1	-71.0	-79.6	-79.6	-62.6	-62.0
	BCSD-CMIP5	-22.3	-9.82	-12.3	-46.5	-34.8	-16.4	7.02	-24.9	-25.9
	NARCCAP	-73.5	-28.8	-85.6	-85.3	-84.4	-75.0	-67.3	-57.5	-55.3
	CMIP5	-94.9	-74.7	-98.2	-98.2	-95.2	-94.7	-93.1	-92.8	-92.6
	Ensemble	-48.6	-21.3	-48.5	-63.7	-59.4	-46.0	-34.1	-43.8	-43.5
Rockies										
Pre-2005 vs 2040-2065	VR-CESM28	-33.0	-4.94	-61.8	-31.4	-21.4	-36.3	-43.3	-12.0	15.2
	BCSD-CMIP5	-22.1	-19.4	17.7	-18.3	-26.3	-20.5	-25.7	-41.6	-50.9
	NARCCAP	-7.50	3.81	-19.5	-5.12	-6.63	-10.4	-24.5	-1.91	7.72
	CMIP5	-67.5	-32.2	-74.2	-72.8	-67.4	-66.9	-42.0	-69.5	-66.7
	Ensemble	-20.3	-6.93	-28.9	-17.3	-17.4	-22.5	-33.0	-19.4	-15.9
Sierra Nevada										
Pre-2005 vs 2040-2065	VR-CESM28	-51.4	-10.8	-3.53	-67.3	-70.9	-68.2	-68.7	-21.5	-21.7
	BCSD-CMIP5	-30.1	-27.5	55.6	-8.20	-26.0	-31.2	-40.6	-33.3	-37.4
	NARCCAP	-60.4	-20.0	-71.9	-81.8	-64.6	-68.0	-59.1	-30.0	-25.1
	CMIP5	-93.1	-69.7	-98.9	-96.2	-93.1	-93.2	-91.4	-89.8	-89.6
	Ensemble	-43.9	-20.6	-12.1	-47.1	-49.9	-51.3	-53.2	-28.6	-29.4
Wasatch and Uinta										
Pre-2005 vs 2040-2065	VR-CESM28	-37.8	-4.29	-47.6	-57.0	-37.0	-34.0	9.54	-34.1	-31.8
	BCSD-CMIP5	-40.6	-31.7	148.0	-32.1	-34.8	-44.0	-52.3	-54.3	-59.8
	NARCCAP	-21.3	1.44	-44.9	-36.6	-27.1	-16.9	13.9	0.76	15.6
	CMIP5	-78.6	-49.7	-81.3	-82.5	-81.3	-74.1	-48.5	-80.4	-80.2
	Ensemble	-32.9	-12.1	-32.4	-43.3	-32.8	-31.4	-16.4	-30.6	-30.4

Table 9: Winter season (DJF) average anomalies within western USA mountain ranges for RCP8.5 2025-2050 and 2075-2100 VR-CESM28 simulations. The Wilcoxon Rank-Sum Test p-values are also given with a true (false) indication if the p-value is below (above) the 0.05 significance level.

Winter Season Anomalies		Wilcoxon Rank-Sum Test p-value (p = 0.05)	Mean	Standard Deviation	Min	Lower Quartile	Median	Upper Quartile	Interquartile Range	Max
Western USA Mountains										
Snowfall	2025-2050	0.577 (False)	-4.39	9.53	-18.9	-14.6	1.44	-1.88	12.7	21.8
(% Change)	2075-2100	1.69×10^{-4} (True)	-29.8	1.22	-43.5	-39.1	-35.0	-13.9	25.2	-24.4
Snow Cover	2025-2050	0.0371 (True)	-10.2	29.0	-39.4	-11.7	-9.44	-4.47	7.23	-0.28
(% Change)	2075-2100	3.16×10^{-14} (True)	-44.2	22.7	-68.3	-68.3	-42.9	-35.6	17.0	-31.8
Snow Water Equivalent	2025-2050	3.97×10^{-3} (True)	-24.9	1.81	-58.5	-29.2	-19.7	-20.1	9.15	3.63
(% Change)	2075-2100	4.30×10^{-12} (True)	-68.9	-23.4	-88.3	-79.0	-70.8	-57.7	21.3	-55.7
Surface Temperature	2025-2050	0.0320 (True)	1.31	0.21	0.76	0.61	0.75	1.67	1.05	2.34
(Anomaly (°C))	2075-2100	1.90×10^{-13} (True)	5.03	0.01	5.83	4.85	4.65	5.08	0.23	4.91
Cascades										
Snowfall	2025-2050	0.289 (False)	-10.7	8.68	-34.1	-32.1	-0.84	7.98	40.1	14.5
(% Change)	2075-2100	6.97×10^{-8} (True)	-54.9	-8.60	-87.0	-72.6	-56.3	-44.9	27.7	-40.9
Snow Cover	2025-2050	0.0247 (True)	-20.3	4.88	-55.0	-33.5	-17.1	-10.5	23.0	-5.33
(% Change)	2075-2100	3.09×10^{-12} (True)	-71.5	-18.5	-94.0	-82.4	-71.5	-68.3	14.1	-51.0
Snow Water Equivalent	2025-2050	1.86×10^{-3} (True)	-44.3	-11.8	-82.3	-68.7	-45.8	-39.9	28.8	-4.11
(% Change)	2075-2100	4.30×10^{-12} (True)	-90.1	-61.0	-99.0	-96.3	-92.6	-90.1	6.21	-83.4
Surface Temperature	2025-2050	0.108 (False)	0.91	0.04	1.25	0.64	0.76	0.41	-0.23	1.23
(Anomaly (°C))	2075-2100	1.06×10^{-12} (True)	4.17	-0.12	4.96	4.09	4.02	3.89	-0.19	3.38
Klamath										
Snowfall	2025-2050	0.271 (False)	-18.3	-5.91	-31.7	0.26	-19.0	-13.9	-14.2	4.64
(% Change)	2075-2100	4.29×10^{-11} (True)	-78.3	-42.2	-95.0	-87.6	-78.6	-77.0	10.6	-72.6
Snow Cover	2025-2050	0.0494 (True)	-32.7	-20.2	-62.5	-20.9	-19.3	-34.9	-14.0	-21.4
(% Change)	2075-2100	1.54×10^{-12} (True)	-87.9	-57.6	-99.5	-94.2	-87.6	-87.7	6.43	-84.3
Snow Water Equivalent	2025-2050	0.0741 (False)	-43.1	-7.31	-79.6	-30.2	-47.8	-49.4	-19.2	2.49
(% Change)	2075-2100	1.54×10^{-13} (True)	-96.1	-78.8	-99.9	-97.6	-96.1	-97.0	0.61	-96.3
Surface Temperature	2025-2050	0.0679 (False)	0.82	0.02	1.56	1.23	0.23	0.60	-0.63	1.22
(Anomaly (°C))	2075-2100	1.90×10^{-13} (True)	3.69	-0.06	4.48	3.84	3.47	3.59	-0.25	3.21
Rockies										
Snowfall	2025-2050	0.672 (False)	-2.29	4.56	-3.59	-6.04	1.41	1.60	7.65	8.28
(% Change)	2075-2100	9.01×10^{-3} (True)	-16.4	6.03	-23.9	-23.3	-19.9	-6.87	16.5	-9.22
Snow Cover	2025-2050	0.0621 (False)	-7.72	42.9	-42.5	-9.66	-8.25	-3.64	6.02	0.34
(% Change)	2075-2100	1.58×10^{-14} (True)	-38.1	47.2	-67.4	-48.8	-38.1	-27.6	21.2	-27.5
Snow Water Equivalent	2025-2050	0.0108 (True)	-22.8	-3.78	-61.8	-26.2	-17.5	-30.8	-4.59	-5.29
(% Change)	2075-2100	4.29×10^{-11} (True)	-64.9	-18.0	-85.7	-77.1	-65.3	-58.6	18.6	-42.6
Surface Temperature	2025-2050	0.0371 (True)	1.41	0.26	0.95	0.75	0.60	1.99	1.24	2.36
(Anomaly (°C))	2075-2100	1.90×10^{-13} (True)	5.32	0.05	6.41	4.75	4.91	5.82	1.07	5.46
Sierra Nevada										
Snowfall	2025-2050	0.603 (False)	-2.64	11.7	-65.7	14.1	-15.5	-5.69	-19.8	70.0
(% Change)	2075-2100	1.83×10^{-5} (True)	-54.8	-20.1	-68.0	-62.1	-59.6	-51.0	11.1	-34.0
Snow Cover	2025-2050	0.0494 (True)	-18.9	1.53	-71.9	-23.0	-25.7	-19.0	4.02	8.18
(% Change)	2075-2100	4.03×10^{-9} (True)	-66.8	-17.5	-89.5	-78.1	-69.6	-63.8	14.3	-43.1
Snow Water Equivalent	2025-2050	0.0994 (False)	-18.7	24.9	-83.5	-34.1	-52.6	-44.3	-10.2	73.1
(% Change)	2075-2100	1.70×10^{-7} (True)	-83.3	-33.8	-94.6	-96.1	-94.2	-86.6	9.46	-53.8
Surface Temperature	2025-2050	0.0353 (True)	1.06	0.10	1.46	0.92	0.73	0.75	-0.17	3.18
(Anomaly (°C))	2075-2100	4.75×10^{-13} (True)	4.18	0.00	4.72	3.91	3.95	4.39	0.48	4.21
Wasatch and Uinta										
Snowfall	2025-2050	0.893 (False)	1.23	10.7	-61.2	-5.07	-1.07	0.95	6.02	27.3
(% Change)	2075-2100	5.50×10^{-3} (True)	-22.8	4.12	-24.5	-29.5	-30.5	-33.7	-4.21	6.50
Snow Cover	2025-2050	0.0472 (True)	-13.1	14.6	-64.4	-18.6	-14.1	-17.9	0.73	4.28
(% Change)	2075-2100	1.04×10^{-9} (True)	-51.0	8.10	-80.8	-61.7	-54.9	-49.8	11.9	-16.7
Snow Water Equivalent	2025-2050	0.0136 (True)	-24.1	14.8	-67.5	-37.5	-35.0	-13.5	24.0	19.1
(% Change)	2075-2100	4.03×10^{-9} (True)	-70.3	-14.4	-86.8	-85.9	-80.2	-65.9	20.0	-44.8
Surface Temperature	2025-2050	7.51×10^{-3} (True)	1.83	0.20	1.30	1.45	1.09	2.04	0.59	2.70
(Anomaly (°C))	2075-2100	1.06×10^{-12} (True)	5.83	0.02	5.90	5.73	5.68	6.09	0.36	4.75

Table 10: VR-CESM28 simulated winter season (DJF) average 500m elevational anomalies within the total western USA mountain range for 1980-2005 and 2025-2100 under the RCP8.5 climate forcing.

| Average Winter Anomaly	Elevation	Min	Mean	Max	Interquartile Range	Standardized Regression Coefficient
Snowfall (% Change)						
1980-2005 **(2025-2100)**	>500m	-56.3 **(-94.5)**	0.00 **(-50.1)**	113 **(91.8)**	42.0 **(47.2)**	-0.03 **(-0.64)**
	>1000m	-36.1 **(-78.8)**	0.00 **(-29.2)**	51.5 **(90.7)**	23.0 **(43.0)**	-0.20 **(-0.50)**
	>1500m	-32.4 **(-50.4)**	0.00 **(-12.6)**	30.3 **(61.1)**	29.7 **(36.8)**	-0.30 **(-0.36)**
	>2000m	-35.1 **(-48.4)**	0.00 **(-1.92)**	38.6 **(59.7)**	28.6 **(36.0)**	-0.25 **(-0.20)**
	>2500m	-37.4 **(-48.8)**	0.00 **(5.88)**	62.4 **(70.9)**	22.3 **(29.7)**	-0.15 **(-0.04)**
	>3000m	-39.5 **(-54.9)**	0.00 **(7.88)**	78.9 **(93.0)**	25.1 **(43.2)**	-0.05 **(0.04)**
Snow Cover (% Change)						
1980-2005 **(2025-2100)**	>500m	-73.3 **(-97.7)**	0.00 **(-58.7)**	97.4 **(43.6)**	61.7 **(53.5)**	0.10 **(-0.67)**
	>1000m	-35.9 **(-89.2)**	0.00 **(-39.8)**	37.8 **(35.8)**	27.3 **(47.0)**	-0.04 **(-0.66)**
	>1500m	-32.9 **(-82.9)**	0.00 **(-33.0)**	23.1 **(32.2)**	22.0 **(36.0)**	-0.17 **(-0.61)**
	>2000m	-24.1 **(-73.5)**	0.00 **(-26.3)**	22.2 **(23.5)**	15.3 **(33.1)**	-0.14 **(-0.61)**
	>2500m	-32.2 **(-65.8)**	0.00 **(-20.6)**	28.4 **(25.4)**	15.3 **(27.2)**	-0.20 **(-0.53)**
	>3000m	-24.0 **(-66.3)**	0.00 **(-14.3)**	11.9 **(13.5)**	12.1 **(21.3)**	-0.14 **(-0.44)**
SWE (% Change)						
1980-2005 **(2025-2100)**	>500m	-90.2 **(-99.8)**	0.00 **(-74.7)**	230 **(102)**	70.7 **(32.2)**	0.01 **(-0.50)**
	>1000m	-64.3 **(-99.1)**	0.00 **(-62.9)**	147 **(174)**	42.3 **(43.0)**	-0.06 **(-0.53)**
	>1500m	-63.9 **(-97.2)**	0.00 **(-51.0)**	88.0 **(120)**	54.2 **(41.0)**	-0.14 **(-0.54)**
	>2000m	-54.4 **(-92.3)**	0.00 **(-42.6)**	69.0 **(86.5)**	34.5 **(48.7)**	-0.04 **(-0.58)**
	>2500m	-54.2 **(-85.0)**	0.00 **(-32.1)**	141 **(99.2)**	42.2 **(52.9)**	0.01 **(-0.46)**
	>3000m	-52.2 **(-88.7)**	0.00 **(-17.5)**	123 **(220)**	51.9 **(52.9)**	0.08 **(-0.32)**
2mST (Anomaly (°C))						
1980-2005 **(2025-2100)**	>500m	-2.95 **(-0.76)**	0.00 **(0.97)**	3.05 **(2.35)**	1.69 **(1.18)**	0.02 **(0.66)**
	>1000m	-3.29 **(-2.38)**	0.00 **(2.85)**	3.11 **(7.01)**	1.65 **(3.58)**	0.04 **(0.63)**
	>1500m	-3.15 **(-2.78)**	0.00 **(3.29)**	3.23 **(8.28)**	1.87 **(3.76)**	0.13 **(0.61)**
	>2000m	-3.60 **(-2.33)**	0.00 **(3.81)**	3.71 **(9.25)**	1.39 **(4.32)**	0.21 **(0.62)**
	>2500m	-3.36 **(-1.63)**	0.00 **(3.55)**	3.70 **(8.85)**	1.48 **(3.52)**	0.28 **(0.62)**
	>3000m	-2.73 **(-1.67)**	0.00 **(3.50)**	3.74 **(9.43)**	1.33 **(3.54)**	0.29 **(0.60)**

Figures
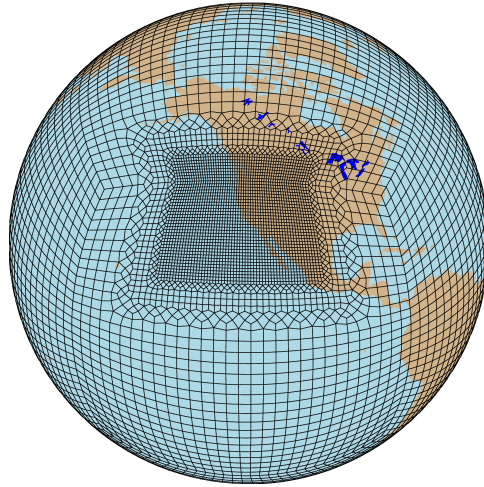
Figure 15: The VR-CESM grid used for this study utilized a quasi-uniform 111km (1°) base-resolution in a cubed-sphere grid structure. The smooth VR refinement region is depicted via the convex polygons with the highest grid resolution of 28km (0.25°) over the Eastern Pacific and the western USA.
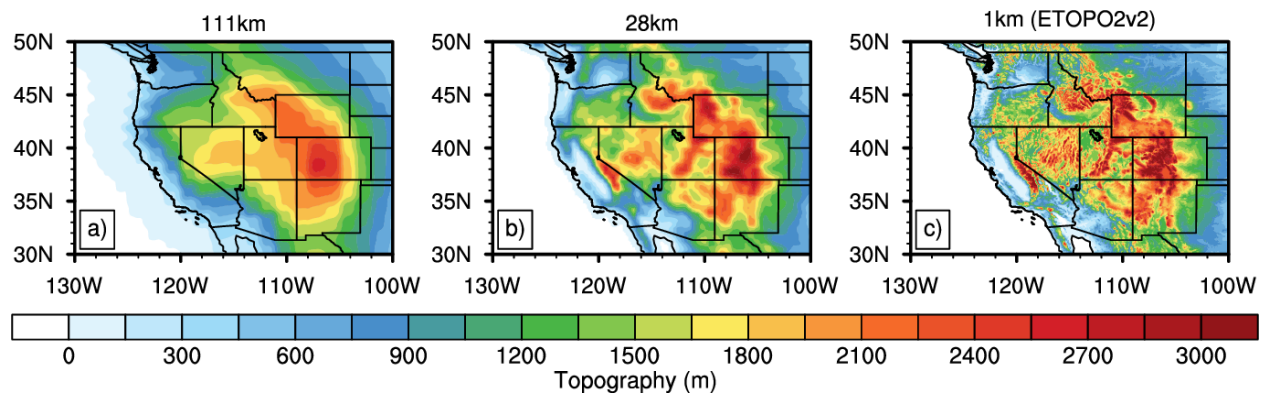

Figure 16: Comparison of topographical distributions between (a) standard uniform-resolution 111km (1°) CESM and (b) VR-CESM 28km (0.25°) to (c) the satellite derived ETOPO2v2 1km (2′) dataset.
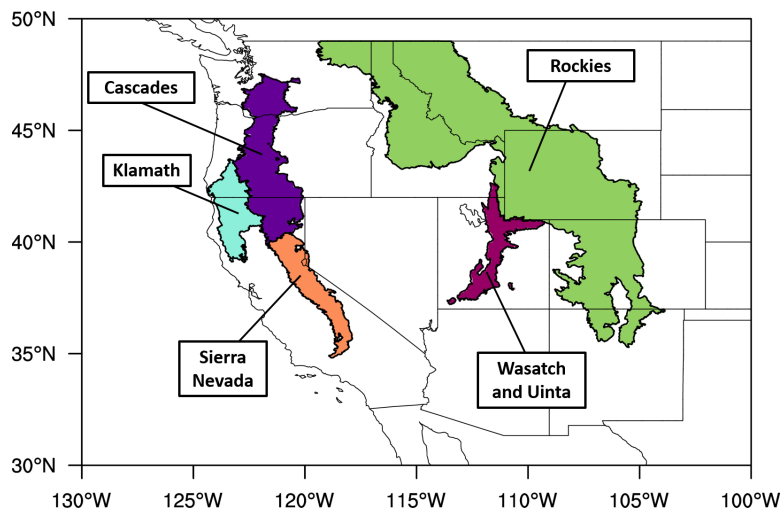
Figure 17: The five EPA Ecoregion III sub-regions used in this assessment, delineated by color and emboldened lines.
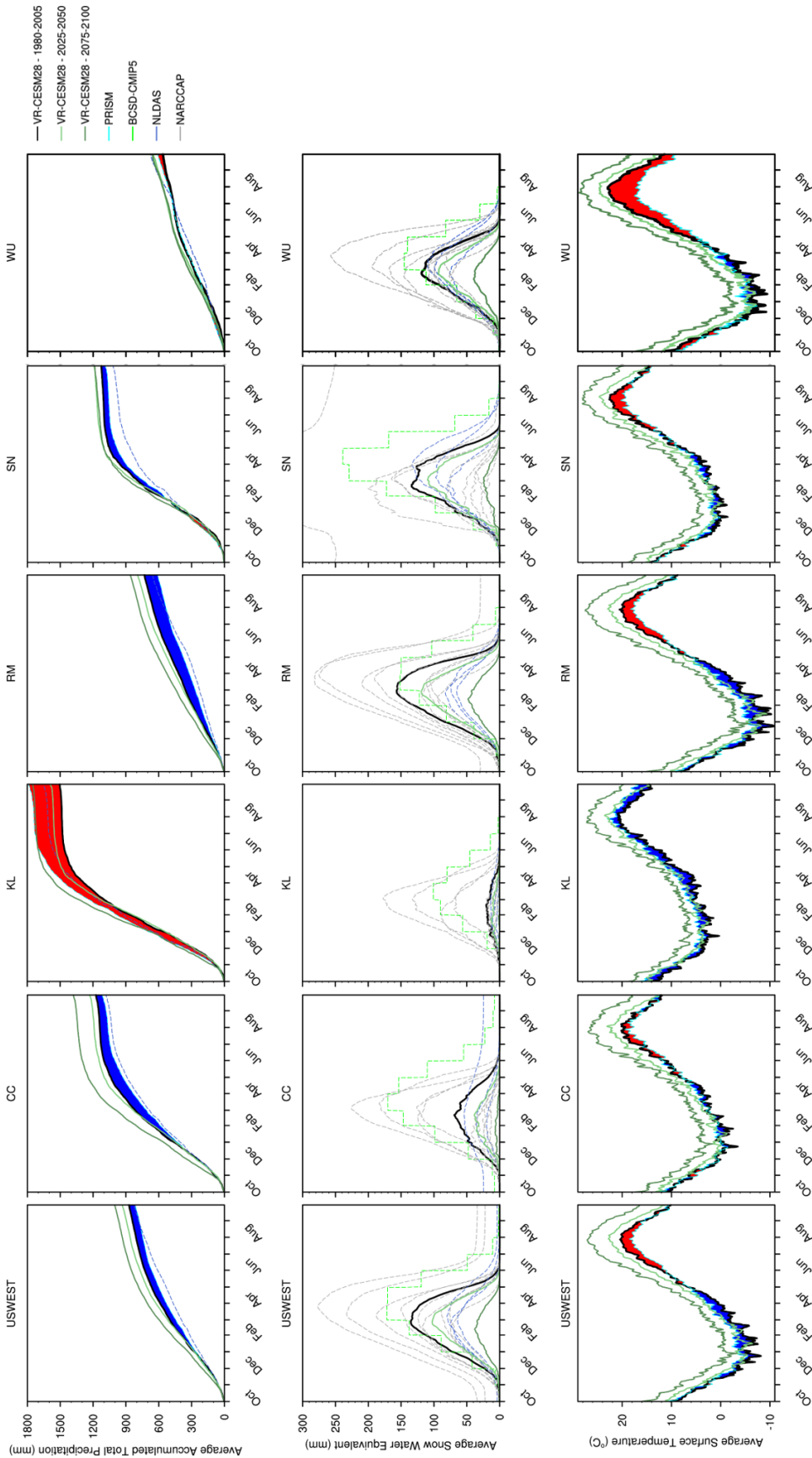
Figure 18: VR-CESM28 climate daily average (Pre-2005) values for accumulated precipitation (top), SWE (center), and two-meter surface temperature (bottom) against PRISM, BCSD-CMIP5, NLDAS, and NARCCAP within the total western USA mountain ranges (first column) and all of the individual mountain ranges. VR-CESM28 model bias is highlighted in blue (red) for over (under) accumulation in precipitation and red (blue) for positive (negative) two-meter surface temperature. VR-CESM28 climate daily averages for RCP8.5 2025-2050 and 2075-2100 results are superimposed over the 1980-2005 results in dark red.
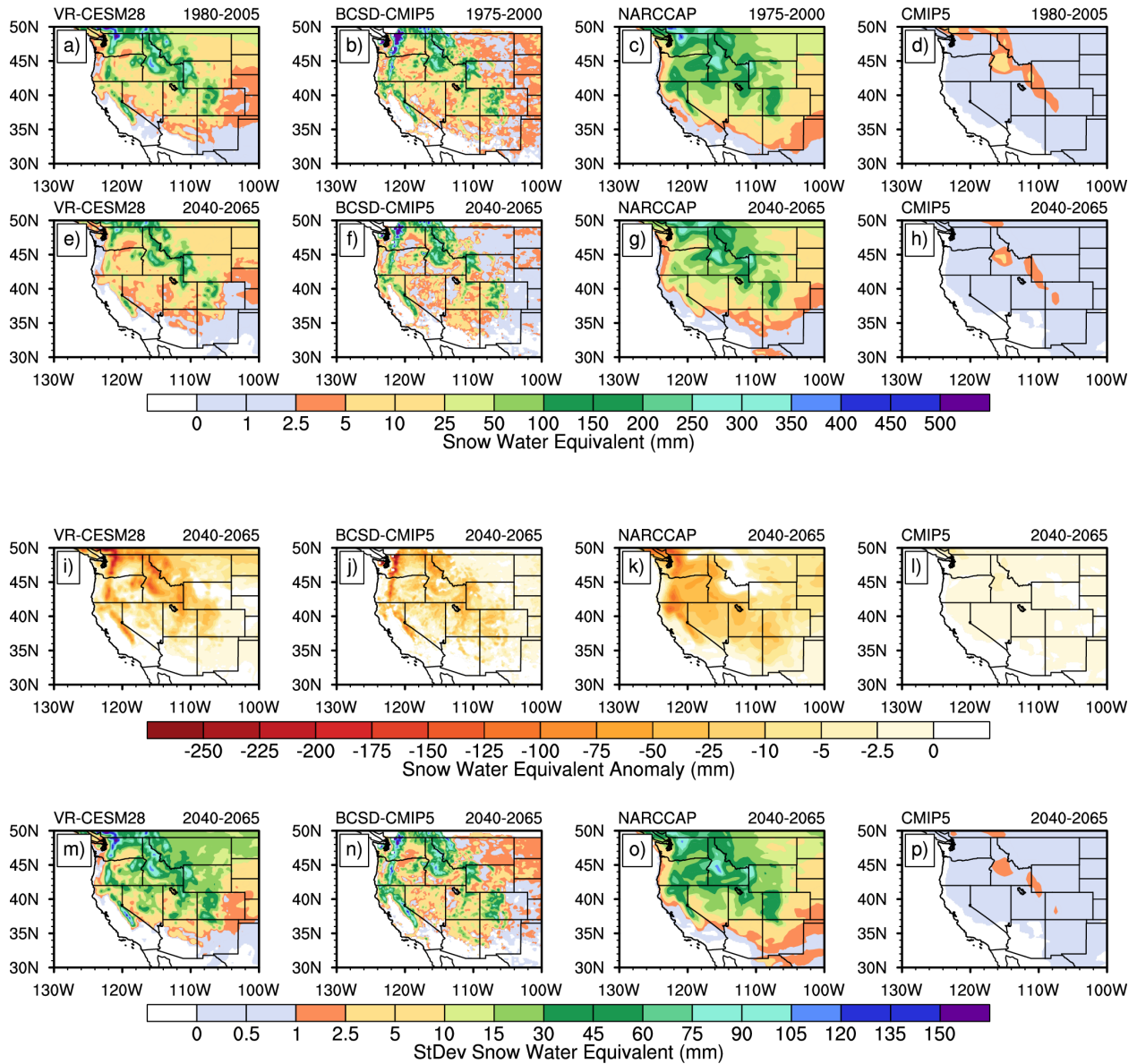
Figure 19: The climate and seasonal (DJF) distributions and percent changes of SWE across the western USA within four global-to-regional climate change datasets. SWE climate average totals within pre-2005 (a-d) and RCP8.5 2040-2065 (e-h), SWE anomalies (i-l) and 2040-2065 seasonal (DJF) variability are shown.
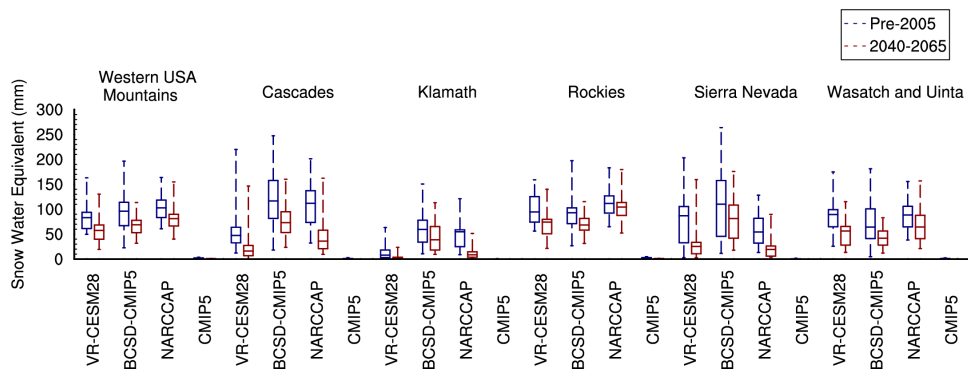
Figure 20: The winter (DJF) season average box-and-whisker distributions of SWE across each of the western USA mountain ranges and each of the simulation periods. The blue box-and-whisker represents the 25 DJF seasons of pre-2005 simulations and the red box-and-whisker represents the 25 DJF simulated seasons from 2040-2065 forced by the business-as-usual (RCP8.5) scenario.
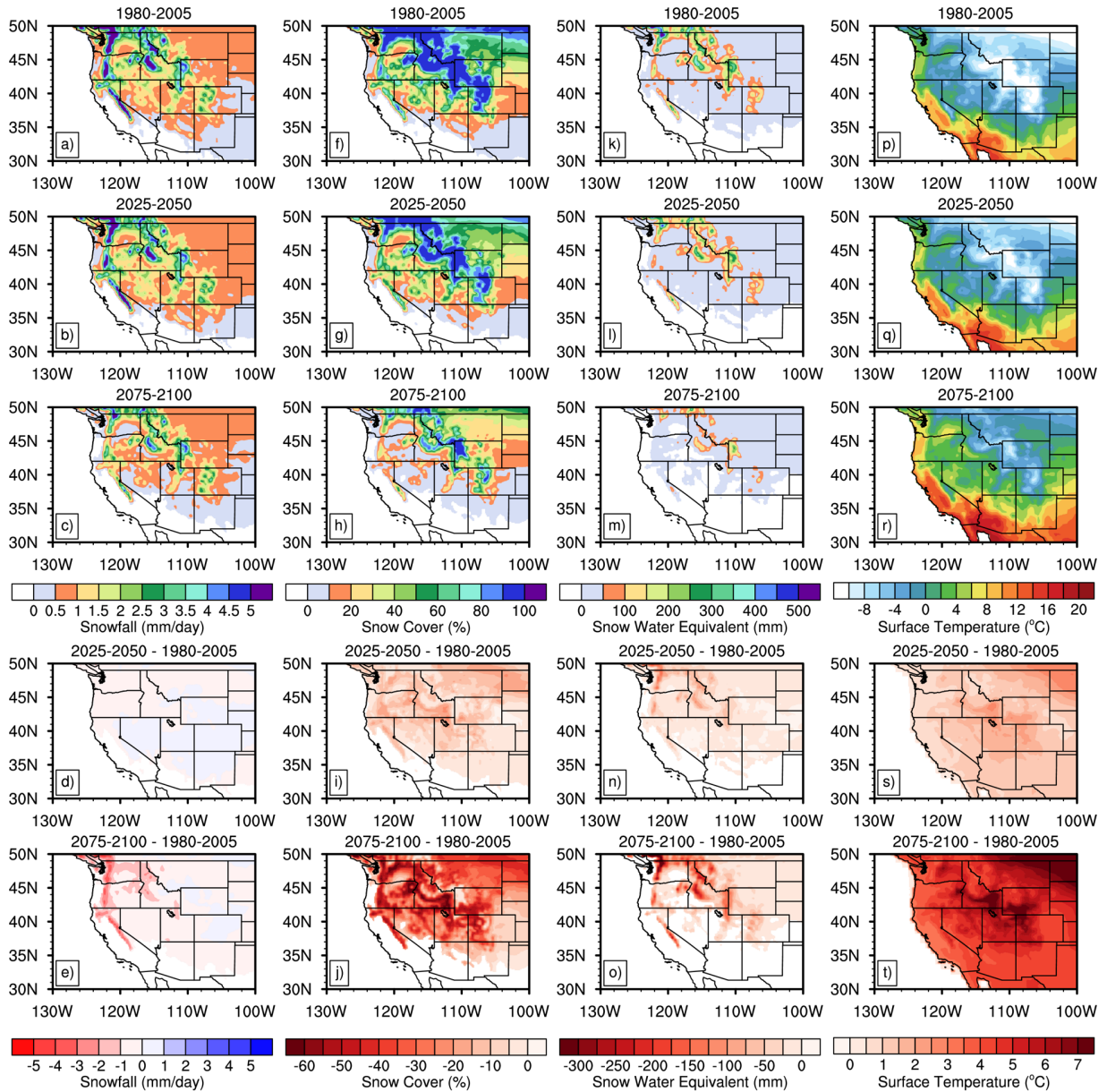
Figure 21: A panel of VR-CESM28 winter (DJF) climatological averages of snowfall (a-c), snow cover (f-h), SWE (k-m), and two-meter surface temperature (p-r) for 1980-2005, 2025-2050, and 2075-2100 under the RCP8.5 scenario over the western USA. Climatological anomalies for the RCP8.5 scenario versus 1980-2005 are highlighted in the bottom two rows.
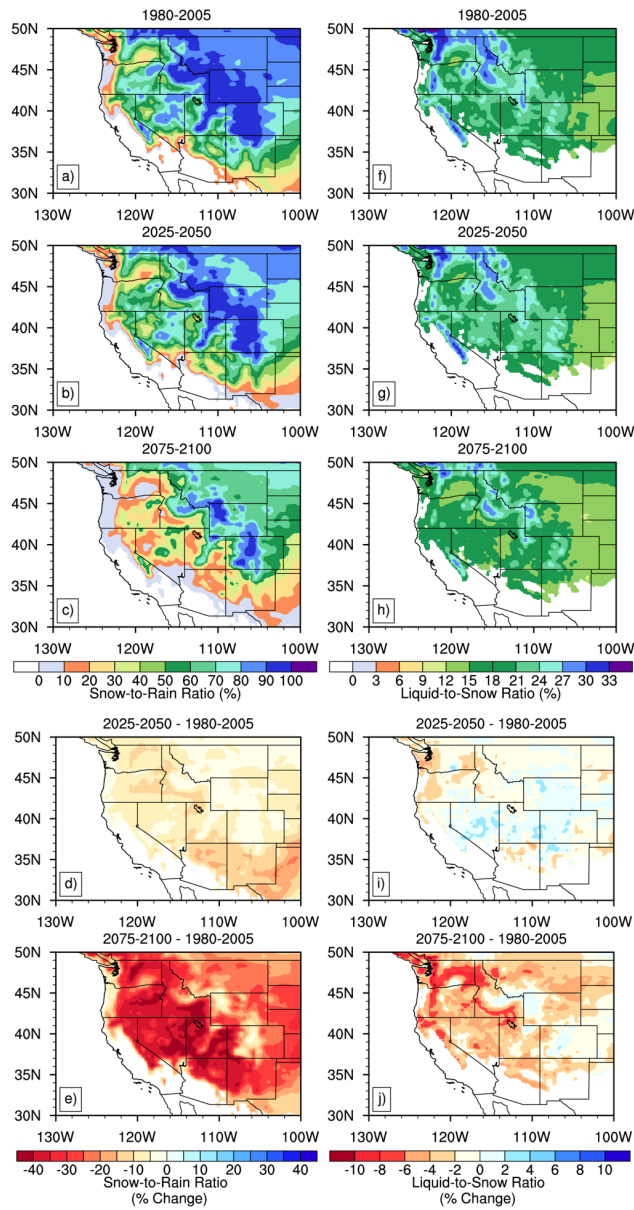
Figure 22: Similar to Figure 21, however for snowfall-to-rainfall (a-c) and liquid-to-snow (f-h) ratios, with percent changes in each ratio highlighted under the DJF climatological averages (d-e and i-j)
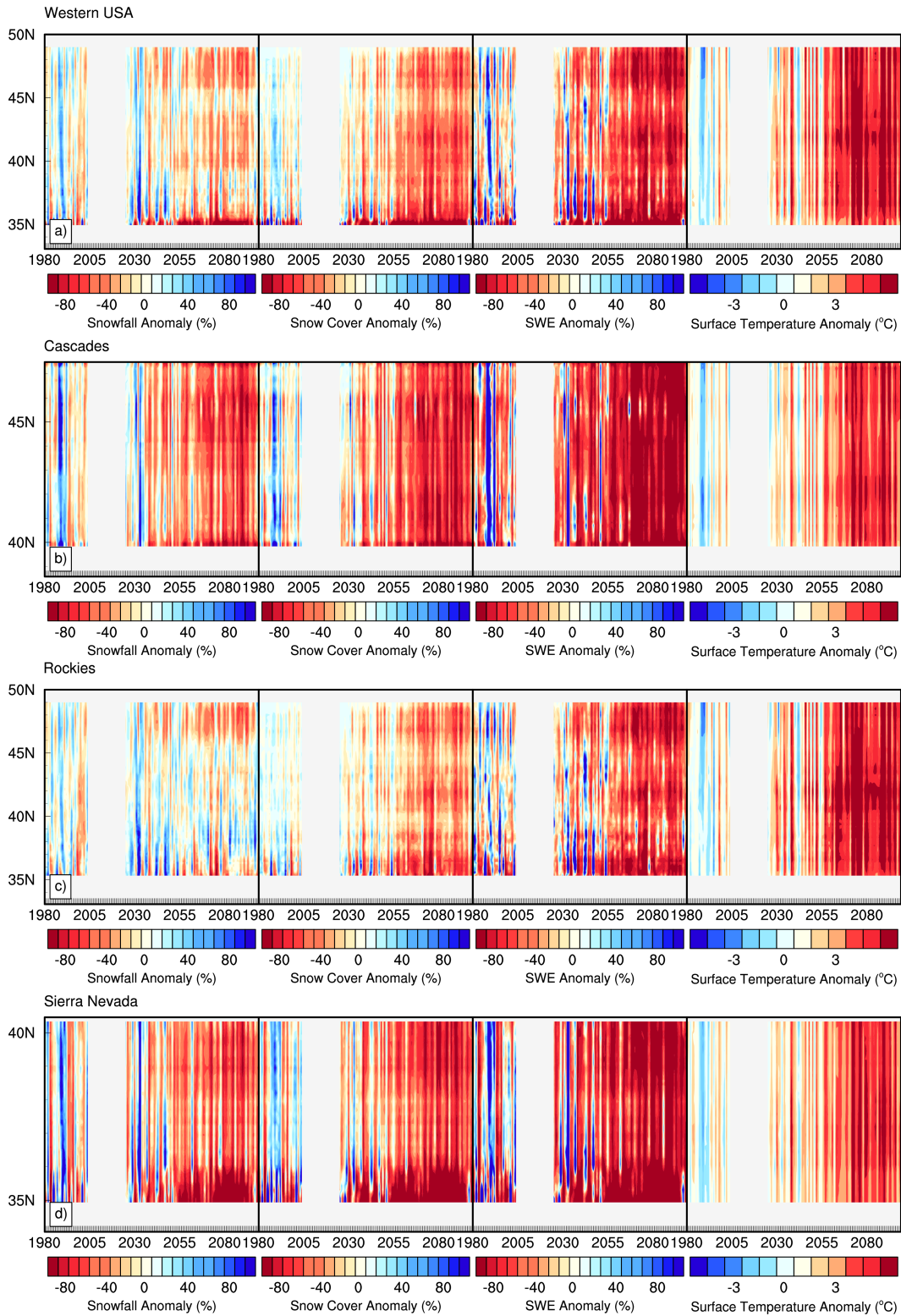
Figure 23: Hovmöller diagram of the latitudinal average DJF total western USA mountain range (a), Cascades (b), Rockies (c), and Sierra Nevada (d), snowfall, snow cover, SWE, and 2mST anomalies from the 1980-2005 DJF average. Regions of red (blue) indicate negative (positive) seasonal trends, save for two-meter surface temperature which has opposite color indication.
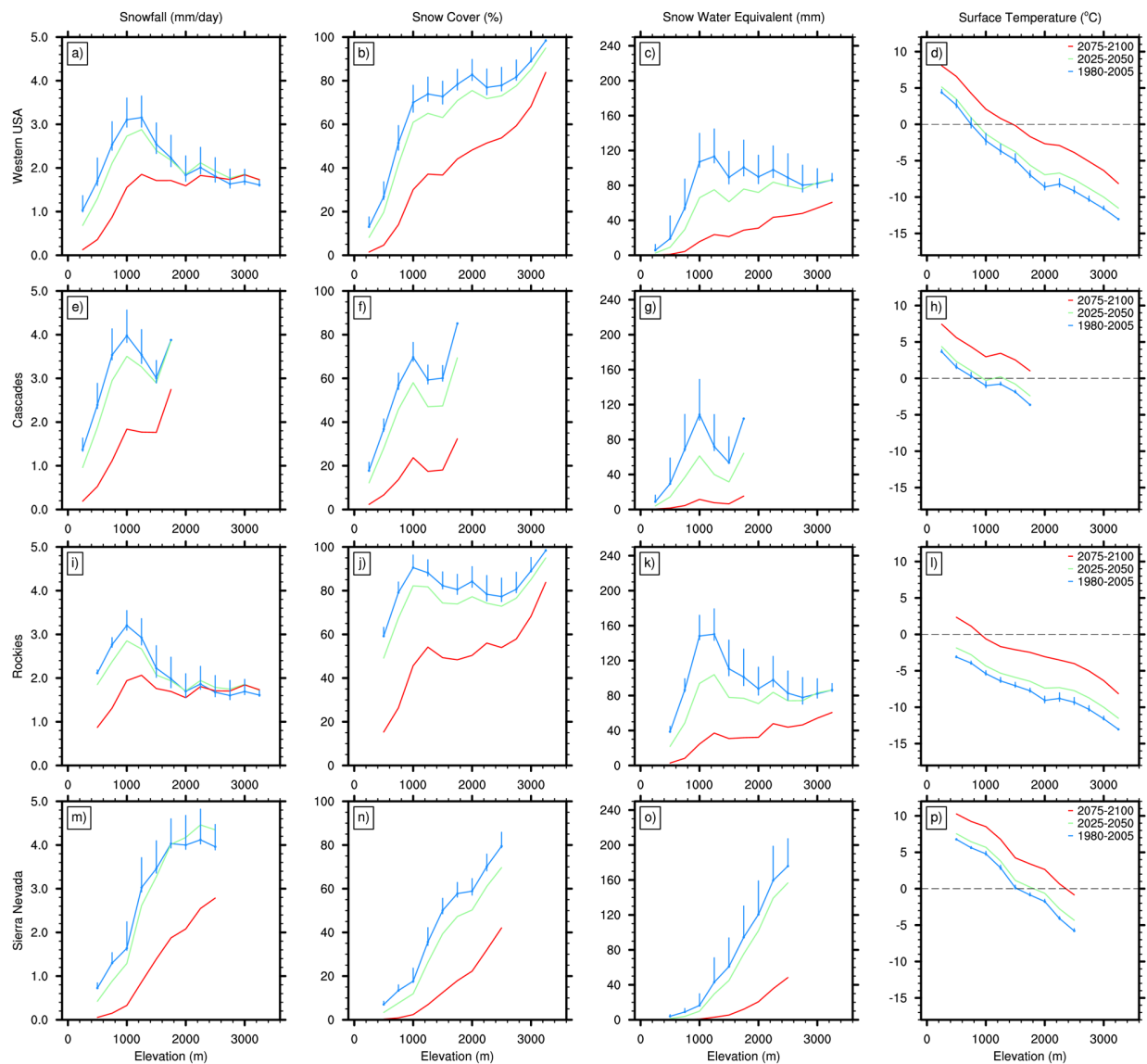
Figure 24: Panel plot of western USA mountain range 250m DJF temporal and spatial average elevational profiles for snowfall, snow cover, SWE, and surface temperature for 1980-2005 (blue), 2025-2100 (green), and 2075-2100 (red) within VR-CESM28. The 250m profiles for the total western USA mountain region are highlighted in a-d, Cascades in e-h, Rockies in i-l, and the Sierra Nevada m-p. To help in assessing historical simulated variability in comparison to the RCP8.5 forcing, sample standard-error bars were added at each elevation interval onto the historical simulation elevation profile. For surface temperature, a 0 °C temperature threshold (freezing-line) is plotted with a dotted line for visual guidance.
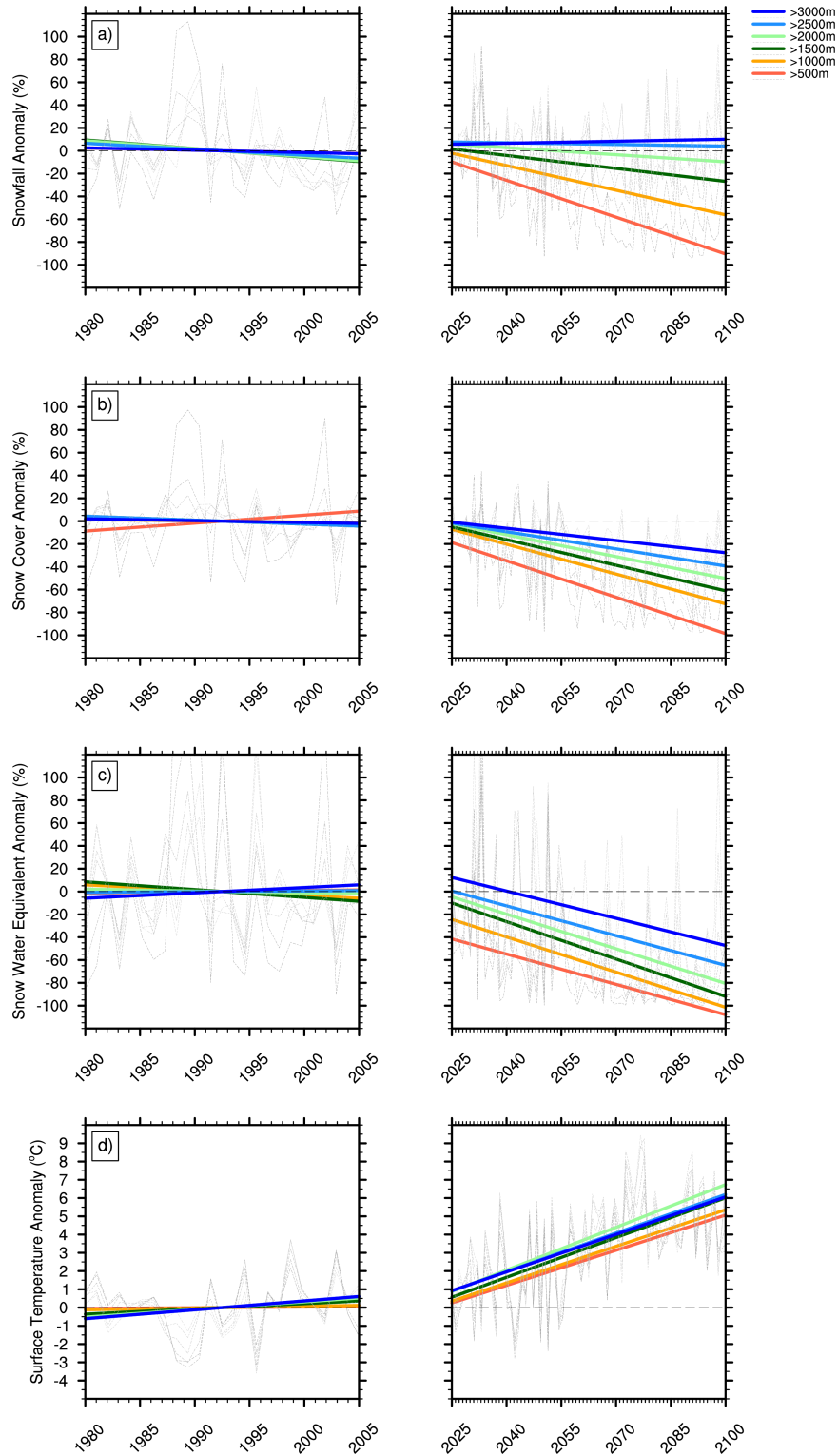
Figure 25: Panel plot of 500m interval elevation bands within the western USA mountain region for 1980-2005 and RCP8.5 2025-2100 DJF trends for (a) snowfall, (b) snow cover, (c) SWE, and (d) surface temperature anomalies for the VR-CESM28 simulations. The winter season variability for each 500m elevation band are highlighted in a lighter-to-darker grayscale dashed line based on lower-to-higher elevation bands. A dashed line is drawn at the zero anomaly y-intercept for visual guidance.

Chapter 3 - Truncation vs Transport - A Variable-Resolution CESM Case Study of the Comparative Importance of Model Resolution and Microphysics in a Mountainous Region

Abstract

Mountains are natural dams that impede atmospheric moisture transport and water towers that cool, condense, and store precipitation. They play a pivotal role in the western US where precipitation is seasonally intermittent and snowpack is crucial to meet water demands. With anthropogenic climate change, the processes shaping the lifecycles of mountain snowpack must be understood. Global-to-regional modeling tools such as variable-resolution in the Community Earth System Model (VR-CESM) can help to develop new understanding of mountain snowpack lifecycles. This paper continues the assessment of VR-CESM in modeling mountain hydroclimatology to understand the role of horizontal resolution (28 km, 14 km, 7 km, and 3.5 km) and microphysics (28 km and 14 km), specifically the diagnostic Morrison and Gettelman (2008) (MG1) scheme vs the prognostic Gettelman et al (2015) (MG2) scheme. The six-member simulation ensemble was performed from 1999-2015 with the F_AMIP_CAM5 component set, which couples the atmosphere-land models and prescribes ocean data. We show that when MG1 is employed, model resolution provides essentially no benefit at scales <14 km to accurately represent California's mountain hydroclimatology. Conversely, with MG2 at 14 km resolution, substantial improvements occurred with DJF climate average precipitation, snow cover and snow water equivalent within 6% of the Parameter-elevation Relationships on Independent Slopes Model (PRISM), the Moderate Resolution Imaging Spectroradiometer (MODIS), and the Landsat-Era Sierra Nevada Snow Reanalysis (SNSR) datasets. Further, mountain windward/leeward distributions were vastly improved and DJF seasonal Pearson correlations were +0.12 higher than MG1 simulations. A systemic mountain cold bias was found within the VR-CESM ensemble, which worsens with resolution refinement and is unresponsive to choice of microphysics.

Introduction

Mountains act as both a natural dam that impedes atmospheric moisture transport and water tower that cools, condenses, and stores precipitation that is then released as streamflow during seasonally dry periods. This system is enabled through a combination of surface reservoirs, snowpack and groundwater storage. Consequently, mountains are crucial in the western US (WUS) where precipitation is seasonally intermittent and extremes-driven. Water resources in this region are often taxed by precipitation from wintertime atmospheric rivers (ARs) falling in regions that do not enable water catchment systems to capture and store water (Dettinger et al, 2011; Dettinger, 2013). This is especially relevant in California, where 50% (California Data Exchange Center (CDEC), accessed 2017) of total precipitation comes during the months of December, January and February (DJF). Here snowpack deposition, on average, occurs in 5-15 days each year (Dettinger et al, 2011), mainly in the Sierra Nevada mountain range where 60% of the state's consumptive use is derived (Bales et al, 2011), and in which 37% of snow water equivalent (SWE) totals come from nine AR events (Guan et al, 2013). Thus, the capture and storage of snowfall in mountain ranges such as the California Sierra Nevada is particularly important for WUS water management and has been shown to provide a natural water store that is equivalent to 70% of existing man-made reservoir storage (or 35% of the total storage) (Dettinger and Anderson, 2015). With forcings associated with anthropogenic climate change the Sierra Nevada mean snowpack stores are projected to diminish by 30% to 60% by 2100 (Rhoades et al, 2017) and the peak accumulation date will shift earlier by 6-21 days by mid-to-late century (Kapnick and Hall, 2010).

Understanding the range of physical processes in WUS mountainous regions and how they may change with the forcings associated with anthropogenic climate change necessitates the use of climate models that can properly characterize land surface heterogeneity and synoptic-scale storm systems. An accurate representation of WUS orography is particularly important to realistically simulate the capture and storage of available precipitable water from the atmosphere. This is due to the importance of mountain range orientation and perpendicularity to storm tracks, the mountain slope variation impacts on orographic uplift, the corresponding alterations in the precipitation phase, the resultant transport and deposition location of the hydrometeors, and the life cycle of

stored mountain snowpack. For example, the resolution dependence that emerges from critical regional climate drivers was discussed for California in Caldwell (2010), Pavelsky et al (2011), and Pavelsky et al (2012), using an RCM (the Weather Research and Forecasting Model), where simulations conducted at resolutions coarser than 28 km (0.25°) were unable to resolve snowpack totals. This was primarily due to inaccurate treatment of orographic uplift which in turn failed to adjust mountain precipitation from rain to snow. Simulated snowpack trends are important from a water-resources standpoint, but can also have cascading impacts on winter hydroclimate trends via the snow-albedo feedback (Chen et al, 2014a). Last, and most importantly, the accurate representation of storm tracks and synoptic-scale processes that alter them (e.g., teleconnections) necessitates the use of a global climate model (GCM), as teleconnections account for 20-45% of annual precipitation variability in the WUS (Dettinger et al, 1998).

Due to computational constraints, even today's most cutting-edge GCMs rarely push to resolutions finer than 28 km. This results in an inaccurate representation of local topographic features that then have a pronounced impact on the mountain hydroclimatology and produce data with less utility for resource-managers (Leung et al, 2013). To date, WUS hydroclimate research has benefited from a myriad of studies, but uncertainties related to atmosphere-orography interactions remain significant. This is due, in large part, because of the computational burden of running a fully-coupled Earth system model at resolutions necessary to properly characterize the regional orography. To address this problem, downscaling techniques have been developed, such as dynamical downscaling with regional climate models (RCMs) (Giorgi et al, 2009; Mearns et al, 2012), statistical downscaling (Gutzler and Robbins, 2011; Pierce et al, 2013), and/or combinations of the two (Sun et al, 2016; Li et al, 2016). These techniques are certainly more computationally efficient than uniform-resolution GCMs, but other issues persist. Of particular relevance for the WUS, atmospheric river frequency and character is poor at the coarse resolutions typical of GCMs, which in turn leads to inadequate boundary conditions to the RCM. Further, upscaling effects such as the topographic influence on atmospheric blocking cannot be captured by dynamically downscaled models. Inconsistencies between the forcing model and RCM, including physical parameterizations and the underlying topography, can also drive unphysical noise in the resolved region. Some care must also be taken when applying conventional statistical downscaling strategies, as these techniques assume

stationarity and are typically unable to capture non-linear behaviors in mountainous regions (e.g., snow-albedo feedback).

With the advent of variable-resolution refinement capabilities in select climate modeling platforms, such as variable-resolution in the Community Earth System Model (VR-CESM) (Zarzycki et al, 2014b, 2015) and the Model for Prediction Across Scales (MPAS) (Skamarock et al, 2012; Rauscher et al, 2013), climate modelers have gained the ability to glimpse into the future of extremely-high-resolution global scale climate modeling for a fraction of the cost that it would conventionally take to run a global climate model at equivalent resolution (Leung et al, 2013; Sakaguchi et al, 2015). Over the last five years, VR-CESM has gone from an experimental modeling platform to a proven applied research tool for use in regional climate assessment (Rauscher et al, 2013; Zarzycki et al, 2014b; Huang et al, 2016; Rhoades et al, 2016; Huang and Ullrich, 2016), synoptic-scale weather systems (Rauscher and Ringler, 2014), and tropical cyclones (Zarzycki et al, 2014a; Zarzycki and Jablonowski, 2014; Zarzycki et al, 2014a, 2015, 2016; Zarzycki, 2016), and most recently in regional climate change assessments (Rhoades et al, 2017; Huang and Ullrich, 2017).

The relative roles of model grid resolution and sub-grid-scale processes have been debated extensively since the inception of climate models (Arakawa and Schubert, 1974; Arakawa, 2004). To help address this question, the research community has advocated to push climate models to the highest resolution possible through the use of new exascale computing systems (Reed and Dongarra, 2015), focused research and development on sub-grid-scale process development (Randall et al, 2003), and/or worked towards a combination of the aforementioned. This has resulted in a recent surge in research and development in multi-scale modeling (Iorio et al, 2004; Tao et al, 2009; O'Brien et al, 2016), the implementation of scale aware physics (Fan et al, 2015; Gross et al, 2016; Gross et al, 2016), and atmospheric model development that can span both hydrostatic and nonhydrostatic scales (Park et al, 2014b; Heinzeller et al, 2016; Ferguson et al, 2016).

To continue the development of VR-CESM, further establish its utility in modeling mountain hydroclimatology, and to understand the relative role of model resolution and microphysics, specifically the diagnostic Morrison and Gettelman (2008) (MG1) scheme vs the prognostic Gettelman et al (2015) (MG2) scheme, we have performed an ensemble of short climatological simulations using

VR-CESM. The results from this study focus on the hydroclimatology from model simulations at 28 km, 14 km, 7 km, and 3.5 km (the so-called grid-scale truncation scale). These simulations are contrasted against the changes induced by the microphysics treatment of hydrometeors (diagnostic versus prognostic microphysics) at 28 km and 14 km.

The remainder of the paper is organized as follows: Section 2 discusses the design of our study, including the creation of the grids that target California's mountainous regions and associated topographic/surface datasets, along with the multitude of comparative datasets (observational and reanalysis) used in this study to understand and assess VR-CESM's capability to model mountain hydroclimatology in the Sierra Nevada are presented. Section 3 includes the results of the study, followed by conclusions and discussion in section 4.

Experimental Design

CESM Overview

CESM is comprised of stand-alone atmospheric, land-surface, oceanic, sea-ice, and land-ice components that can be fully coupled and/or data prescribed. Our VR-CESM six-member ensemble utilized the scientifically validated version of CESM (1.2.2) and the newly developed MG2 microphysics enabled version (1.5.5) with full atmospheric-land coupling and prescribed sea ice and sea surface temperatures, component set FAMIPC5 (Gates, 1992; Neale et al, 2010; Oleson et al, 2010). Six model permutations have been considered, where either the horizontal resolution or the microphysics scheme were targeted. Horizontal resolution was 28km, 14km, 7km or 3.5km. The microphysics used was either the MG1 or MG2 scheme. A detailed description of the VR-CESM benefits and scalability in the Community Atmospheric Model version 5 (CAM5-SE) and Community Land Model version 4.0 (CLM4-SP) is given in Rhoades et al (2016) and Rhoades et al (2017). Here we briefly discuss the use of VR-CESM beyond hydrostatic scales (>10 km), and the difference between MG1 vs MG2 microphysics.

Currently, the use of VR-CESM beyond hydrostatic scales (∼10 km) is not advised for applied research. Being a hydrostatic model, VR-CESM uses the hydrostatic approximation to replace the prognostic vertical velocity equation with a diagnostic equation. Consequently, terms controlling

horizontal and vertical transport of vertical momentum are neglected, even though these terms are needed for the representation of gravity waves, mountain lee waves, and mesoscale convective systems at scales below ∼10 km. Whereas these features could not be reasonably ignored in numerical weather prediction systems, the impact of the hydrostatic assumption on climatology is less clear, and there remains a need for additional work on this topic. At increasingly fine resolutions, the hydrostatic approximation has shown tendencies towards divergent growth in the vertical velocity compared with nonhydrostatic formulations with increasing refinement and convergence of the aspect ratio (Weisman et al, 1997). Recent analyses by Yang et al (2017) using both hydrostatic and nonhydrostatic formulations of the Weather Research and Forecasting (WRF) model at 36km, 12km, and 4km showed statistically significant divergence in simulated total precipitation in the tropics (20% of domain at 4km), largely due to latent heat release, however differences within midlatitudes were largely diminished (3% of domain at 4km). Nonetheless, we emphasize that our results at grid resolutions finer than 10 km (specifically CAL_VR7 and CAL_VR4) are purely meant for exploratory research and are not advised for applied use. We further emphasize that in all cases topographic smoothing has been applied in accordance with Zarzycki et al (2015) to eliminate any visual evidence of spurious model noise in the vertical pressure velocity.

MG1 and MG2 microphysics in CESM are almost identical in all aspects, except for their treatment of precipitation (Gettelman et al, 2015). Both MG1 and MG2 use two moments (i.e., mass and number mixing ratios) to determine hydrometeor size distributions which affords more degrees of freedom in determining things such as rain drop size and evaporation rates. However, MG1 uses diagnostic hydrometeors (i.e., simulated precipitation is inferred from a combination of variables), whereas MG2 uses prognostic hydrometeors (i.e., hydrometeor concentration is "remembered" across timesteps) (Morrison and Gettelman, 2008; Gettelman et al, 2015). To derive precipitation amounts in MG2, mass and number mixing ratios are prognosed and transported for both rainfall and snowfall. This has resulted in an order of magnitude higher accretion to autoconversion ratio between MG1 vs MG2. A more realistic presence of mixed-phase clouds in global CESM simulations, due solely to process rate changes. Both of which have shown resolution-independence from 200 km to 25 km (Gettelman et al, 2015).

VR-CESM Model Grid, Topographical Fields, and Surface Datasets

A set of four VR grids were generated for this study using SQuadGen (Ullrich, 2014), and both employed in CAM5-SE and CLM4-SP (Figure 26a). These grids were developed by first refining from a global base resolution of 111 km to 28 km over the WUS and eastern Pacific, to incorporate atmospheric river source regions. Further VR refinement was then targeted over the California mountainous regions down to resolutions of 28 km (CAL_VR28 MG1 and MG2), 14 km (CAL_VR14 MG1 and MG2), 7 km (CAL_VR7), and 3.5 km (CAL_VR4) using an outline of the Klamath and Sierra Nevada mountainous regions from the EPA's Ecoregion Level III classification system (dashed dark blue outline in Figure 26b). Additionally, elevation thresholds and USGS hydrologic units were used to generate the other Sierra Nevada windward and leeward regions to ensure that they track the mountain ridgeline accurately.

The topographic datasets were derived from a 1 km resolution digital elevation product known as the Global 30 Arc-Second Elevation (GTOPO30). Careful consideration was taken to ensure that the smoothness of each of the grid topographies were sufficient to dampen potential high-frequency model simulation error derived from the higher-order properties of the dynamical core solvers. More information on the technical details of the topography smoothing operator can be found in Zarzycki et al (2015). The resultant topographies are shown and differenced from the original GTOPO30 dataset in Figure 26c. The topographic mean and variability is improved at higher resolution, especially when compared to a conventional 111 km (1°) uniform-resolution version of CESM (CESM_111). This is further apparent in Figure 27a where the elevation classes are significantly more realistic with increasing CAL_VR resolution compared to the GTOPO30 dataset, especially when compared to CESM_111.

High-resolution year 2000 surface datasets available in CLM4-SP were used for all simulations (standard CLM4-SP utilizes 55 km surface datasets). This data provides 5 km to 9 km resolution characterizations of plant functional types (PFTs), soils, lakes, wetlands, crops, and urban areas. This is apparent in Figure 27 (b-c), which depicts the percent change in forest cover between CAL_VR28 and CAL_VR4 for the two major PFT tree species in California, Temperate Needleaf Evergreen and Boreal Needleleaf Evergreen. For all simulations, surface characteristics are assumed

to be static for the year 2000, a reasonable approximation for our near-term simulation period of 1999-2015.

Mountain Climate Comparative Datasets

The spatial and temporal resolutions for the CAL_VR six-member ensemble and the comparative reanalysis and/or observational datasets used in this study are given in Table 11. The comparative datasets used in this study were chosen on their merit to characterize specific hydroclimate variables of interest. Additionally, each of the datasets were standardized from 1999-12 to 2015-02 to climate daily normal (i.e., each day across all years evaluated are averaged together), DJF average, and DJF climate average using the netCDF Operators (NCO - Zender (2008)) and the Climate Data Operators (CDO - Schulzweida et al (2007)). Although California's winter season spans November though March, DJF was used as it accounts for 50% of the annual total precipitation (California Data Exchange Center (CDEC), accessed 2017) and minimizes errors associated with snow related feedbacks in the beginning of the accumulation period and end of the ablation period (Raleigh et al, 2013). These errors arise due to the ephemerality of snow at this time that may fail to be captured by current monitoring techniques. The remainder of this section describes the principal comparative datasets used in our study:

- The Parameter-elevation Relationships on Independent Slopes Model (PRISM) dataset utilizes over 10,000 quality controlled observational station datasets along with a climate-elevation regression for each DEM grid-cell to create a daily 4 km total precipitation and two-meter surface temperature spatially continuous CONUS product (Daly et al, 2008). The observed values are then updated for micro-climate variations in atmospheric vertical layer location, coastal proximity, elevation, geographic location, orographic effectiveness, and topographic orientation. The net result of this extensive quality assurance is a substantial improvement in gridded daily climate variables compared to the alternative WorldClim and Daymet datasets, especially in mountainous and coastal areas of the WUS (Daly et al, 2008). Further, the choice to use the PRISM 4 km total precipitation and surface temperature products for comparison to our six-member simulation ensemble was based on our confidence built from use in prior studies which highlighted no statistical difference between several other major precipitation

91

products (Huang et al, 2016), the extensive micro-climate interpolation strategies utilized, and the wide use within the mountain climate community. With that said, Henn et al (2016) has shown that gridded precipitation products, such as PRISM, have shown a systemic underestimation of total precipitation maxima due to interpolation at higher elevations when a complete water balance is assessed via streamflow gauges and ET measurement constraints.

- The Moderate Resolution Imaging Spectroradiometer (MODIS) satellite product (MOD10CM V005) provides global monthly 5 km snow cover (Hall and Riggs, accessed 2016). The product is quality-assured for cloud cover by using visible and short-wave near-IR spectral bands and a snow mapping algorithm with a Normalized Difference Snow Index (NDSI). We have chosen to use the MODIS 5 km snow cover product for comparison to our six-member simulation ensemble based on its use in prior studies (Rhoades et al, 2016) and its agreement to ground based measurements at 93% accuracy for its various products at 28 km, 5 km, and 0.5 km resolution. A recognition that the efficacy of MODIS as a comparative dataset is also dependent on the scale and mountain region assessed. This stems from the sensitivity to snow ephemerality, forest cover, and terrain (Hall and Riggs, 2007).

- The Global Historical Climatology Network (GHCN) provided by the National Oceanic and Atmospheric Administration (NOAA) encompasses over 100,000 observational stations around the globe recording daily observations of 40 meteorological variables (Menne, M.J., I. Durre, R.S. Vose, B.E. Gleason, and T.G. Houston, 2012). In the Sierra Nevada, 401 NOAA-GHCN meteorological stations measure total precipitation and snowfall and are located between 35.65° to 39.67° latitude by -121.28° to -117.39° longitude. Of the 401 stations, 213 stations are located in the windward side of the Sierra Nevada and 106 stations have continuous measurements from 1999-2015, with an elevational coverage of 64m to 2826m. (Figure 26b). This dataset represents the most comprehensive in-situ station network for total precipitation and snowfall monitoring stations in the western US, a focal reason for its comparative use in this study.

- The Landsat-Era Sierra Nevada Snow Reanalysis (SNSR) dataset by Margulis et al (2016a) characterizes SWE for 20 watersheds within the California Sierra Nevada at 90 m resolution from 1985 to 2015. The reanalysis estimates for SWE are derived from a Bayesian data as-

simulation technique that utilizes 30 m elevation estimates from the ASTER and the National Land Cover Database, hourly 14 km meteorological inputs from the North American Land and Data Assimilation Database phase 2 (NLDAS-2), and snow cover area and vegetation cover fractions derived from the NASA Landsat 5, 7, and 8 satellite data. The dataset was validated against 108 snow pillows and 202 snow course in-situ SWE measurements (not incorporated into the assimilation technique) and found to correlate at 0.97 across all sites (Margulis et al, 2016a,b). This dataset presents a high-quality SWE product that was sorely lacking in previous VR-CESM studies (Rhoades et al, 2016).

Results

Figure 28 presents the simulated DJF climate average differences for total precipitation, snow cover, SWE and surface temperature associated with solely changing horizontal grid resolution to 28 km, 14 km, 7 km and 3.5 km. Overall, CAL_VR MG1 simulated more total precipitation, snow cover, and SWE, but colder surface temperature during the winter season (Table 12). The average simulated bias of total precipitation, snow cover and SWE were between +0.8 mm/day to +1.1 mm/day, -0.5% to 11% and -27 mm to 26 mm, respectively, within the California Mountain Region. Generally, on the leeward side of the Sierra Nevada, total precipitation and SWE showed a small negative bias and less snow cover overall (Figure 28). The Sierra Nevada total precipitation windward/leeward ratios were 3x larger than the PRISM dataset, with nearly a 1.5x overestimation on the windward side and 50% underestimation on the leeward side (Table 13). The biases associated with the windward/leeward ratios highlight that CAL_VR MG1 simulations had significant issues with properly distributing total precipitation, snow cover and SWE in the Sierra Nevada. To measure the spatial similarities from season-to-season between the comparative datasets and the CAL_VR simulations within the California Mountain Region, Pearson pattern correlation coefficients were computed. The Pearson pattern coefficients are a measure of the linear correlation between simulated and observed where a sum of squares is computed for a common variable for each dataset and related to the co-variability of that variable between both datasets. For each CAL_VR simulation, 16 DJF Pearson pattern coefficients were computed for the 1999-2015 study period. The minimum, average, and maximum DJF Pearson pattern correlation for each CAL_VR simula-

tion is shown in Table 13. The average DJF Pearson pattern correlations for the CAL_VR MG1 ensemble ranged from 0.5 to 0.7 for total precipitation, snow cover and SWE, with no significant difference found with changes to horizontal grid refinement. Comparatively, surface temperature simulations had Pearson pattern correlations >0.9. However, the surface temperature simulations also exhibited a clear systematic cold bias with CAL_VR28 MG1 at -2.4 K and CAL_VR4 MG1 at -3.7 K (Table 13). The surface temperature cold bias was especially pronounced in the mountainous regions throughout all resolutions. Several hypotheses as to why this might have occurred are discussed in the conclusions. Thus, solely refining horizontal resolution to more realistically represent topography and land cover in VR-CESM did not alleviate systematic model issues such as the windward/leeward total precipitation ratios and surface temperature cold biases, but merely localized the biases.

Figure 29 highlights the DJF climate average differences for total precipitation, snow cover, SWE and surface temperature between the MG1 (diagnostic treatment of hydrometeors) and MG2 (prognostic treatment of hydrometeors) microphysics schemes implemented in CAM at horizontal grid refinements of 28 km and 14 km. The CAL_VR14 MG2 simulation most closely represented the comparative dataset values for total precipitation, snow cover, and SWE results by significantly alleviating the DJF seasonal mean total precipitation bias to within +0.1 mm/day (+2%) of PRISM, +5.5% of MODIS, and -3.5 mm (-4.6%) of SNSR throughout the California Mountain Region. Additionally, the total precipitation, snow cover and SWE windward/leeward ratios in the Sierra Nevada in CAL_VR14 MG2 (CAL_VR28 MG2) were much improved with values of 3.0 (2.6), 1.1 (0.9), and 2.0 (1.3) when compared with the PRISM (2.9), MODIS (1.2), and SNSR (2.2) datasets. This is especially apparent when compared with the overestimation of the windward/leeward ratios within the CAL_VR MG1 simulations which ranged between 7.8 to 9.7 for total precipitation, 2.3 to 2.8 for snow cover, and 6.2 to 12 for SWE (Table 13). Correspondingly, CAL_VR MG1 precipitation was far too localized on the windward side of the Sierra Nevada, whereas CAL_VR MG2 more realistically distributed total precipitation, snow cover, and SWE on the windward/leeward of the Sierra Nevada. This result is attributed to both the resolution dependence of topography and the recent advances by Gettelman et al (2015) to prognose hydrometeor mass and number mixing ratios. The topographic representation drives the overall atmosphere-land interaction to

create precipitation. The prognostic hydrometeor representation in MG2 alters the process rates, increases the presence of mixed phase clouds, and advects total precipitation in complex terrain in a more realistic manner. In the CAL_VR MG2 simulations, the mean DJF seasonal Pearson pattern correlations across all of the hydroclimate variables more closely matched the comparative datasets by +0.12 when compared with the CAL_VR MG1 simulations, except surface temperature in which the spatial correlations in both CAL_VR MG1 and CAL_VR MG2 results were above 0.90. Thus, an increase in horizontal refinement coupled with the new prognostic treatment of hydrometeors in the sub-grid-scale microphysics provided a vastly improved approximation for total precipitation, snow cover, and SWE at DJF climatological and DJF seasonal temporal evaluations, especially in proper windward/leeward distributions. This breakthrough provides clear benefit to water managers and hydrological modelers alike who care about future climate model projections of the magnitude, phase, and location of precipitation deposition for assessments of water availability in mountainous regions. Of interest to future model development, systematic cold bias in surface temperature and snow cover was persistent throughout all four of the model resolutions and the two sub-grid-scale microphysics schemes. This may highlight some of the pending model process uncertainties associated with lapse rates in mountainous environments, in-cloud ice phase processes, and/or observational uncertainties.

Model efficacy in distributing total precipitation and capturing the daily climate cycles of surface temperature and SWE over the entire California Mountain Region and within the windward and leeward sides of the Sierra Nevada over an average water year is represented in Figure 30. Each of the plotted lines indicate a difference of a given CAL_VR simulation from that of the comparative dataset used for total precipitation, SWE, and surface temperature highlighted in Table 11. Blue lines highlight the ensemble of CAL_VR simulations which solely increased horizontal resolution and red lines indicate the set of ensemble members with changes in microphysics scheme. The vertical black line delineates the accumulation period and the melt period at the historical peak accumulation date of April 1st. For surface temperature, a 30-day running average filter was applied to clarify individual model performance. The effects of solely refining horizontal resolution from 28 km to 3.5 km leads to accumulated total precipitation that is positively biased and dominated by windward (leeward) depositions that are too wet (too dry). Interestingly, the effects of increasing

model resolution coupled with the change in microphysics from diagnostic to prognostic treatment of cloud hydrometeors remediates much of the aforementioned biases. This is seen when looking at the CAL_VR14 MG2 results which produces the smallest average (range) of bias in accumulated total precipitation in the California Mountain Region of +48 mm (+120 mm), especially on the windward side of the Sierra Nevada. The divergence in how total precipitation was dispersed influence how the mountain snowpack accumulation and melt periods were simulated. For example, the California Mountain Region and windward side of the Sierra Nevada in CAL_VR MG1 and CAL_VR MG2 (save for the CAL_VR28 MG1 simulation) generally behaved in converse to one another. The CAL_VR MG1 (CAL_VR MG2) simulations were positively (negatively) biased during the accumulation and melt cycle in the California Mountain Region and windward side of the Sierra Nevada. Akin to the total precipitation results, modeled SWE in CAL_VR MG2 most closely tracked the SNSR winter mountain snowpack accumulation cycle, especially when the aggregate of all assessed mountain regions were accounted for. Interestingly, divergence away from SNSR was exhibited near the historical peak accumulation month (March to April) which may be an indication that melting factors that shape the simulated snowpack may be too strong and inhibit proper persistence into the spring season. Notably, the persistent cold bias in surface temperature was unaffected by increasing horizontal resolution and/or modifying the microphysics scheme. The ensemble average surface temperature bias for the CAL_VR simulations within the California Mountain Region was -2.2 K with a range of 7.7 K . A clear systemic cold bias persists throughout much of the fall, winter and spring seasons with a general increase in bias with finer horizontal resolution, likely a result of resolving more elevation classes.

As important as the model efficacy in properly representing the average spatial patterns and the proper distribution of mountain windward and leeward hydroclimatology is the ability to characterize the elevational profiles of precipitation variables. Figure 31 highlights the ability of the CAL_VR ensemble to represent the DJF climate average 500m elevational profiles shown in the comparative datasets based on changing horizontal resolution (blue) and/or microphysics (red). Vertical black lines indicate the DJF seasonal spread (i.e., standard error) for the comparative dataset used at each 500m elevation interval. Overall, solely refining horizontal resolution did not offer any advantage to modeled elevational profiles with a general wet (dry) bias in windward (leeward) total precipitation,

and an increased surface temperature cold bias with increasing elevation. The windward wet bias in the CAL_VR MG1 results are likely indicative of the microphysics sensitivity to orography with an absolute ensemble bias of 2.7 mm/day per 500m compared with the CAL_VR MG2 absolute ensemble bias of 1.3 mm/day per 500m. Similar to the trends highlighted before, a combination of increasing horizontal resolution and modifying the microphysics scheme (e.g., CAL_VR14 MG2) represented the most favorable results with the smallest windward total precipitation absolute bias of 0.6 mm/day per 500m. Although total precipitation bias trends were ameliorated by the combination of refinement of horizontal resolution and changes in the sub-grid-scale microphysics, the persistent cold bias found throughout all six members of the CAL_VR ensemble generally worsens with increasing elevation. From 0m to 500m, the average cold bias in the California Mountain Region (windward side of the Sierra Nevada) was -1.8 K (-1.5 K) and at the maximum shared elevation of 2500m to 3000m the average cold bias increased to -5.1 K (-5.4 K), with an average increment of bias of -0.7 K (-0.8 K) per 500m elevation gained. It should be noted that this could also be partially attributed to the interpolation method used by PRISM at the ridgeline of the mountains where in-situ station data is more scarce (Henn et al, 2016). For snow cover, solely refining grid resolution within the CAL_VR MG1 ensemble provided no added value to the proper representation of the trends with elevation in the California Mountain Region, windward side of the Sierra Nevada, and/or the leeward side of the Sierra Nevada when compared to MODIS. The CAL_VR MG1 absolute ensemble average bias for snow cover was 10% (12%) for the windward (leeward) side of the Sierra Nevada. The updated sub-grid-scale microphysics in the CAL_VR MG2 ensemble appears to ameliorate 4% of the bias on both the windward and leeward side of the Sierra Nevada, however across both CAL_VR MG1 and CAL_VR MG2 a pervasive issue with low elevations (1000m to 1500m) is present, a region where snowpack is most ephemeral and the snowline is most variable. Last, SWE elevation trends indicate further benefits to the use of the CAL_VR MG2 model setup. The absolute average SWE bias across all 500m elevation trends in CAL_VR MG1 was 57 mm with a minimum (maximum) bias of -176 mm (14 mm), whereas CAL_VR MG2 results had an absolute average SWE bias of 15 mm and a minimum (maximum) of -50 mm (7 mm). Generally, CAL_VR MG1 has a predictable positive (negative) SWE bias on the windward (leeward) side of the Sierra Nevada, comparable to the total precipitation results. CAL_VR MG2 tracks similar trends as shown in total precipitation with minimum SWE bias across all of the 500m

elevation classes and the windward and leeward sides of the Sierra Nevada. Thus, although surface temperature had a clear cold bias which worsened at higher elevations, the orographic total precipitation and proper distributions of windward/leeward distributions of SWE highlight the benefits of the updated CAL_VR MG2 simulations.

The model efficacy in generating snowfall with elevation gain in mountainous areas is evaluated in the windward side of the Sierra Nevada over the 1999-2015 period. Figure 32 presents the DJF snowfall/total precipitation (i.e., snowfall efficiency) ratios with 500m elevation intervals for the CAL_VR ensemble members and the NOAA-GHCN in-situ dataset. Intuitively, snowfall is rarely observed under 500m elevation, but the ratio of snowfall/total precipitation increases with elevation gain with snowfall efficiency values over 0.5 at elevations higher than 2000m. Generally, CAL_VR MG1 generates slightly more snowfall than CAL_VR MG2, and the snowfall/total precipitation ratios do not show significant difference and trend with refinement in horizontal resolution. Comparing the snowfall efficiencies between the CAL_VR MG1 (CAL_VR MG2) ensemble against the NOAA-GHCN dataset highlights that CAL_VR generally overestimates snowfall in low-elevation regions with a +92% (+64%) bias within the 500m-1000m elevation interval, but underestimates snowfall by -21% (-31%) in the 1500m-2000m elevation intervals. The snowfall efficiency analysis is hindered by the fact that station data on the windward side of the Sierra Nevada (106 total) becomes more scarce with elevation with 73 stations between 0m-1000m, 23 stations between 1000m-2000m, and 7 stations between 2000m-3000m.

Conclusions

The overarching goal of this paper was to utilize a recently developed regional downscaling technique (VR-CESM) to assess the relative importance of horizontal resolution and sub-grid-scale microphysics in determining modeled hydroclimate trends within complex terrain over a near-term historical time-frame of 1999-2015. Additionally, the best available comparative datasets for total precipitation (PRISM), snow cover (MODIS), SWE (SNSR), and surface temperature (PRISM) were compiled and utilized for the model evaluation over orography in California.

Through this analysis the following conclusions were made:

(1) Simply increasing model horizontal resolution to more realistically capture land surface heterogeneity (terrain and land-cover), while maintaining a diagnostic microphysics parameterization, did not improve modeled mountain hydroclimate statistics. This result follows CAL_VR MG1 simulations of over precipitation on the windward side of the Sierra Nevada (+1 mm/day) that led to excessively high average windward/leeward ratios in total precipitation of 8.8 (3x greater), snow cover of 2.7 (2x greater), and SWE of 11 (5x greater) for the CAL_VR MG1 ensemble when compared to the windward/leeward ratios for PRISM (2.9), for MODIS (1.2), and for SNSR (2.2). Last, seasonal DJF Pearson pattern correlations were constrained between 0.5 to 0.7 across total precipitation, snow cover, and SWE, with snow cover the most highly correlated and total precipitation the lowest. Average DJF seasonal correlations for surface temperature were highest across all simulations at 0.9 , but it is cautioned that a general cold bias between -2.4 K to -3.7 K for the DJF climate average was found throughout all CAL_VR simulations.

(2) The development of a new prognostic microphysics scheme by Gettelman et al (2015) in CAM coupled with more realistic representations of orography were key in more properly representing the DJF climate and seasonal averages of total precipitation, snow cover, and SWE throughout the California Mountain Region. The CAL_VR MG2 simulations most closely represented the comparative datasets used for total precipitation, snow cover, and SWE results by alleviating the DJF seasonal mean bias to within +2% of PRISM, +6% of MODIS, and -5% of SNSR. total precipitation, snow cover and SWE windward/leeward distributions in the Sierra Nevada in CAL_VR14 MG2 (CAL_VR28 MG2) were much improved at 3.0 (2.6), 1.1 (0.9), and 2.0 (1.3) when compared with the PRISM (2.9), MODIS (1.2), and SNSR (2.2) datasets. Further, the DJF seasonal Pearson pattern correlations for CAL_VR MG2 simulations across all of the hydroclimate variables more closely matched the comparative datasets by +0.12 when compared with the CAL_VR MG1 ensemble. Although a positive total precipitation bias was shown across most of the CAL_VR ensemble, this could also be partially attributed to interpolation uncertainties in PRISM.

(3) Further benefits in using the prognostic MG2 microphysics scheme were shown within the daily climate average life cycles of CAL_VR MG1 and CAL_VR MG2. The least average

(range) of bias in accumulated total precipitation was found for CAL_VR MG2 in the California Mountain Region at +48 mm (+120 mm), especially on the windward side of the Sierra Nevada. Similarly, the SWE accumulation cycle closely matched SNSR until the historical peak accumulation months of March to April, after which SWE steadily became low biased. Although comparative dataset uncertainty may be partially implicated, this may also be an indication that spring dependent melting factors such as temperature thresholds, water vapor concentrations, and/or radiational effects in VR-CESM may influence the simulation in spring months too strongly, which in turn inhibits SWE persistence. Throughout all CAL_VR simulations a systemic cold bias is evident with an ensemble average (range) of bias of -2.2 K (7.7 K) which persists throughout much of the fall and winter seasons and generally becomes worse with refinement of model horizontal resolution (probably due to more elevation classes being resolved).

(4) Solely refining horizontal resolution did not result in more realistic elevational profiles, but rather highlighted the MG1 sensitivity to orographic uplift with a general wet (dry) bias in windward (leeward) total precipitation. The CAL_VR MG1 absolute ensemble bias of 2.7 mm/day per 500m compared with the CAL_VR MG2 absolute ensemble bias of 1.3 mm/day per 500m highlights the partial alleviation of this orographic sensitivity. CAL_VR14 MG2 represented the most favorable results for Sierra Nevada windward total precipitation, snow cover, and SWE with an absolute average bias (% bias reduction from CAL_VR MG1) of 0.6 mm/day per 500m (54% bias reduction), 6.4% per 500m (36% bias reduction) and 17 mm per 500m (70% bias reduction), respectively. A worsening surface temperature cold bias with increasing elevation was persistent throughout all CAL_VR simulations. An average increment of bias of -0.7 (-0.8) K per 500m elevation gained was found in the California Mountain Region (windward side of the Sierra Nevada). Further, minimal surface temperature bias was found at lower elevations, -1.8 K (-1.5) K, and maximized at the highest shared elevation of 2500m-3000m, -5.1 K (-5.4) K, for the California Mountain Region (windward side of the Sierra Nevada). Thus, although surface temperature had a clear cold bias which worsens at higher elevations, the orographic total precipitation and proper distributions of windward/leeward distributions of snow cover and SWE highlight the benefits of the updated CAL_VR MG2

simulations.

(5) Snowfall efficiency (snowfall/total precipitation) was higher in CAL_VR MG1 vs CAL_VR MG2, however refinement of horizontal resolution and a more realistic topography representation did not significantly alter snowfall efficiency. When compared with the NOAA-GHCN in-situ measurements, the CAL_VR MG1 (CAL_VR MG2) ensemble generally overestimates snowfall efficiency in low-elevation regions with a +92% (+64%) bias from 500m to 1000m and underestimates snowfall efficiency by -21% (-31%) from 1500m to 2000m. Unfortunately, the snowfall efficiency analysis is hampered by the scarce station densities over the study time frame.

Overall, the CAL_VR ensemble identified that a systemic cold bias is apparent in mountainous environments. This cold bias worsens with elevation and is indicative that the amalgamation of processes that drive lapse rates in VR-CESM may not be sufficiently represented yet (e.g., turbulence scheme, snow-albedo feedback, cloud cover, and/or specific humidity profiles). This is an understandable bias in global scale models as they have not been developed at the resolutions that are accessible by the VR technique (i.e., <28 km). We present several hypotheses as to why the VR-CESM model may misrepresent key hydroclimate processes, and suggest these are viable targets for future development via the VR-CESM framework:

(1) The boundary layer turbulence scheme may be overly stable in the presence of snowpack, thus creating a cold-biased boundary layer that in turn affects the surface temperature (likely worsened with an increase in elevation).

(2) The snow-albedo feedback may not be sufficiently characterized in CLM due to several key parameterization choices. For example, snow cover in CLM is described by a hyperbolic tangent function. This function incorporates a tuning for global scale radiative balance via its m parameter, which modulates the rate of change of the snow cover s-curve behavior (bounded between 0% and 100% snow cover). This m parameter modulates the rate of change between 0% and 100% snow cover and may not apply to the characteristics of an individual mountain range having unique micro-climate (e.g., proximity to ocean, water-vapor concentrations,

and forest cover) and physical factors (ie.g., latitude, orientation, slope, and peak-to-valley variability) that may influence its snow cover tendencies.

(3) The cold bias with elevation could in turn low bias specific humidity concentrations at higher elevations and in turn amplify the rate of change of surface lapse rates. This would then impact the lifecycle of the bulk snow density of newly fallen snow which is solely a function of three temperature thresholds (Tatm $> +2\,^{\circ}\text{C}$; $+2\,^{\circ}\text{C} >$ Tatm $> -15\,^{\circ}\text{C}$; Tatm $< -15\,^{\circ}\text{C}$). Further, condensational heating affects are not directly accounted for in how CLM4 models snowpack lifecycles which prevents important energy fluxes in to/out of the snowpack.

(4) Cloud cover percentage in mountainous regions may be biased, leading to issues with long-wave radiation feedbacks which are important for mountain snowpack, a virtual blackbody in the longwave spectrum. Since snowfall efficiency per 500m elevation gain were found to be insensitive to topographic resolution, this is potentially a source of error for SWE lifecycles (leading to a low bias)

(5) Structural decisions made in the development of CLM have artificially capped SWE totals to 1000 mm. These types of decisions need to be identified and tested via sensitivity analysis at the regional scales that VR-CESM can now reach.

In this study, VR modeling has been demonstrated as a valuable approach for assessing global climate model sensitivities at sufficient resolutions to realistically represent orography at reduced computational cost. This study highlights the benefit of using the VR-CESM downscaling method to garner a glimpse of the future of extremely-high resolution global modeling, assess its ability to represent key hydroclimate processes in complex terrain, and, finally, pinpoint future model development needs. Further work is needed with VR-CESM to understand and isolate potential issues in the aforementioned processes and address the systemic biases found in this study. Additionally, the authors will explore the potential benefits of using a nonhydrostatic dynamical core (WRF) coupled with outputs from the hydrostatic VR-CESM simulations produced here to assess any added value in the representation of mountain hydroclimate processes.

Tables

Table 11: California mountain region hydroclimate datasets.

Climate Dataset		Hydroclimate Variable	Spatial Resolution	Temporal Resolution	Analysis Time − Series
VR-CESM					
	CAL_VR28 - MG1	total precipitation, snowfall, snow cover, SWE, surface temperature	28 km	Daily	1999-2015
	CAL_VR28 - MG2	total precipitation, snowfall, snow cover, SWE, surface temperature	28 km	Daily	1999-2015
	CAL_VR14 - MG1	total precipitation, snowfall, snow cover, SWE, surface temperature	14 km	Daily	1999-2015
	CAL_VR14 - MG2	total precipitation, snowfall, snow cover, SWE, surface temperature	14 km	Daily	1999-2015
	CAL_VR7 - MG1	total precipitation, snowfall, snow cover, SWE, surface temperature	7 km	Daily	1999-2015
	CAL_VR4 - MG1	total precipitation, snowfall, snow cover, SWE, surface temperature	3.5 km	Daily	1999-2015
Reference Datasets					
	SNSR	SWE	90 m	Daily	1999-2015
	MODIS	snow cover	5 km	Monthly	2000-2015
	NOAA GHCN	total precipitation, snowfall	401 stations	Daily	1999-2015
	PRISM	total precipitation, surface temperature	4 km	Daily	1999-2015

Table 12: Summary statistics for winter season (DJF) hydroclimate variables by the VR-CESM and comparative datasets within the California Mountain Region.

Climate Dataset	Mean	Standard Deviation	Min	Lower Quartile	Median	Upper Quartile	Interquartile Range	Max
Total Precipitation (mm/day)								
CAL_VR28 MG1	6.95	2.82	1.72	4.40	7.63	8.38	3.98	12.5
CAL_VR28 MG2	7.81	3.50	3.70	4.81	6.81	9.77	4.97	14.7
CAL_VR14 MG1	7.01	1.65	4.21	5.76	6.76	7.88	2.12	9.88
CAL_VR14 MG2	6.20	2.80	3.47	3.47	4.78	8.35	4.88	12.1
CAL_VR7	7.15	3.33	2.68	3.88	6.04	9.22	5.34	12.8
CAL_VR4	6.92	2.81	2.62	4.83	6.55	8.03	3.21	12.8
PRISM	6.07	1.83	3.04	4.97	6.00	7.08	2.11	9.8
Snow Water Equivalent (mm)								
CAL_VR28 MG1	57.0	45.6	10.3	26.8	36.3	72.2	45.4	166
CAL_VR28 MG2	62.4	27.5	19.5	35.5	61.6	73.2	37.7	115
CAL_VR14 MG1	111	70.3	28.1	49.2	103	136	87.1	279
CAL_VR14 MG2	80.9	80.0	13.6	25.6	38.4	109	83.4	242
CAL_VR7 MG1	109	72.5	16.0	48.8	88.1	191	142	216
CAL_VR4 MG1	104	59.8	18.6	51.3	99.4	136	84.2	224
SNSR	84.4	41.5	20.0	41.1	86.7	109	68.2	152
Snow Cover (%)								
CAL_VR28 MG1	40.3	15.3	13.2	28.5	38.9	47.2	18.8	75.1
CAL_VR28 MG2	44.2	7.80	27.4	40.5	42.9	49.2	8.7	58.6
CAL_VR14 MG1	52.2	11.4	31.5	44.8	53.6	58.6	13.8	72.9
CAL_VR14 MG2	46.3	18.7	21.6	32.6	41.7	53.2	20.6	82.1
CAL_VR7	50.2	13.9	28.3	40.4	49.4	60.7	20.3	70.2
CAL_VR4	50.3	12.4	23.3	41.6	49.5	59.3	17.7	70.6
MODIS	40.8	13.0	14.7	25.2	44.0	47.9	22.7	56.4
Two-Meter Surface Temperature (K)								
CAL_VR28 MG1	274	1.39	271	273	274	275	1.54	277
CAL_VR28 MG2	274	1.01	272	273	274	275	1.61	276
CAL_VR14 MG1	273	0.89	272	273	273	274	1.30	275
CAL_VR14 MG2	274	1.66	270	273	274	274	1.61	276
CAL_VR7 MG1	273	1.26	271	272	273	274	1.34	276
CAL_VR4 MG1	273	1.36	269	272	273	274	2.04	274
PRISM	276	1.07	274.6	276	276	277	1.07	279

Table 13: Summary statistics for the difference of winter season (DJF) hydroclimate variables between VR-CESM and the comparative datasets within the California Mountain Region.

| Climate Dataset	Mean	Interquartile Range	Minimum	Mean	Maximum	Windward/Leeward Ratio
Total Precipitation (mm/day)						
		Difference	*Pearson − Pattern Correlation*			
CAL_VR28 - MG1	0.88	1.87	0.26	0.65	0.82	7.78
CAL_VR28 - MG2	1.74	2.85	0.40	0.67	0.85	2.58
CAL_VR14 - MG1	0.94	0.01	0.58	0.69	0.77	9.60
CAL_VR14 - MG2	0.13	2.77	0.60	0.77	0.88	2.98
CAL_VR7 - MG1	1.08	3.23	0.13	0.61	0.77	9.22
CAL_VR4 - MG1	0.84	1.10	0.25	0.60	0.74	8.57
PRISM	0.00	0.00	1.00	1.00	1.00	2.92
Snow Water Equivalent (mm)						
CAL_VR28 - MG1	-27.4	43.3	0.34	0.51	0.66	6.24
CAL_VR28 - MG2	-22.0	-30.5	0.38	0.65	0.81	1.27
CAL_VR14 - MG1	26.3	18.9	0.28	0.50	0.63	12.31
CAL_VR14 - MG2	-3.53	15.2	0.57	0.69	0.84	1.96
CAL_VR7 - MG1	24.2	73.5	0.39	0.55	0.68	12.35
CAL_VR4 - MG1	19.2	16.0	0.31	0.53	0.67	11.80
SNSR	0.00	0.00	1.00	1.00	1.00	2.18
Snow Cover (%)						
CAL_VR28 - MG1	-0.52	-3.90	0.54	0.63	0.72	2.34
CAL_VR28 - MG2	3.40	-13.9	0.60	0.78	0.86	0.92
CAL_VR14 - MG1	11.4	-8.83	0.48	0.66	0.76	2.84
CAL_VR14 - MG2	5.50	-2.03	0.64	0.80	0.90	1.12
CAL_VR7 - MG1	9.38	-2.38	0.52	0.68	0.75	2.66
CAL_VR4 - MG1	9.52	-4.92	0.55	0.69	0.80	2.84
MODIS	0.00	0.00	1.00	1.00	1.00	1.18
Two-Meter Surface Temperature (K)						
CAL_VR28 - MG1	-2.31	0.47	0.86	0.89	0.92	
CAL_VR28 - MG2	-2.28	0.55	0.89	0.90	0.92	
CAL_VR14 - MG1	-3.32	0.24	0.89	0.92	0.94	
CAL_VR14 - MG2	-2.89	0.55	0.88	0.93	0.95	
CAL_VR7 - MG1	-3.57	0.27	0.91	0.94	0.96	
CAL_VR4 - MG1	-3.68	0.98	0.90	0.95	0.97	
PRISM	0.00	0.00	1.00	1.00	1.00	

Figures
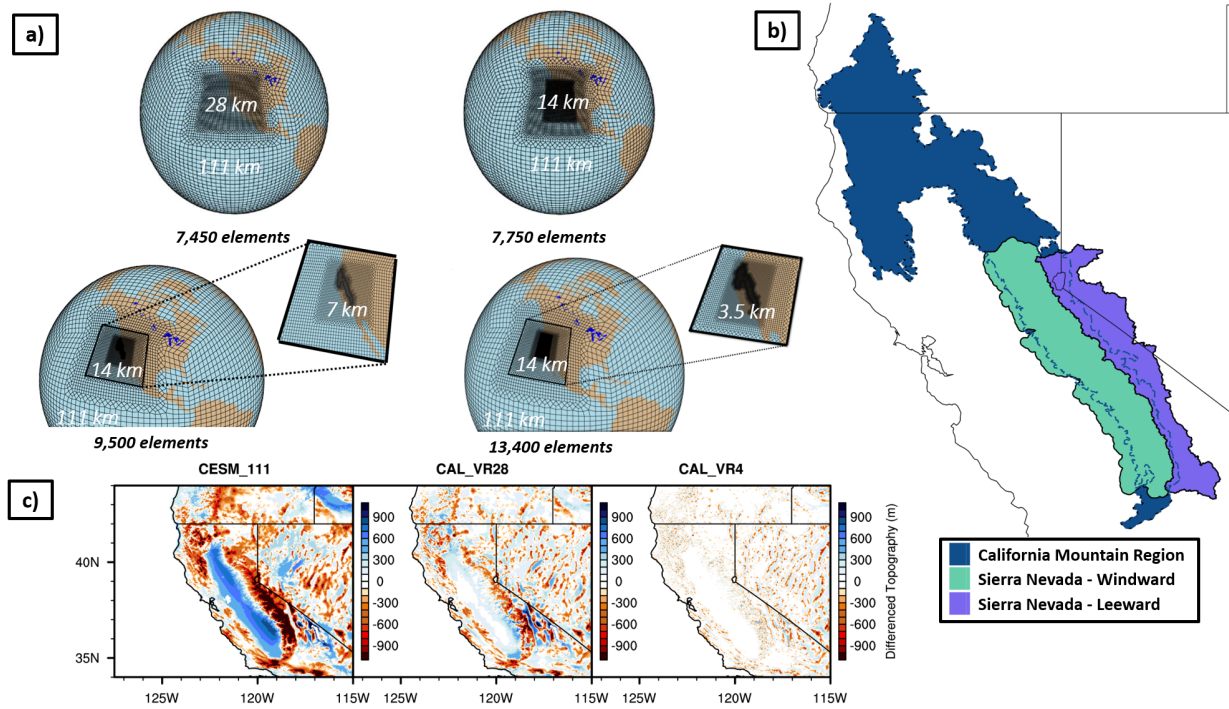
Figure 26: The VR-CESM grids used for this study utilized a quasi-uniform 111 km (1.00°) base-resolution cubed-sphere grid. In a), VR refinement is shown via the convex polygons with the highest grid resolutions focused over California's mountainous regions at 28 km (0.25°), 14 km (0.125°), 7 km (0.0625°) and 3.5 km (0.03125°). The three analysis regions for this study are depicted in b), with the California mountain region (focus of VR refinement) highlighted in dark blue and via a dashed dark blue line when overlapping with the other regions. Last, c) highlights the topographical difference between the USGS GTOPO 30 arc-second topography dataset over California, with a conventional 111 km (1.00°) global climate model topography shown for juxtaposition (CESM_111).
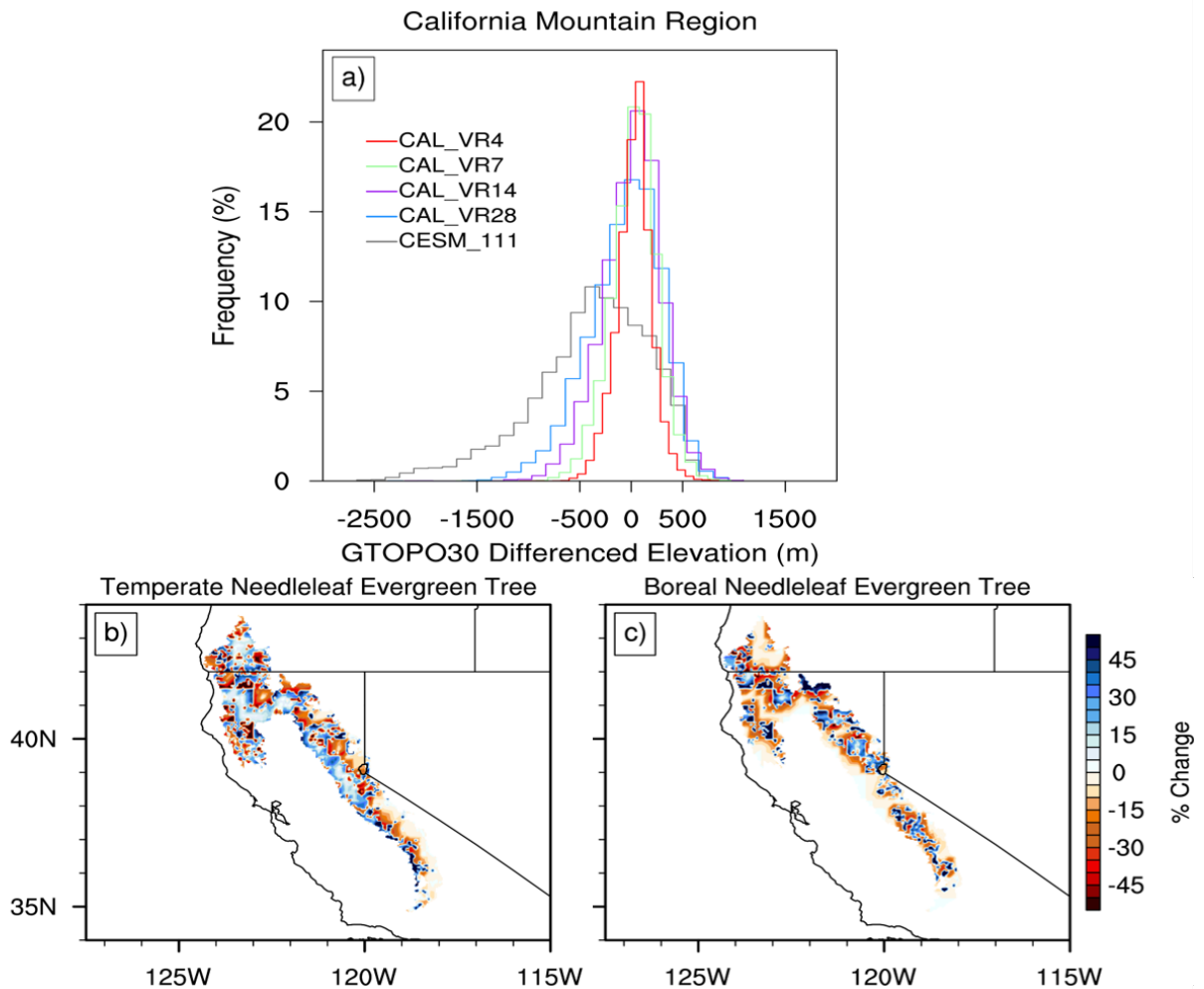
Figure 27: Surface characteristics in CAL_VR with (a) representing the difference in model surface topography over the California Mountainous Region compared to a DEM product (GTOPO30) and (b-c) showing differences in forest cover distributions between CAL_VR28 and CAL_VR4 for the two most abundant tree species in CLM4.0 within the static year 2000 three-minute surface dataset.
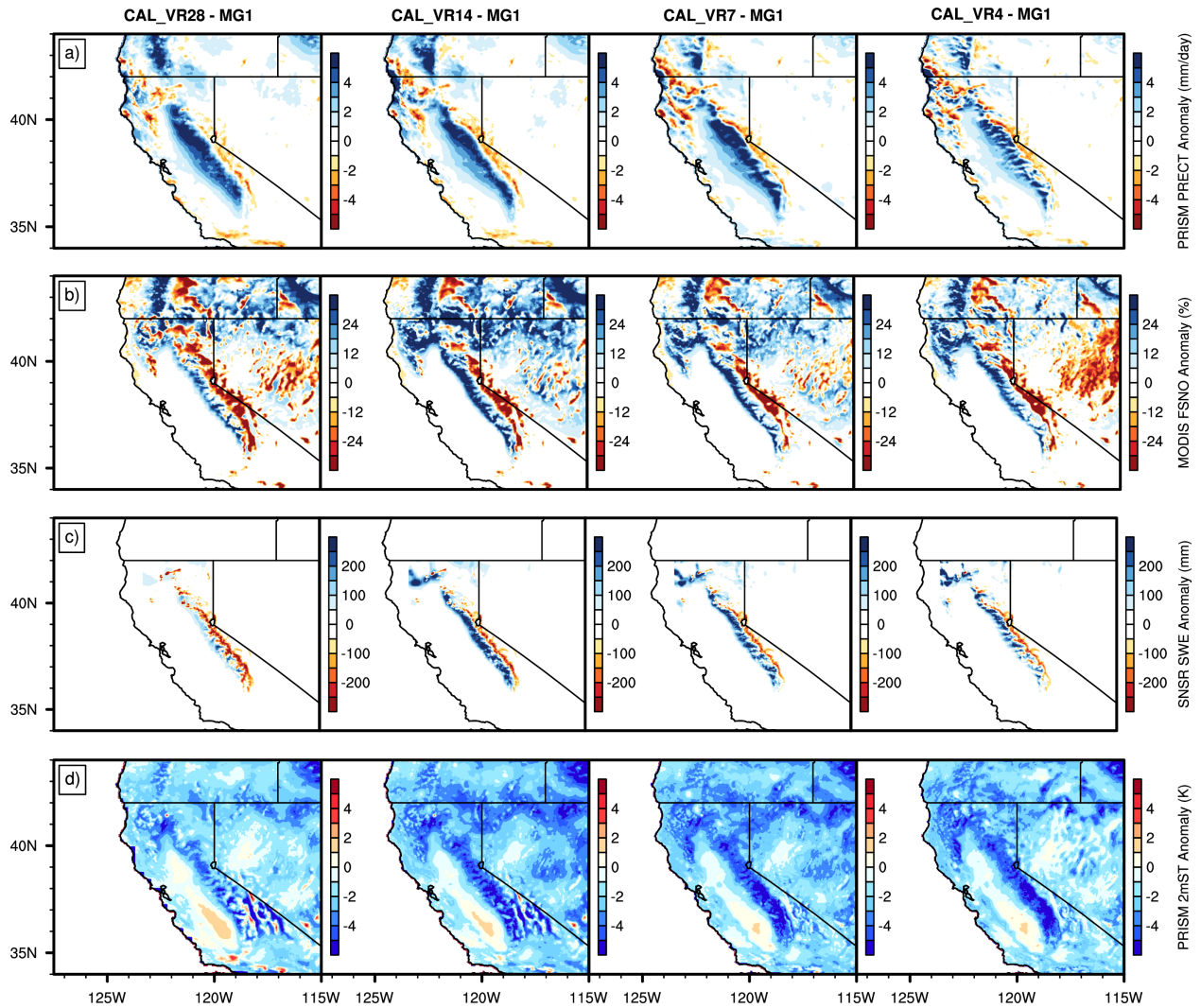
Figure 28: Effect of refined horizontal grid resolution in CAL_VR DJF spatial climate average differences a) total precipitation (PRECT) against PRISM; b) snow cover (FSNO) against MODIS; c) Snow water equivalent (SWE) against SNSR; d) two-meter surface temperature (2mST) against PRISM.
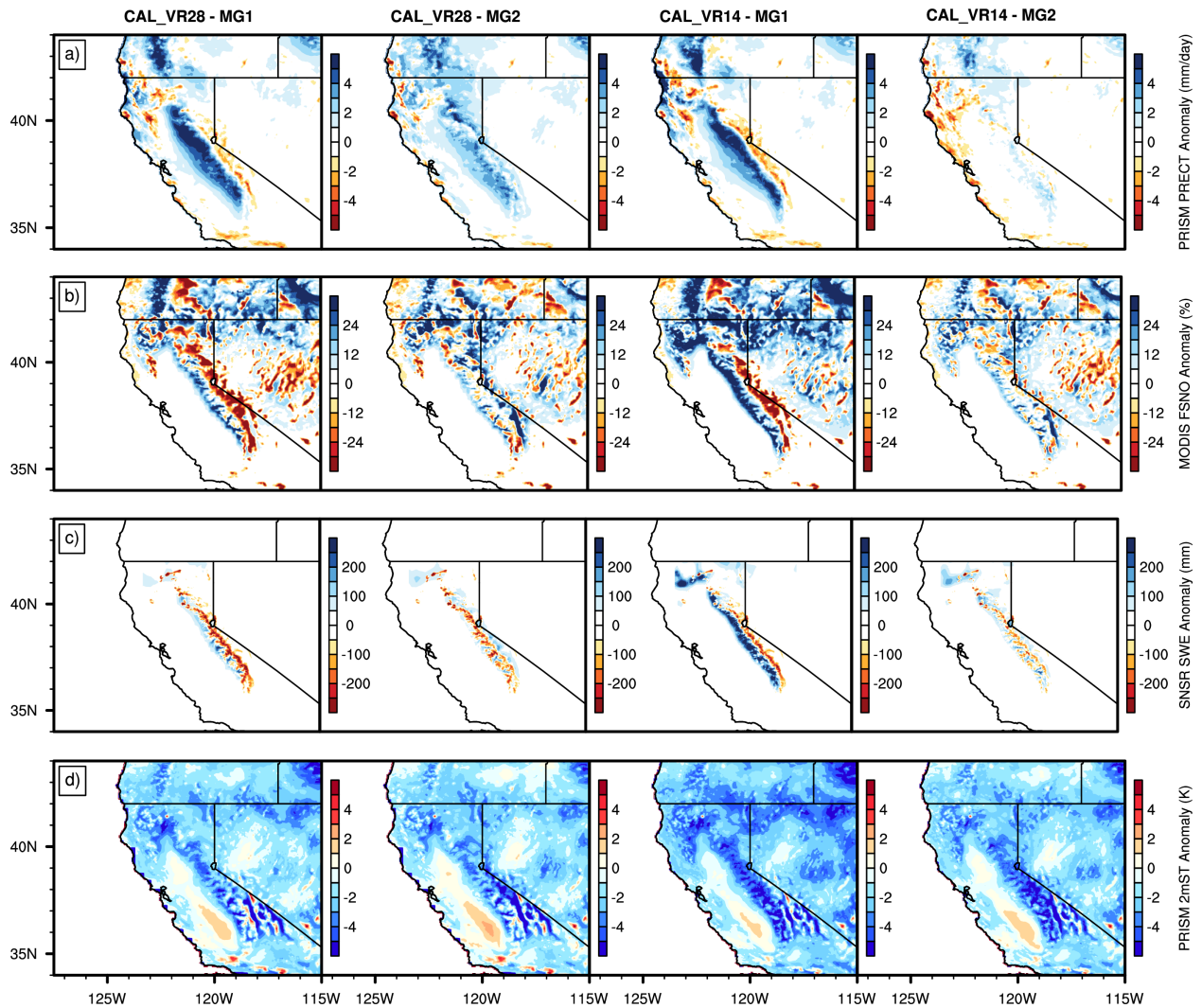
Figure 29: Effect of diagnostic (MG1) vs prognostic (MG2) microphysics CAL_VR DJF spatial climate average differences a) total precipitation (PRECT) against PRISM; b) snow cover (FSNO) against MODIS; c) Snow water equivalent (SWE) against SNSR; d) two-meter surface temperature (2mST) against PRISM.
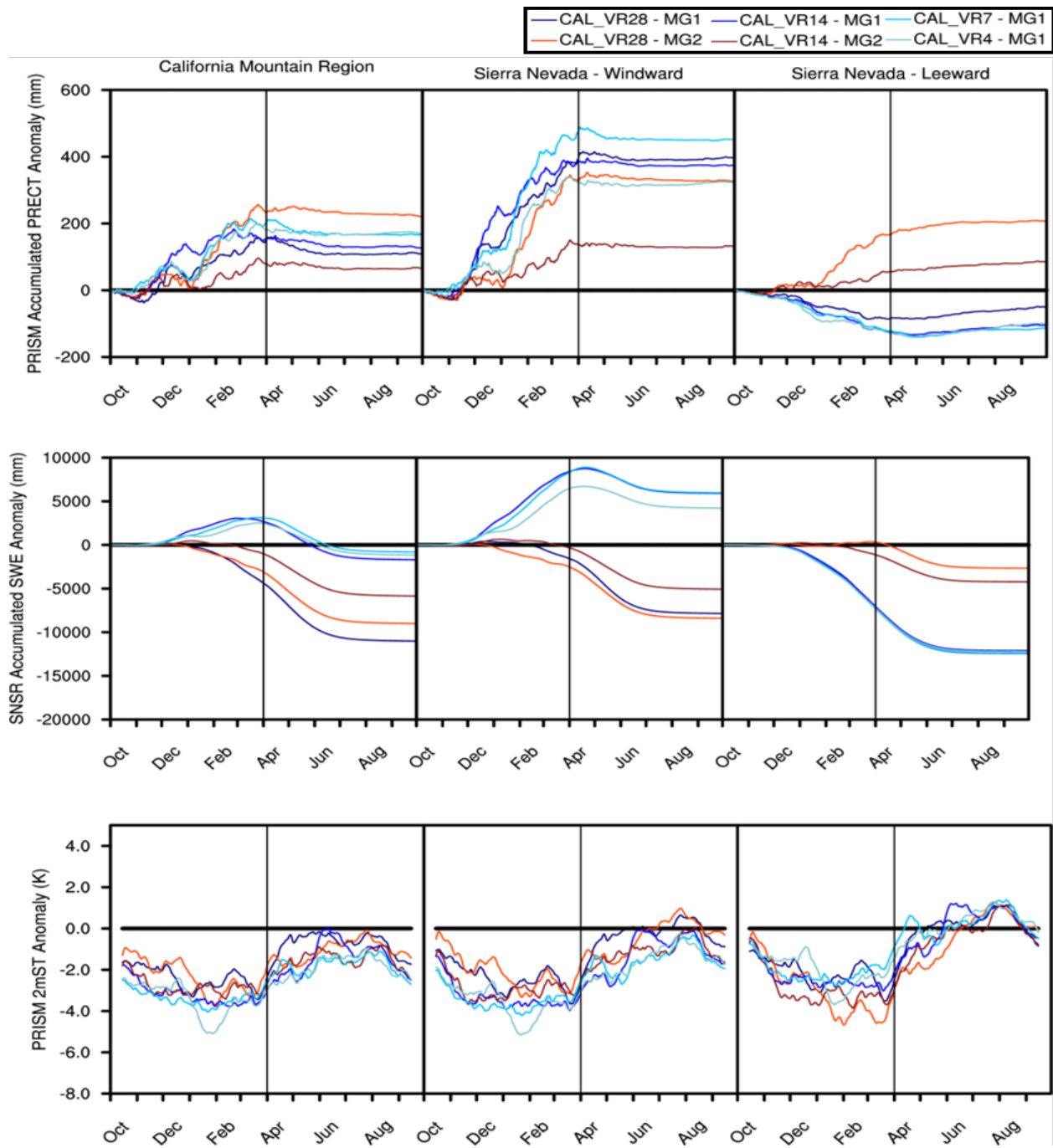
Figure 30: Water year daily climate average differences for the CAL_VR MG1 (blue) and CAL_VR MG2 (red) ensemble members compared to PRISM for total precipitation (PRECT) and surface temperature (2mST) and SNSR snow water equivalent (SWE) for the California Mountain Region (left column), windward side of the Sierra Nevada (center column), and leeward side of the Sierra Nevada (right column). A 30-day running average filter was applied to the 2mST fields for clarity. The vertical black line delineates the accumulation period from the melt period at the historical peak accumulation date of April 1st.
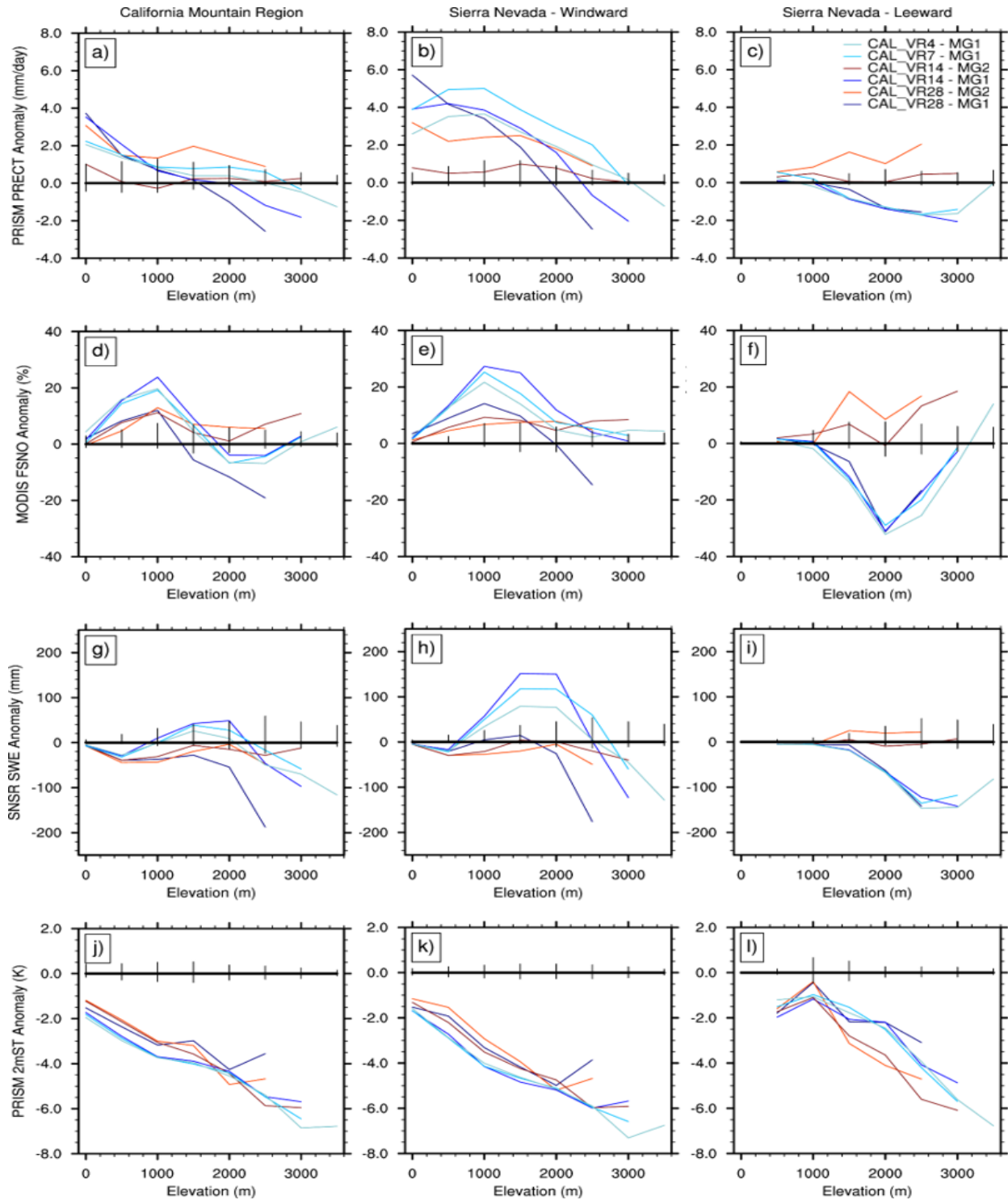
Figure 31: DJF climate average 500m elevational profile differences for CAL_VR MG1 (blue) and CAL_VR (red) ensemble members compared to PRISM for total precipitation (PRECT), surface temperature (2mST), SNSR snow water equivalent (SWE), and MODIS snow cover (FSNO) for the California Mountain Region (left column), windward side of the Sierra Nevada (center column), and leeward side of the Sierra Nevada (right column). Vertical black lines indicate the DJF seasonal spread in the comparative dataset at a given elevation interval.
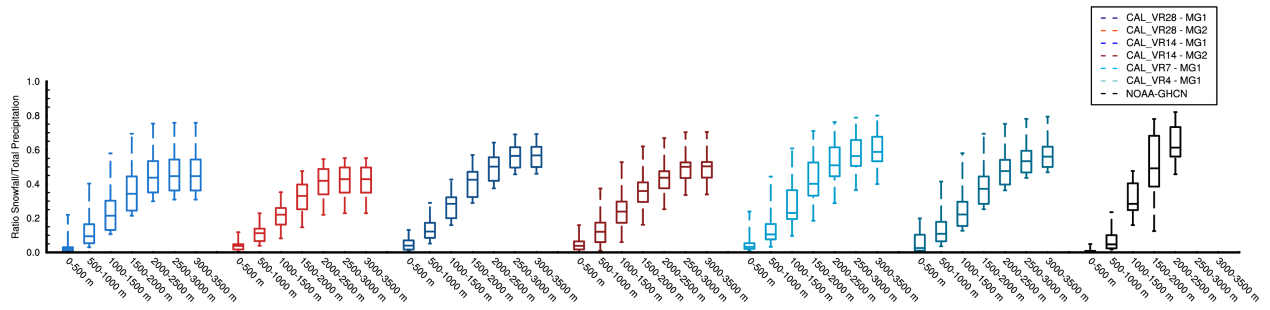
111

Figure 32: DJF climate average 500m snowfall (SNOWF) efficiences for the CAL_VR MG1 (blue) and CAL_VR MG2 (red) ensemble members compared with the NOAA-GHCN in-situ stations located on the windward side of the Sierra Nevada (black).

Conclusions

This dissertation presented three separate studies which utilized a recently developed global climate modeling technique, variable-resolution in the Community Earth System Model (VR-CESM), to understand the major processes that shape mountain hydroclimatology of the western US. Prior to this dissertation VR-CESM had only been utilized in idealized aquaplanet experiments and to understand large-scale atmosphere phenomena associated with Atlantic hurricanes. This work represents the next step in VR-CESM development with the implementation of realistic topography, the exploration of atmosphere-land interactions, and the investigation of climate change.

Chapter 1 presented the first exploratory VR-CESM simulations conducted with a range of topographic representations for the California Sierra Nevada. A gamut of model, observation, and reanalysis datasets associated with Sierra Nevada snowpack were collected and juxtaposed to the VR-CESM simulations. It was found that for around two times the computational cost of a standard Intergovernmental Panel on Climate Change global model, VR-CESM could provide vastly better snowpack statistics and more usable regional climate data associated with water resources. VR-CESM highlighted close agreement with comparative datasets at both seasonal and climatological time scales with total snow water equivalent (snow cover) within 7 mm (7%) of the expected value and interquartile ranges (i.e., interannual variability) well within expected ranges. Further, seasonal Pearson pattern correlations were high (0.68) considering the simulations were only constrained by observed sea surface temperatures. Interestingly, topographic representation, rather than a doubling of horizontal resolution, played more of a role in how well VR-CESM simulated the historical snowpack trends. VR-CESM did showcase biases associated with an early peak accumulation timing (one to two weeks earlier) and a higher spring snowmelt rate (complete melt 30 days too soon) compared with observed values, although these biases were not any worse than other downscaling strategies. Overall, VR-CESM was shown to be competitive with current regional downscaling techniques in representing Sierra Nevada snowpack, warranting its use for future analyses.

Chapter 2 utilized the best available VR-CESM case from Chapter 1, considering model cost and

performance, to simulate a "business-as-usual" (RCP8.5) climate change scenario across the five major mountain ranges of the western US. To contextualize VR-CESM's climate change signal, the three most widely used climate change datasets for the western US (i.e., CMIP5, BCSD-CMIP5, and NARCCAP) were juxtaposed against VR-CESM over a common mid-century timeslice of 2040-2065. It was found that snowpack tendencies in the global model simulations (CMIP5) are unusable for climate change analysis and VR-CESM highlighted a more pessimistic decline in average winter season snow water equivalent (-38%) compared with dynamical downscaling (-19%) and statistical downscaling (-26%) techniques by mid-century. Further analysis focused on an expanded 2025-2050 and 2075-2100 trend analysis to understand changes in winter season average, interannual variability, precipitation phase, and elevational dependencies. Overall, it was found that by 2025-2050 (2075-2100) winter season average snowfall would decline by 4% (30%), snow cover by 10% (44%), snow water equivalent by 25% (69%), and surface temperatures would increase by 1.3 °C (5.0 °C). By 2050, interannual variability highlighted a stark contrast to historical trends, with anomalously high winter season snowfall, snow cover, and snow water equivalent non-existent and anomalously high surface temperatures becoming the new normal. Total precipitation was found to increase by 7% (20%) by 2025-2050 (2075-2100), however a 4% (24%) decline in snow-to-rain ratios were also found. Surface temperatures showed a strong elevational dependency by 2025-2050 (2075-2100) of +0.97 °C (+2.35 °C) from 500 m to 1000 m and +2.85 °C (+7.01 °C) to +3.81 °C (+9.43 °C) from 1000 m to >3000 m. Overall, the nonlinear feedbacks that climate change imposes on mountain hydroclimate processes highlights the significant burden that water managers will face in the coming century to meet water demand. Adaptation strategies may need to deviate from historically plausible protocols in order to ensure the resiliency of western US economies.

Chapter 3 systematically explored the effects of changing model horizontal resolution (28 km, 14 km, 7 km, and 3.5 km) and sub-grid-scale parameterizations (28 km and 14 km with prognostic vs diagnostic microphysics) in representing historical hydroclimate trends in the California Sierra Nevada. It was found that increased refinement in model horizontal resolution to more accurately represent surface heterogeneity did not result in a more realistic mountain hydroclimatology when compared with observational and reanalysis datasets. In fact, bias tendencies were merely maintained and localized across the four members of the VR-CESM ensemble. A breakthrough in VR-CESM per-

formance was found when using a new prognostic microphysics parameterization coupled with an increased refinement in model horizontal resolution. The advantages of this new physics parameterization are attributed to its more realistic "memory" of hydrometeor concentrations between grid cells and insensitivity to orographic forcing on the windward region of mountains. This resulted in a substantially closer approximation of historical DJF climate average total precipitation (within 2%), snow cover (within 6%), and snow water equivalent (within 5%) when compared to mountain hydroclimate observational datasets. Additionally, the mountain windward/leeward distributions of these variables were nearly identical for DJF climate average total precipitation (3 to 1 ratio), snow cover (1 to 1 ratio), and snow water equivalent (2 to 1 ratio). Akin to Chapter 1, DJF seasonal average Pearson pattern correlations were high for total precipitation (0.77), snow cover (0.80), and snow water equivalent (0.69) when considering that the simulations were only constrained by observed sea surface temperatures. Of interest for future model development, a systemic cold bias in surface temperature was found across all six members of the VR-CESM ensemble and worsened with refinement in model horizontal resolution. The worsening of the surface temperature bias is likely due to lapse rate issues in mountainous environments within CESM. Potential culprits of the surface temperature cold bias were associated with boundary layer turbulence, snow-albedo feedback from the snow cover equation, elevation dependence of specific humidity concentrations, and/or cloud cover radiation feedbacks. Overall, the use of VR-CESM with a new microphysics scheme enhances its usability in properly representing the magnitude and distribution of precipitation and the life cycles of mountain snowpack. These two processes are crucial for data usability within the context of water resource management and dam operations, both of which are dependent on regional accuracy.

This dissertation helped to answer several key questions regarding the usability of VR-CESM as a global-to-regional hydroclimate tool, however there are many other questions yet to be answered. Four such questions are presented, however this is not an exhaustive list. First, VR-CESM has only been utilized in North America and should be explored in other midlatitude mountain regions (e.g., the South American Andes) to ensure model performance is robust. Second, the snowpack and surface temperature biases highlighted in Chapter 1 and 3 within VR-CESM need to be explored and constrained. A set of hypotheses were generated in Chapter 3 which suggest that a set of

experiments using standalone CAM and/or CLM could be utilized to isolate parameter sensitivities related to mountain lapse rates and/or snowpack. Particular focus should be applied at the regional to mountain range scale where CESM has not been extensively developed. Third, the character of precipitation in midlatitude regions has been elucidated in recent years and the effects of atmospheric rivers are apparent. VR-CESM offers a unique testbed to evaluate its ability to properly represent the counts, duration, intensity, and landfall locations of these crucial hydroclimate features. Fourth, VR-CESM is constrained by the hydrostatic approximation made in its dynamical core formulation. An evaluation of the effects of using a nonhydrostatic vs hydrostatic dynamical core within midlatitude mountain ranges should be further explored to ensure that hydroclimate variables are not adversely sensitive to this at scales below 10 km.

An ancillary benefit of this work was the formulation of a start-to-finish VR-CESM guide that explains how to generate the necessary datasets, implement the datasets within the CESM root directories, test the implemented datasets for numerical noise, and, finally, perform VR-CESM simulations that are able to answer scientifically relevant research questions. Prior to this work, there had not been a centralized document to expedite the learning curve of other users who wish to use this model technique. This document is now available upon request.

Appendix

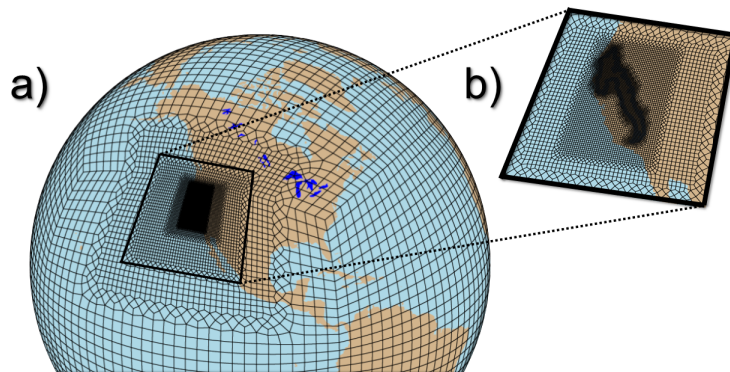**Community Earth System Model (CESM)**

Figure 33: An example of a recently constructed VR-CESM grid over complex terrain in California. The continuous refinement of the model grid resolution from left to right include a) 111km (1.00°) to 28km (0.25°) over the western USA and b) 28km (0.25°) to 4km (0.03°) over the Sierra Nevada and Klamath regions of northern California.

Variable-resolution capabilities are only available within a few modeling frameworks, one of which is the Community Earth-System Model (CESM), co-developed by the Department of Energy and the National Center for Atmospheric Research (Hurrell et al (2013)). CESM is a state-of-the-art Earth system model consisting of atmospheric, oceanic, land and cryospheric components, with options to include biogeochemical cycling, chemical tracer species, and whole-atmosphere simulations. The Community Atmosphere Model (CAM, the atmospheric component of CESM) is further broken into two components: the dynamical core (dycore) and the sub-grid-scale physics parameterization suite, which incorporates processes that occur on scales less than the model grid scale (e.g., clouds and land-surface processes). Generally, dycores can be thought of as numerical solvers for the continuity, mass (tracer and dry air), momentum, and thermodynamic equations, and the equation of state, (adiabatic processes) and sub-grid-scale parameterizations update the dycore solutions to incorporate important processes such as localized heating from tracer forcings and latent heat release (diabatic heating). The dycore utilizes different numerical discretization methods that aim to balance computational burden with model accuracy. This adiabatic and diabatic solution is then updated to be energetically conserved and physically consistent (i.e., no non-physical solutions such

as negative mass) within each model grid column via fixers and filters. The result of all of this is a projected time tendency of a model variable of interest (e.g., temperature). In CESM, CAM has several dycores available for use including finite-volume, semi-Lagrangian, Eulerian and spectral element (SE), with work underway for the inclusion of others in the near future. Of these four, only one dycore has variable-resolution capability, namely CAM-SE. An example of a VR-CESM grid generated to explore the mountain hydroclimatology of the California Sierra Nevada is highlighted in Figure 33.

The SE dycore method has several important properties including parallel scalability, flexibility and accuracy, that make it a desirable choice for modeling atmospheric dynamics. The SE dycore (Fournier et al (2004); Taylor and Fournier (2010)) is now default in CAM and is therefore a supported platform for scientific research. More recently, variable-resolution support has been added to CESM's CAM, the land-surface model (Community Land Model (CLM)), and within the remapping tools used to generate initial and boundary conditions (e.g., topography, land-surface cover, soil profile, sea-surface temperature and sea-ice datasets). Thus, the variable-resolution CESM-SE framework (VR-CESM) now allows for coupled atmosphere-land-prescribed ocean climate simulations (i.e., CESM's scientifically validated component set, F_AMIP_CAM5, used for the Atmospheric Model Intercomparison Project (AMIP)).

A unique problem in variable-resolution models is how to best refine from a globally uniform-resolution (e.g., 111km) to a regionally refined resolution (e.g., <28km). In order to accomplish this feat, a unique model grid generator must be employed. Fortunately, effort has been made in constructing said software. One example is the Spherical Quadrilateral Mesh Generator (SQuad-Gen) software suite developed by Dr. Paul Ullrich (Ullrich, 2014). SQuadGen first employs a cubed-sphere base mesh over the globe at a desired resolution (e.g., 111km) and then provides smooth grid transition regions via quadrilateral shapes and spring-dynamics over user specified regions of interest. Thus, grids generated using this technique have several advantageous properties including greater uniformity in grid refinement regions and grid cells that more readily approach 90 degree angles (Guba et al, 2014). This transition region is generated as smoothly as possible between one resolution and another via spring dynamics, but this process still creates irregularly

shaped grid cells. These irregularly shaped grid cells complicate how to best solve the computed dynamical core fluxes, both meridionally and zonally, which could impact the numerical stability and kinetic energy spectrum (Dennis et al, 2012; Guba et al, 2014; Zarzycki et al, 2015).

To address this a fourth-order hyperviscosity diffusion operator is applied and implicitly scaled to each grid box resolution. Higher (lower) values are used in larger (smaller) grid boxes to ensure that proper dampening of coarser resolution fields occur without undermining resolved dynamics in the finer resolution fields. Hyperviscosity is critical in dampening sub-grid-scale modes that may act to generate numerical instabilities (e.g., sound waves), while ensuring that large-scale modes, resolved at the grid-scale, are left relatively unimpacted (Guba et al, 2014). To formulate the appropriate hyperviscosity dampening, three techniques are currently available. These include constant-coefficient, scalar, and tensor. Each of the techniques employ a matrix determinant solver on the spectral element basis vectors in spherical coordinates (Guba et al, 2014). For variable-resolution CESM, the tensor hyperviscosity technique is used which is dependent on the local element horizontal length scales and, unlike the constant-coefficient technique, ensures that proper resolution scaling occurs regardless of horizontal irregularities in grid box lengths (Guba et al, 2014).

The adoption of variable-resolution within the global atmospheric modeling community is fairly recent, although several major modeling centers are currently pushing this capability to operational global climate models (Skamarock et al, 2012; Harris and Lin, 2013; Zarzycki et al, 2014a; McCorquodale et al, 2014). Variable-resolution grid refinement has been demonstrated to be effective for operational modeling of tropical cyclones Zarzycki et al (2014a); Zarzycki and Jablonowski (2014); Zarzycki et al (2014a, 2015), large-scale weather systems Rauscher and Ringler (2014) and regional climate Rauscher et al (2013); Zarzycki et al (2014b); Rhoades et al (2016); Huang et al (2016).

Sub-Grid-Scale Parameterizations

In CESM, unresolved grid-scale processes (or sub-grid-scale parameterizations) enter the CAM equation sets via four extension variables within the mass conservation equation, tracer transport

equation (one for each species), horizontal momentum equation, and the thermodynamic equation. Of note, the vertical momentum equation isn't explicitly represented and prognosed in CAM as the dynamical core was developed under the hydrostatic assumption (i.e., via scale analysis, the GCM grid horizontal length scale is much larger than the vertical and consequently can be explicitly ignored). Thus, the four extension variables include the drag parameter (F) for convection, turbulence and gravity waves in the horizontal momentum equation; the diabatic heating parameter (H) for radiation, convection, microphysics, turbulence, and gravity waves in the thermodynamic equation; the tracer source-sink parameter (S) for phase changes (evaporation and condensation) in water vapor in the mass tracer equation; and lastly, the mass fixer parameter (M) for air mass water vapor content in the mass conservation equation (Neale et al, 2010). In CAM5, time-splitting techniques are used to sequentially couple the sub-grid-scale parameterizations to the dynamical core equation set solvers. This means that the dynamical equations are solved first and then the sub-grid-scale parameterizations are solved, in this order: surface fluxes, boundary layer, shallow convection, deep convection, macrophysics, microphysics (which are updated by aerosol distributions and the surface models) and lastly, radiation processes. When all are accounted for, 90% of the computational workload in CESM is used in solving the radiation and dynamics equation sets (Neale et al, 2010).

The effort of this technical report is to identify several of the crucial sub-grid-scale parameterizations employed to understand modeled hydroclimatology in regions of complex terrain, with a particular focus on VR-CESM. These topics will include: cloud processes (macro- and micro-scale), convection, radiation, sub-grid-scale topography and drag, and land-surface processes (e.g., snow processes).

Cloud Processes and Precipitation

Cloud formation occurs via four main processes: convection, orographic uplift, frontal convergence and convergence of air. As such, these main processes are also largely responsible for dictating where precipitation will and will not occur. Additionally, the contents of the cloud can often dictate radiative properties and if precipitation will occur. For example, clouds with large quantities of ice have been associated with a higher likelihood to produce precipitation, especially intense precipitation that is not drizzle (Morrison and Gettelman, 2008). Ice particles act as seeds for

cloud droplet growth which abates part of the droplet size gap that must be overcome to lead to precipitation. Unfortunately, cloud processes act at much more refined spatial scales than current climate models can explicitly resolve and the non-linearities of internal cloud processes (i.e., formation, species distributions, and phase transitions) in varying amounts of cloud water amount are non-negligible. Thus, sub-grid-scale cloud characterization in climate models is a source of continual development. In Hurrell et al (2009), 12 of the 32 sources of largest uncertainty (i.e., root-mean squared error) in climate models were directly associated with cloud processes, with links to several indirect feedbacks as well. With this in mind, climate researchers have devoted a large amount of research time in how to best characterize various cloud properties at the sub-grid-scale in a way in which to encapsulate the complexities associated with phase change, critical relative humidity thresholds, horizontal extent, and vertical development and overlap. In VR-CESM these critical parameterizations are dictated in large part by the CAM5 microphysics and macrophysics.

The microphysics sub-grid-scale parameterization in CAM5 was developed by Morrison and Gettelman (2008). Microphysics is a broad term that describes how CAM5 characterizes clouds condensed phase water processes such as the species' (liquid and ice) size distributions, functional shapes, and conversion rates. CAM5 relies on the concept of "bulk" schemes where cloud liquid and ice size distributions are assumed to take a continuous functional form (Morrison and Gettelman, 2008). To enhance the usual GCM approach and leverage techniques that have shown promise in cloud-resolving and regional scale models the Morrison and Gettelman (2008) scheme in CAM5 predicts two-moments of the distribution (i.e., cloud mixing ratio (q) and cloud number concentration (N)). By characterizing these two quantities, the volumetric size distributions of liquid water and ice species (i.e., effective radius) develop in a more realistic way and interactions between clouds and aerosols are more robust (Morrison and Gettelman, 2008). To determine the time evolution of cloud mixing ratio and cloud number concentration (with liquid and ice solved separately), grid scale quantities such as advection, detrainment, turbulence, and sub-grid-scale microphysical processes including accretion (growth), nucleation (catalyzed growth), evaporation/freezing/melting/sublimation (phase change), and autoconversion to rain/snow (deposition) are computed (Morrison and Gettelman, 2008). As stated earlier, cloud water amount and variability plays a crucial role in dictating the evolution and lifetime of a given cloud. In GCMs, the

grid cell is far too large to provide realistic variability over the spatial scales that clouds act on. Thus, to provide appropriate spatial heterogeneity a probability density function (PDF) with a gamma distribution is constructed and considered for cloud water, presently not for cloud ice due to observational ambiguities (Neale et al, 2010). The gamma distribution approach in CAM5 was derived from optical depth observations of marine boundary layers clouds, providing some empirical backing, and is assumed to be applicable to all modeled stratiform clouds. The efficacy of using this distribution for non-boundary layer clouds is uncertain and clearly stated by the authors (Morrison and Gettelman, 2008).

Cloud water (cloud ice) conversion to rain (snow) in CAM5 are determined by the interplay between all of the aforementioned processes. For cloud water to rain, direct autoconversion is dictated by first solving for the gamma PDF for in-cloud water by calculating the relative variance and mean in-cloud mixing ratio. Once the in-cloud water PDF is determined, the amount of water available can now be used (and integrated over) to calculate how much would be available for conversion into rain. Additionally, cloud fraction must be calculated to ensure that sub-grid variability in cloud/no-cloud is maintained (this is determined by the macrophysics, described below). The product of the cloud water integration (under the gamma PDF), cloud fraction, and the product of perturbations in cloud mixing ratio and cloud number concentration, all scaled with various constants derived from empirical evidence, determines the autoconversion and accretion rates (Morrison and Gettelman, 2008). As discussed previously, cloud ice autoconversion to snow isn't assumed to follow a gamma distribution, largely due to a lack of observational studies; thus, cloud ice-mass and number-weighted size distributions (with associated threshold sizes and conversion time scales) of cloud ice mixing ratios and number concentrations are computed (Morrison and Gettelman, 2008). In CAM5, threshold size between cloud ice and snow is set at 200 micrometers with autoconversion time scales set at three minutes and collection efficiencies of cloud ice into falling snow at 10%. For autoconversion in cloud ice mixing ratios, the product of cloud fraction, number- and mass-weighted size distributions (determined by the aforementioned size thresholds and conversion rates), and an exponential attenuation parameter. The size distributions are determined by the following thresholds: minimum (maximum) mean diameter of cloud water is asumed to be two (50) micrometers, cloud ice to be 10 (400) micrometers, rain to be 20 (500) micrometers, and snow 10

(2000) micrometers. Lastly, for simplicity, cloud ice (snow) is assumed to melt instantly at $0°$ $(2°)$ Celsius. Overall, precipitation in CAM5 is ensured to be in vertical balance, both energetically and from a mass standpoint. This is important to consider since cloud mixing ratio and number concentration are determined separately and thus can potentially lead to error in conservation. This however may lead to potential sensitivities to time step, but errors can be minimized by appropriate sub-stepping (Neale et al, 2010). As shown in (Park et al, 2014a), CAM5 has a general positive bias in global annual-mean total precipitation at the surface with a value (3.01 mm/day) 12-15% larger than satellite derived measurements (although these observations are suggested to be low biased). From a mountain centric viewpoint, CAM5 has shown too strong of precipitation in the Himalayas (especially in summer), the Andes (especially in winter), and in the Rockies when run at $1.9°$ lat by $2.5°$ lon resolution and a physics time-step of 1800 seconds (30 minutes) (Park et al, 2014a). With the advent of variable-resolution capabilities, testing of these mountain precipitation biases at higher-resolution is currently underway.

Macrophysics schemes in GCMs are used to describe sub-grid-scale cloud fraction in each model vertical layer, the overlap (both horizontally and vertically) of clouds, and, lastly, the rate at which water vapor is converted from vapor into liquid and ice (Neale et al, 2010). As described in Morrison and Gettelman (2008), microphysics has a strong physical backing; however, macrophysics is associated with the largest uncertainty in GCMs. This is largely a result of the need to work seamlessly across a multitude of horizontal resolutions that modelers demand and still maintain radiative/mass balance. CAM5 utilizes the Park and Bretherton (2009); Park et al (2014a) schemes and has been developed to produce cumulus (both deep and shallow), stratus, and total cloud (cumulus plus stratus) sub-grid-scale cloud properties. The difference between stratus and cumulus clouds have to do broadly with their shapes and turbulent nature. Stratus clouds are often dominated by horizontal development with symmetric turbulence in the horizontal/vertical velocities, cloud extents, and saturation properties; whereas, cumulus clouds are dominated by vertical development and assymetric turbulence in which vertical development is narrow, strong, and saturated and the descending subsidence is weakly diffuse and unsaturated (Neale et al, 2010). These important processes (and their fractional behavior) are empirically derived.

In CAM5, deep cumulus is represented by a log equation imposed on the product of an empirically derived constant (675) and the uprdaft mass flux, with an adjustable scaling parameter. This parameterization derives from the assumption that given a group of thermodynamic properties from source air derived from the grid-mean a deep convective updraft plume can rise to neutral buoyancy and be laterally entrained (10^{-3} m) when CAPE is larger than 70 J/kg (Park et al, 2014a). Since this equation was derived from the assumption that cumulus/stratus clouds act in a continuum, an overestimation is implied and therefore a limit is imposed on this equation to provide fractional areas ranging from zero to a maximum of 60% in the grid cell (Neale et al, 2010). Additionally, the constants used in the equation are assumed to have variability based on resolution, the continuum assumption, and therefore assumed to be adjustable to ensure that reasonable regional/global radiation budgets and grid-mean liquid/ice water contents are maintained (Neale et al, 2010). Shallow cumulus fraction solves for both vertical velocity and mass flux within the updraft of the cumulus (Park et al, 2014a). The parameterization aims to exemplify a plume of air which rises from the PBL top and is laterally entrained, with entrainment rates inversely proportional to the geometric height of the plume (Park et al, 2014a). The equation that describes this process constitutes a product of the mass flux, density of air, and vertical velocity of the cumulus updraft, multiplied by a constant (2) to account for two bouyancy processes (i.e., negative and positive saturated buoyancy updrafts) (Neale et al, 2010). Akin to the deep cumulus fraction, a continuum between liquid and ice is assumed, therefore a self imposed constraint is used. This constraint assumes that the fraction of the cloud can span zero to 20 percent of the grid cell (Neale et al, 2010). The stratus cloud macrophysics are separated into liquid and ice fractions by using grid-mean relative humidity for water and grid-mean relative humidity for ice. Liquid fraction is assumed to follow a triangular PDF where four RH conditionals (lower limit, bi-modal peak locations, and upper limit) are set to ensure that even given a limited sample set of data a PDF can be derived (Park et al, 2014a). The half-width of the triangular PDF must be scale aware to account for any GCM grid size and the sub-grid variability associated with this, therefore it should be computed internally and not explicitly set externally. However, in CAM5 tuning parameters for critical relative humidities (cRH) are set that are sensitive to model vertical level of the updraft plumes and the land-surface properties of the grid cell. Thus, for layers below 700 hPa a cRH is set to 0.89, and interestingly for western USA hydroclimate interests, to 0.79 if snow water equivalent is less

124

than 10^{-6} m (the CAM5 developers self-describe this as a crude representation of a rough surface in the lower troposphere), and 0.80 in layers above 400 hPa, with linear interpolation between the two cRH pressure levels (Park et al, 2014a). Therefore, although simplified from reality, these cRH values set the context of when cloud fraction in the grid-cell can begin to develop and provide the spatial heterogeneity observed in nature spanning 20 km to 200 km (usual GCM grid-cell sizes) without using an overly strict constraint of a necessary RH threshold of 100% in the grid-cell mean (Quaas, 2012). With that being said, a necessary condition for cloud water to form is for RH to be 100% and liquid water can not exist outside the liquid stratus cloud region (also known collectively as the saturation equilibrium) (Park et al, 2014a). Ice stratus cloud fraction doesn't use a triangular PDF, but rather a quadratic function of grid-mean total ice RH dependent on the grid-mean total ice specific humidity divided by saturation specific humidity of ice minus the cRH of ice stratus all over the difference between supersaturation (set at 1.1) minus cRH of ice stratus (Neale et al, 2010). Unlike liquid stratus, ice stratus cRH is set to 0.8 regardless of vertical level of the updraft plumes or land-surface properties, largely due to lack of observational data.

The last of the critical sub-grid scale determinants from macrophysics is the cloud overlap (both horizontal and vertical). As described previously, four independent cloud fractions are possible (deep/shallow cumulus and liquid/ice stratus). The distribution of these cloud fractions play a pivotal role in determining the radiative interactions throughout the vertical column of the model, how the Bergeron conversion process from vapor to liquid to ice occurs and inevitably the precipitation tendencies of the GCM. Therefore, careful consideration must be used. For CAM5, horizontal overlap is determined by seven main assumptions. These are: shallow cumulus can account for up to 20% of the cloud fraction, deep cumulus can account for up to 60% of the cloud fraction and total cumulus can only account for up to 80% of the grid cell cloud fraction; shallow cumulus and deep cumulus can't overlap, whereas liquid/ice stratus are maximally overlapped and uniformly distributed; liquid and ice stratus can take up to 100% of the grid cell fraction, but only fill the non-cumulus portion within each grid layer; and, lastly, to ensure conservation of total cloud fraction, all cloud fractions must sum to less than or equal to 100% of the grid cell (Park et al, 2014a). Within a given vertical layer, CAM5 assumes that maximum overlap occurs in stratus cloud fraction and that the radiation scheme only interacts with one total cloud fraction value,

assumes horizontally homogeneous water/ice totals, and uses a maximum-vertical overlap of cloud fraction to calculate radiative heating rates and profiles (Park et al, 2014a).

Convection

Convection in CAM is split into two main categories, shallow and deep. Shallow convection dictates how vertical transport of heat, momentum, moisture, and tracers will occur under asymmetric turbulence. The shallow convection scheme (UWShCu) in CAM5 was developed by Park and Bretherton (2009) with several assumptions including a steady state convective updraft plume with a small fractional area and a corollary subsidence within the same grid cell. This scheme has undergone extensive single-column testing and refinement in CAM5. The UWShCu shallow convection (along with the moist turbulence parameterization) is responsible for eight different sub-grid-cell processes in CAM5 that dictate the evolution of cumulus cloud formation and demise. These proccesses include building the mean state profiles; creating the cloud condensation bins; characterizing updraft plumes at the top of the planetary boundary layer (PBL); calculating the convective inhibitions and turbulent kinetic energy for cloud base mass fluxes and updraft velocities; constructing the buoyancy and entrainment characteristics of a plume between the PBL and cloud top; identifying entrainment near the cloud top; producing convective fluxes in the PBL; ensuring conservation of grid-mean tendencies in scalars; and, lastly, computing the tendencies of non-conserved scalars (Neale et al, 2010). To compute the eight shallow convection processes seven state variables are required. These include the grid mean tendencies in water vapor, liquid water, ice, temperature, horizontal winds (u and v), and the mass/aerosol count. With these state variables, the shallow convection scheme computes the condensate potential temperature and the total specific humidity with both assumed to be either nearly or completely conserved. The profiles for both quantities are then computed to conserve the mean state in each vertical layer, but discontinuities may occur at model interfaces. Lastly, the profiles are used to compute the virtual potential temperature. In summary, as described in Park and Bretherton (2009), the UWShCu parameterization is a mass-flux scheme where entrainment and detrainment are computed via a buoyancy sorting algorithm and triggered/closed by convective inhibition.

Deep convection in CAM5 was developed mainly using the Zhang and McFarlane (1995) scheme.

The overall role of deep convection is to dictate the evolution of an ensemble of convective plume updraft/downdraft when the atmosphere is conditionally unstable in the lower layers of the model atmosphere with sufficient convective available potential energy (CAPE). As convection occurs, CAPE is assumed to be destroyed at an exponential rate with a specified adjustment time scale Zhang and McFarlane (1995).

Albeit, critically important for tropical precipitation trends, convection isn't a dominant driver in western USA mountain hydroclimatology (especially in winter). Therefore, the model assumptions made in the macro- and micro-physics coupled with the efficacy of the large-scale climate drivers are the dominant drivers of regional precipitation. These include the location and magnitude of the Rossby Wave tracks, the positive/negative phase of geopotential height anomalies, topographical resolution, orographic uplift, and SST anomalies.

Sub-Grid-Scale Topography

Topography representation in climate models is crucial in resolving key hydroclimatic variables. Orographic uplift plays a pivotal role in forcing air masses to quickly ascend the adiabatic lapse rate, resulting in a faster means to precipitation, and the maintenance of freezing to subfreezing temperatures through extended periods of the year. This is especially important for temperature dependent quantities such as snowfall and snowpack accumulation/melt. Unfortunately for most of today's global climate models topography is much more smoothed than reality. This smoothing is a function of the coarse (111km) model grids that arise due to restraints in computational cost and maintaining numerical stability in terrain following vertical coordinate systems, like the ones implemented in CESM. Thus, the peaks, valleys, and slope irregularities of realistic topography is often neglected. To try and alleviate this, sub-grid-scale topography is implemented to ensure that some semblance of the fractal nature of topographic reality is maintained in climate model's resolved topography. This is important in representing surface frictional drag, orographic uplift, and vertical moisture and momentum transport/profiles.

In CAM5, surface stress is implicitly represented in the lowest model layer to ensure that the whole system's horizontal momentum is conserved, surface winds don't act non-physically and numerical

instabilities don't arise (often supplemented by smoothing of the lower boundary topography). To calculate the surface stress coefficient for a given timestep, the normal drag coefficient is added to the turbulent mountain stress drag coefficient (a variable specific to only the atmospheric model). The normal drag coefficient is derived from the lower layer winds and the turbulent mountain stress coefficient is derived from the sub-grid distribution of surface topography. Additionally, a portion of the residual accumulated stress (stored for up to two model hours) is partitioned into the lower model layer, which changes the surface winds. Lastly, the winds at the lowest model layers are computed for the next time step. The overall effect of this drag coefficient is to dampen winds at the lower boundary of the climate model (creating vertical shear) as well as vertically propagate energy/moisture.

An additional sub-grid-scale parameter that is related to the sub-grid-scale topography in CAM5 is the representation of gravity wave drag. Gravity waves arise due to heterogeneous surface boundaries (i.e., topography) that create internal heating (friction) and wind shear resulting in the vertical propagation of momentum and energy from source regions (mountains) to higher levels in the atmosphere and/or downstream of the disturbance resulting in a non-negligible modification to the large-scale flow of the atmosphere (Neale et al, 2010). In fact, as described in (McFarlane, 1987) GCMs used to have inherent Northern Hemispheric wintertime circulation biases due to the inadequate representation of geopotential height fields and orographic forcing (i.e., gravity wave dissipation) which would impact the efficacy of medium-range forecasts. The gravity wave drag functions in CAM5 are derived from the hydrostatic momentum, continuity, and thermodynamic equations with assumed exponential wave solutions that rely on the Reynolds stress, Brunt-Vaisalla frequency, scale height, horizontal wavenumber and phase speed to compute the WentzelKramers-Brillouin (WKB) solution (Neale et al, 2010). This allows for the approximation of dynamical processes such as the saturation condition (wave breaking), diffusive damping (molecular diffusion or radiative cooling), and dissipation transport and/or heating from wave breaking (Neale et al, 2010). Of particular interest to mountain hydroclimate research, the orographic source function in CAM5 is derived from McFarlane (1987). This orographic specific disturbance (known as tau) is calculated by first sampling the sub-grid-scale standard deviation in orography to determine the average mountain height which in turn determines the maximal upper bound of the streamline

displacement that may occur (Neale et al, 2010). Once this value is determined, then the product of this term and the vertical averages for local air density, Brunt-Vaisalla frequency, and horizontal wind speeds are used to compute the streamlines of wave propagation/dissipation (Neale et al, 2010).

Another method in which to embed topographic influences into climate models are via sub-grid-scale topography parameterizations, such as the LG method (Leung and Ghan, 1998; Ghan et al, 2002; Qian et al, 2010). This climate model parameterization uses a 1km elevation dataset (GLOBE) to group the planet into 11 elevation classes, assessed and partitioned individually for each model grid cell. The elevation class bins are: -500, -1, 200, 400, 700, 1000, 1500, 2000, 3000, 4000, 5000, 7000, and 9000 meters, with less elevation classes needed as topography is explicitly resolved at the grid cell level (decreasing computational burden). The LG method works by using a combination of statistical representation of sub-grid variations in surface elevation and a simple airflow model employed only in regions of complex terrain. The airflow model assesses the rise/descent of an air parcel interacting with each elevation class and diagnoses the vertical temperature and humidity profiles (using the grid cell mean values). According to Leung and Ghan (1998), there are only two precipitation tuning parameters in the LG method, Tau (orographic forcing timescale related to the lifting/descent of an air parcel) which is usually tuned to 10 hrs for climate simulations based on sensitivity analyses in regional climate model (RCM) studies and Frc (the critical Froude number related to the mountain height (non-dimensionalized)). Overall, the LG method's updated state doesn't directly influence the model physics for clouds and/or precipitation, but does become a forcing term in the prognostic conservation equations for temperature and humidity for each elevation class. The result of implementing this sub-grid-scale parameterization into CAM has resulted in a clear upgrade in terms of mountain snowpack in the western USA with CAM replicating similar winter season (DJF) spatial distributions of precipitation and mountain snowpack as a widely used RCM, WRF, and vastly better characterizations compared to the non-LG method version of CAM, which characterized merely 3% of the observed SWE value (Ghan et al, 2002; Qian et al, 2010). Although a huge upgrade was seen with the LG method, the sub-grid scheme underestimations were on the order of 2-5 in the Sierra Nevada, Wasatch, and Rockies and overestimated by a factor of 2-5 in eastern Oregon and lee side of the Sierra Nevada (Qian et al, 2010). The excessive snow

was likely due to excessive precipitation, a cold bias associated with inadequate representation of lee side rain shadows (especially in coastal and narrow/perpendicular mountain ranges) and no account of the influence of mountain range orientation's modification to model wind directions(Ghan et al, 2002; Qian et al, 2010).

Radiation

The interactions between CAM5 cloud distributions and radiative transfer are integral in determining the surface energy budgets within CESM (and represent the bulk of the computational cost of a GCM). As described earlier, clouds are assumed to take the form of either liquid, ice, or snow, each of which have distinct optical depths (measure of attenuation through a medium), single-scatter albedos (incident radiative dispersion for a given wavelength), and asymmetry parameters (scattering ability of a given aerosol); however, for simplification, due to computational restraints, all of the cloud types and their associated properties are amalgamated together into a total cloud fraction Neale et al (2010). To calculate the radiative fluxes and heating rates, CAM5 utilizes the Rapid Radiative Transfer Model for GCMs (RRTMG) scheme which employs broad spectral intervals for both shortwave and longwave radiation on hourly interval frequencies and assumes a Kurucz spectrum to define the solar spectral irradiance (Iacono et al, 2008; Neale et al, 2010). RRTMG accounts for both diurnal and orbital cycles for Earth's eccentricity (orbital shape), precession (axial wobble), and obliquity (axial tilt). With an assumed 1368.22 W/m^2 (this can be adjusted) at the top of the atmosphere, the radiative transfer model divides the solar spectrum into 14 shortwave bands (spanning 0.2 to 12.2 micrometers) that allow extinction (absorption and scattering) to occur from homogeneously mixed layers of oxygen and nitrogen gas, ozone, water, carbon dioxide, methane, clouds, aerosols, and Rayleigh scattering (Neale et al, 2010). Additionally, the RRTMG model only computes shortwave radiation when the sun is above the horizon (or when the cosine of the zenith angle is greater than zero). With all of the aforementioned assumptions, RRTMG has shown accuracy in total radiative flux to 1-2 W/m^2 in clear sky conditions, six W/m^2 for overcast conditions, and two W/m^2 of a more complex and empirically validated model (CHARTS) Neale et al (2010). For longwave calculations, 16 bands are assumed (spanning 3.1 to 1000 micrometers) with absorption possibilities for water, carbon dioxide, methane, ozone, nitrous oxide, chlorofluorocarbons (CFCs - 11 and 12), oxygen and nitrogen gas. A single radiative transfer

angle is assumed (secant = 1.66) for one upward and downward longwave calculation, although the angle can be adjusted if total column water vapor concentrations are sufficiently high (due to the perturbed diffusivity angle). Further, the radiative emissivity is assumed to be one; but, if the radiative surface temperature derived from the upward longwave surface flux calculation in CLM, via the Stefan-Boltzmann equation, is less than one then this alternate value is used. The resultant longwave approximations in the model are accurate to within one W/m^2 of the total vertical column with higher accuracy in the tropospheric cooling rate (within 0.1 K/day) than the stratospheric cooling rate (0.3 K/day) when compared to a more complex line-by-line radiative transfer model, LBLRTM (Neale et al, 2010).

Land-Surface Processes

Land-surface models are diverse in both their complexity and foci. In general, Earth System Models, such as CESM, entrust the land-surface model to couple to the atmospheric model and provide lower boundary conditions/updates for short- and long-wave radiation changes, frictional drag on the wind, carbon/nitrogen cycling, land cover (and albedo) properties, and water budget cycling. The following variables are sent from the atmosphere model to the land model: atmospheric reference height pressure and temperature (a critical quantity in determining the boundary layer height and resultant fluxes between the atmosphere and land surface), zonal/meridional winds, potential temperature, specific humidity, incident short- and long-wave radiation (direct and diffuse), liquid/solid precipitation, carbon, nitrogren, and aerosol species, and lightning frequency (Oleson et al, 2010). Conversely, the land model then sends the following updated variables back to the atmosphere model: latent, sensible, momentum, water vapor, and dust fluxes, emitted and reflected long- and short-wave (both direct and diffuse), absorbed solar radiation, radiative temperature, two-meter surface temperature and specific humidity, snow water equivalent, aerodynmaic resistance, friction velocity, and, lastly, net ecosystem exchange (Oleson et al, 2010). Additionally, recent developments in CLM have resulted in features such as dynamic vegetation cover where the land-surface can iteratively interact with atmospheric forcing, fire ignition, and even human decision making that may lead to modification of the land-surface based on economic and/or rational actor frameworks (Oleson et al, 2010).

To provide the aforementioned updates to the atmospheric model input variables, CLM utilizes a column-based specification routine that breaks each model cell into a unique combination of land unit types including glacier, lake, urban, vegetated, and wetland (Lawrence et al, 2011). The vegetated component of the grid cell is further broken down into various soil types, derived from various USGS products, and 15 unique, plus non-vegetated, Plant Functional Types (PFTs) (Lawrence et al, 2011). CLM4.0 PFTs include five evergreen species and six deciduous species for temperate, boreal, and tropical climates, three grasses for arctic and non-arctic climates (with C-3 and C-4 variations) and a few staple cereal crops (Lawrence et al, 2011). PFT cover is derived from the Moderate Resolution Imaging Spectroradiometer (MODIS) satellite data at $0.5°$ resolution with canopy heights for each of the PFTs assumed to be constant, ranging from 0.5 meters (crops, grasses, and shrubs) to 35 meters (trees) (Lawrence et al, 2011). Broadly, the hydrologic portion of CLM aims to solve the water budget, or precipitation is equal to the sum of evapotranspiration, runoff, and the change in storage (surface and sub-surface). In this process, CLM must differentiate between precipitation phase (rain/snow) and how much of this precipitation is intercepted by the canopy (or stored as snow) as well as how much of the interception/throughfall is absorbed by the soils and inevitably transpired by the vegetation.

The parameterizations of snowpack within CESM's CLM4.0, are based primarily on work done by Anderson (1976), Jordan (1991), and Yongjiu and Qingcun (1997). These parameterizations characterize several important state variables for snowpack including: the mass of water, mass of ice, snowpack layer thickness (up to five individual layers), snow cover extent, temperature profile throughout the total snowpack, black carbon and mineral deposition, and snowpack aging and optical properties (Lawrence et al, 2011). Excitingly, CLM5 (which will be publicly released in 2017) will likely have substantial (and beneficial) changes to the CLM4 hydrology/snow model components, moving it closer to state-of-the-art status (Lawrence and the Land Model Working Group, 2016). These modifications include: the maximum snow layers increased from five to 12, the snow water equivalent cap moved from one meter to 10 meters, the treatment of rainfall/snowfall separately in canopy interception, several wind effect additions (fresh snow density modifications and compaction post-precipitation), and significant upgrades to the hillslope hydrology (Lawrence and the Land Model Working Group, 2016). Fundamentally, CLM (and many other snow models) use

Anderson (1976) as the basis of developing their model variant. The foundational model developed by Anderson (1976) is dependent on its interpretation of the energy balance equation which states that the change in heat storage in the snow cover is equal to the sum of the incoming atmospheric/terrestrial longwave radiation, sensible and latent heat transfer, and the heat transfer due to mass and snow-soil interface minus the sum of the reflected shortwave and emitted longwave radiation by the snow cover. Although seemingly straightforward, the execution of model thresholds in various snow properties aren't. This is largely a result of the various temporal scales at which these processes act, the liquid/ice phasing is somewhat temperature variant (i.e., liquid water and snow can both exist at 0° Celsius) and snow is highly reflective in the shortwave (40-90% reflectance efficiency, based on snow age) yet a blackbody in the longwave (99% absorbance/emittance efficiency) (Anderson, 1976). Furthermore, snowfall and rainfall are sensitive to orographic influence and ground level temperatures, however not always linearly so. This was shown by the U.S. Army Corps of Engineers (1956) which assessed rainfall/snowfall in relation to surface air temperatures in the western USA. They found that typically the rain to snow transition occurs around 1-2° Celsius; however, relatively large variations can occur in phasing where rain was found to occur down to -1 ° Celsius and snow was found to occur up to 4° Celsius. Additionally, the presence of cloud and forest cover can alter this energy balance. For example, a non-forested snow area will have positive net longwave radiation exchanges when the temperature is above freezing and cloudiness is present, yet with no cloud cover the same site will have a net negative longwave exchange until air temperature is above 20-25° Celsius (Anderson, 1976). Additionally, an extensive review of the North American and European snowpack-canopy interaction literature by Varhola et al (2010) showed that snowpack accumulation and melting patterns can be significantly altered by changes in forest cover, accounting for relative variance changes of 57% in snow accumulation and 72% in snow ablation. All of the aforementioned directly effect the snowpack density, reflectance properties, and thus water availability of the snowpack. Thus, CLM's PFT types and percent cover of PFTs within each CLM vegetated land-unit play a crucial role in shaping snowpack trends. As described previously, this is because the interaction between the canopy and snowpack are vegetative species specific for biogeochemical, radiative, and hydrological processes including: interception, throughfall, canopy drip, water removal via transpiration, and optical property interactions based on leaf angle and specific PFT (Lawrence et al, 2011). Therefore, CLM provides a relatively complex representation

of snowpack and its biogeophysical interactions (i.e., canopy cover and storage) within a scalable global climate model framework. As shown by the most recent snow model intercomparison project (SnowMIP2), a comprehensive assessment of 33 snow models (including CLM) with varying complexity and intended development purpose, no model was shown to perform best across a range of discrete locations in the Northern Hemisphere (Essery et al, 2009). Further complications arose in the intercomparison project when canopy interactions were assessed as models performed differently with vegetated and non-vegetated environments. Essery et al (2009) found that a key indicator of more optimal performance in a snow model is its vegetation cover characterization, winter temperature characterization, and performance across a multitude of variables (e.g., snow cover, snow depth, and snow water equivalent). Although bias is prevalent in CLM (as it is in most models), it does account for many of these optimal performance indicators, lending itself to hydroclimate research in western USA mountainous regions.

References

Anderson EA (1976) A point of energy and mass balance model of snow cover. NOAA Tech Rep NWS 19:1–150, doi: http://amazon.nws.noaa.gov/articles/HRL_Pubs_PDF_May12_2009/HRL_PUBS_51-100/81_A_POINT_ENERGY_AND_MASS.pdf

Arakawa A (2004) The Cumulus Parameterization Problem: Past, Present, and Future. Journal of Climate 17(13):2493–2525, doi: 10.1175/1520-0442(2004)017⟨2493:RATCPP⟩2.0.CO;2

Arakawa A, Schubert WH (1974) Interaction of a Cumulus Cloud Ensemble with the Large-Scale Environment, Part I. Journal of the Atmospheric Sciences 31(3):674–701, doi: 10.1175/1520-0469(1974)031⟨0674:IOACCE⟩2.0.CO;2

Ashfaq M, Ghosh S, Kao SC, Bowling LC, Mote P, Touma D, Rauscher SA, Diffenbaugh NS (2013) Near-term acceleration of hydroclimatic change in the western US. Journal of Geophysical Research: Atmospheres 118(19):10–676, doi: 10.1002/jgrd.50816

Bacmeister JT, Wehner MF, Neale RB, Gettelman A, Hannay C, Lauritzen PH, Caron JM, Truesdale JE (2014) Exploratory high-resolution climate simulations using the Community Atmosphere Model (CAM). Journal of Climate 27(9):3073–3099, doi: 10.1175/JCLI-D-13-00387.1

Bales RC, Molotch NP, Painter TH, Dettinger MD, Rice R, Dozier J (2006) Mountain hydrology of the western United States. Water Resources Research 42(8):n/a–n/a, doi: 10.1029/2005WR004387

Bales RC, Battles JJ, Chen Y, Conklin MH, Holst E, OHara KL, Saksa P, Stewart W (2011) Forests and water in the Sierra Nevada: Sierra Nevada watershed ecosystem enhancement project. Sierra Nevada Research Institute report (11.1), URL http://mountaincountieswater.com/wp-content/uploads/2012/03/SWEEP_published_112911.pdf

Bales RC, Rice R, Roy SB (2014) Estimated Loss of Snowpack Storage in the Eastern Sierra Nevada with Climate Warming. Journal of Water Resources Planning and Management 141(2):04014,055, doi: 10.1061/(ASCE)WR.1943-5452.0000453

Barnett TP, Pierce DW, Hidalgo HG, Bonfils C, Santer BD, Das T, Bala G, Wood AW, Nozawa T, Mirin AA, Cayan DR, Dettinger MD (2008) Human-Induced Changes in the Hydrology of the Western United States. Science 319(5866):1080–1083, doi: 10.1126/science.1152538

Bartos MD, Chester MV (2015) Impacts of climate change on electric power supply in the Western United States. Nature Climate Change 5:748–752, doi: 10.1038/nclimate2648

Belmecheri S, Babst F, Wahl ER, Stahle DW, Trouet V (2016) Multi-century evaluation of Sierra Nevada snowpack. Nature Climate Change 6(1):2–3, doi: 10.1038/nclimate2809

Berg N, Hall A, Sun F, Capps S, Walton D, Langenbrunner B, Neelin D (2015) Twenty-First-Century Precipitation Changes over the Los Angeles Region. Journal of Climate 28(2):401–421, doi: 10.1175/JCLI-D-14-00316.1

Berghuijs W, Woods R, Hrachowitz M (2014) A precipitation shift from snow towards rain leads to a decrease in streamflow. Nature Climate Change 4(7):583–586, doi: 10.1038/nclimate2246

Brekke L, Thrasher B, Maurer E, Pruitt T (2013) Downscaled CMIP3 and CMIP5 climate and hydrology projections: Release of downscaled CMIP5 climate projections, comparison with preceding information, and summary of user needs. US Dept of the Interior, Bureau of Reclamation, Technical Services Center, Denver p 47pp, URL http://gdo-dcp.ucllnl.org/downscaled_cmip_projections/techmemo/downscaled_climate.pdf

Cai X, Yang ZL, Xia Y, Huang M, Wei H, Leung LR, Ek MB (2014) Assessment of simulated water balance from Noah, Noah-MP, CLM, and VIC over CONUS using the NLDAS test bed. Journal of Geophysical Research: Atmospheres 119(24):13–751, doi: 10.1002/2014JD022113

Caldwell P (2010) California Wintertime Precipitation Bias in Regional and Global Climate Models. Journal of Applied Meteorology and Climatology 49:2147–2158, doi: 10.1175/2010JAMC2388.1

California Data Exchange Center (CDEC) (accessed 2017) California Department of Water Resources Northern Sierra 8 Station Index. [Available online at http://cdec.water.ca.gov/cgi-progs/precip1/8STATIONHIST]

Cannon AJ, Sobie SR, Murdock TQ (2015) Bias Correction of GCM Precipitation by Quantile Mapping: How Well Do Methods Preserve Changes in Quantiles and Extremes? Journal of Climate 28(17):6938–6959, doi: 10.1175/JCLI-D-14-00754.1

Cayan DR (1996) Interannual climate variability and snowpack in the western United States. Journal of Climate 9(5):928–948, doi: 10.1175/1520-0442(1996)009⟨0928:ICVASI⟩2.0.CO;2

Cayan DR, Redmond KT, Riddle LG (1999) ENSO and Hydrologic Extremes in the Western United States. Journal of Climate 12(9):2881–2893, doi: 10.1175/1520-0442(1999)012⟨2881:EAHEIT⟩2.0.CO;2

Chen F, Dudhia J (2001) Coupling an advanced land surface-hydrology model with the Penn State-NCAR MM5 modeling system. Part I: Model implementation and sensitivity. Monthly Weather Review 129(4):569–585, doi: 10.1175/1520-0493(2001)129⟨0569:CAALSH⟩2.0.CO;2

Chen F, Barlage M, Tewari M, Rasmussen R, Jin J, Lettenmaier D, Livneh B, Lin C, Miguez-Macho G, Niu GY, Wen L, Yang ZL (2014a) Modeling seasonal snowpack evolution in the complex terrain and forested Colorado Headwaters region: A model intercomparison study. Journal of Geophysical Research: Atmospheres 119(24):13,795–13,819, doi: 10.1002/2014JD022167

Chen F, Liu C, Dudhia J, Chen M (2014b) A sensitivity study of high-resolution regional climate simulations to three land surface models over the western United States. Journal of Geophysical Research: Atmospheres 119(12):7271–7291, doi: 10.1002/2014JD021827

Chen J, Brissette FP, Leconte R (2014c) Assessing regression-based statistical approaches for downscaling precipitation over North America. Hydrological Processes 28(9):3482–3504, doi: 10.1002/hyp.9889

Collins WD, Rasch PJ, Boville BA, Hack JJ, McCaa JR, Williamson DL, Kiehl JT, Briegleb B, Bitz C, Lin S (2004) Description of the NCAR community atmosphere model (CAM 3.0). Tech. rep., Tech. Rep. NCAR/TN-464+ STR

Daly C, Halbleib M, Smith JI, Gibson WP, Doggett MK, Taylor GH, Curtis J, Pasteris PP (2008) Physiographically sensitive mapping of climatological temperature and precipitation across the

conterminous United States. International Journal of Climatology 28(15):2031–2064, doi: 10. 1002/joc.1688

Dee D, Uppala S, Simmons A, Berrisford P, Poli P, Kobayashi S, Andrae U, Balmaseda M, Balsamo G, Bauer P, et al (2011) The ERA-Interim reanalysis: Configuration and performance of the data assimilation system. Quarterly Journal of the Royal Meteorological Society 137(656):553–597, doi: 10.1002/qj.828

DeFlorio MJ, Pierce DW, Cayan DR, Miller AJ (2013) Western US extreme precipitation events and their relation to ENSO and PDO in CCSM4. Journal of Climate 26(12):4231–4243, doi: 10.1175/JCLI-D-12-00257.1

Dennis J, Edwards J, Evans KJ, Guba O, Lauritzen PH, Mirin AA, St-Cyr A, Taylor MA, Worley PH (2012) CAM-SE: A scalable spectral element dynamical core for the Community Atmosphere Model. The International Journal of High Performance Computing Applications 26(1):74–89, doi: 10.1177/1094342011428142

Dettinger M (2011) Climate Change, Atmospheric Rivers, and Floods in California - A Multimodel Analysis of Storm Frequency and Magnitude Changes. JAWRA Journal of the American Water Resources Association 47(3):514–523, doi: 10.1111/j.1752-1688.2011.00546.x

Dettinger MD (2013) Atmospheric Rivers as Drought Busters on the U.S. West Coast. Journal of Hydrometeorology 14(6):1721–1732, doi: 10.1175/JHM-D-13-02.1

Dettinger MD, Anderson ML (2015) Storage in California's Reservoirs and Snowpack in this Time of Drought. San Francisco Estuary and Watershed Science 13(2):1–5, URL `http://escholarship.org/uc/item/8m26d692`

Dettinger MD, Cayan DR (1995) Large-scale atmospheric forcing of recent trends toward early snowmelt runoff in California. Journal of Climate 8(3):606–623, doi: 10.1175/1520-0442(1995)008⟨0606:LSAFOR⟩2.0.CO;2

Dettinger MD, Cayan DR, Diaz HF, Meko DM (1998) North-South Precipitation Patterns in Western North America on Interannual-to-Decadal Timescales. Journal of Climate 11(12):3095–3111, doi: 10.1175/1520-0442(1998)011⟨3095:NSPPIW⟩2.0.CO;2

138

Dettinger MD, Ralph FM, Das T, Neiman PJ, Cayan DR (2011) Atmospheric rivers, floods and the water resources of California. Water 3(2):445–478, doi: 10.3390/w3020445

Diffenbaugh NS, Scherer M, Ashfaq M (2013) Response of snow-dependent hydrologic extremes to continued global warming. Nature Climate Change 3(4):379–384, doi: 10.1038/nclimate1732

of Engineers UAC (1956) Snow hydrology: Summary report of the snow investigations. North Pacific Division Portland, OR pp 1–257, URL `https://www.wcc.nrcs.usda.gov/ftpref/wntsc/H&H/snow/SnowHydrologyCOE1956thruCh6.pdf`

Essery R, Rutter N, Pomeroy J, Baxter R, Stähli M, Gustafsson D, Barr A, Bartlett P, Elder K (2009) SNOWMIP2: An evaluation of forest snow process simulations. Bulletin of the American Meteorological Society 90(8):1120–1135, doi: 10.1175/2009BAMS2629.1

Fan J, Liu YC, Xu KM, North K, Collis S, Dong X, Zhang GJ, Chen Q, Kollias P, Ghan SJ (2015) Improving representation of convective transport for scale-aware parameterization: 1. Convection and cloud properties simulated with spectral bin and bulk microphysics. Journal of Geophysical Research: Atmospheres 120(8):3485–3509, doi: 10.1002/2014JD022142

Fang C, Wu L, Zhang X (2014) The impact of global warming on the pacific decadal oscillation and the possible mechanism. Advances in Atmospheric Sciences 31(1):118–130, doi: 10.1007/s00376-013-2260-7

Ferguson JO, Jablonowski C, Johansen H, McCorquodale P, Colella P, Ullrich PA (2016) Analyzing the Adaptive Mesh Refinement (AMR) characteristics of a high-order 2D cubed-sphere shallow-water model. Monthly Weather Review doi: 10.1175/MWR-D-16-0197.1

Field CB, Barros VR, Mastrandrea M, Mach KJ, Abdrabo MK, Adger N, Anokhin Y, Anisimov O, Arent D, Barnett J, et al (2014) Summary for Policymakers. Climate Change 2014: Impacts, Adaptation, and Vulnerability Part A: Global and Sectoral Aspects Contribution of Working Group II to the Fifth Assessment Report of the Intergovernmental Panel on Climate Change pp 1–32, URL `https://www.ipcc.ch/pdf/assessment-report/ar4/wg1/ar4-wg1-spm.pdf`

Fournier A, Taylor MA, Tribbia JJ (2004) The spectral element atmosphere model (SEAM): High-

resolution parallel computation and localized resolution of regional dynamics. Monthly Weather Review 132(3):726–748, doi: 10.1175/1520-0493(2004)132⟨0726:TSEAMS⟩2.0.CO;2

Gates WL (1992) AMIP: The Atmospheric Model Intercomparison Project. Bulletin of the American Meteorological Society 73(12):1962–1970, doi: 10.1175/1520-0477(1992)073⟨1962:ATAMIP⟩2.0.CO;2

Gettelman A, Morrison H, Santos S, Bogenschutz P, Caldwell PM (2015) Advanced Two-Moment Bulk Microphysics for Global Models. Part II: Global Model Solutions and AerosolCloud Interactions. Journal of Climate 28(3):1288–1307, doi: 10.1175/JCLI-D-14-00103.1

Ghan S, Bian X, Hunt A, Coleman A (2002) The thermodynamic influence of subgrid orography in a global climate model. Climate Dynamics 20(1):31–44, doi: 10.1007/s00382-002-0257-5

Ghan SJ, Liu X, Easter RC, Zaveri R, Rasch PJ, Yoon JH, Eaton B (2012) Toward a minimal representation of aerosols in climate models: Comparative decomposition of aerosol direct, semidirect, and indirect radiative forcing. Journal of Climate 25(19):6461–6476, doi: 10.1175/JCLI-D-11-00650.1

Gimeno L, Nieto R, Vázquez M, Lavers DA (2014) Atmospheric rivers: a mini-review. Atmospheric Science 2:2, doi: 10.3389/feart.2014.00002

Giorgi F, Jones C, Asrar GR, et al (2009) Addressing climate information needs at the regional level: the CORDEX framework. World Meteorological Organization (WMO) Bulletin 58(3):175, doi: http://www.cordex.org/images/pdf/cordex_giorgi_wmo.pdf

Glantz MH, Katz RW, Nicholls N (1991) Teleconnections linking worldwide climate anomalies. Cambridge University Press, doi: 10.1002/joc.3370120308

Gross M, Malardel S, Jablonowski C, Wood N (2016) Bridging the (Knowledge) Gap between Physics and Dynamics. Bulletin of the American Meteorological Society 97(1):137–142, doi: 10.1175/BAMS-D-15-00103.1

Gross M, Wan H, Rasch PJ, Caldwell PM, Williamson DL, Klocke D, Jablonowski C, Thatcher DR, Wood N, Cullen M, Beare B, Willett M, Lemarié F, Blayo E, Malardel S, Termonia P, Gassmann

A, Lauritzen PH, Johansen H, Zarzycki CM, Sakaguchi K, Leung R (2016) Recent progress and review of Physics Dynamics Coupling in geophysical models. ArXiv e-prints `1605.06480`

Group MRIEW, et al (2015) Elevation-dependent warming in mountain regions of the world. Nature Climate Change 5(5):424–430, doi: 10.1038/nclimate2563

Groves DG, Yates D, Tebaldi C (2008) Developing and applying uncertain global climate change projections for regional water management planning. Water Resources Research 44(12), doi: 10.1029/2008WR006964

Guan B, Molotch NP, Waliser DE, Fetzer EJ, Neiman PJ (2010) Extreme snowfall events linked to atmospheric rivers and surface air temperature via satellite measurements. Geophysical Research Letters 37(20):n/a–n/a, doi: 10.1029/2010GL044696

Guan B, Molotch NP, Waliser DE, Fetzer EJ, Neiman PJ (2013) The 2010/2011 snow season in california's sierra nevada: Role of atmospheric rivers and modes of large-scale variability. Water Resources Research 49(10):6731–6743, doi: 10.1002/wrcr.20537

Guba O, Taylor MA, Ullrich PA, Overfelt JR, Levy MN (2014) The spectral element method (SEM) on variable-resolution grids: evaluating grid sensitivity and resolution-aware numerical viscosity. Geoscientific Model Development 7(6):2803–2816, doi: 10.5194/gmd-7-2803-2014

Gutzler DS, Robbins TO (2011) Climate variability and projected change in the western united states: regional downscaling and drought statistics. Climate Dynamics 37(5):835–849, doi: 10.1007/s00382-010-0838-7

Hall A (2004) The role of surface albedo feedback in climate. Journal of Climate 17(7):1550–1568, doi: 10.1175/1520-0442(2004)017⟨1550:TROSAF⟩2.0.CO;2

Hall DK, Riggs GA (2007) Accuracy assessment of the MODIS snow products. Hydrological Processes 21(12):1534–1547, doi: 10.1002/hyp.6715

Hall DK, Riggs GA (accessed 2016) MODIS/Terra Snow Cover Monthly L3 Global 0.05Deg CMG, Version 6. doi: http://dx.doi.org/10.5067/MODIS/MOD10CM.006

Hall DK, Riggs GA, Salomonson VV (2006) MODIS snow and sea ice products. In: Earth Science Satellite Remote Sensing: Vol. 1: Science and Instruments, Springer, pp 154–181, doi: 10.1007/978-3-540-37293-6_9

Hanak E, Lund JR (2012) Adapting Californias water management to climate change. Climatic Change 111(1):17–44, doi: 10.1007/s10584-011-0241-3

Hanak E, Lund J, Dinar A, Gray B, Howitt R, Mount J, Moyle P, Thompson B (2011) Managing Californias Water From Conflict to Reconciliation. Public Policy Institute of California (PPIC) URL http://www.ppic.org/content/pubs/report/R_211EHR.pdf

Harris LM, Lin SJ (2013) A Two-Way Nested Global-Regional Dynamical Core on the Cubed-Sphere Grid. Monthly Weather Review 141(1):283–306, doi: 10.1175/MWR-D-11-00201.1

Harris LM, Lin SJ, Tu C (2016) High-Resolution Climate Simulations Using GFDL HiRAM with a Stretched Global Grid. Journal of Climate 29(11):4293–4314, doi: 10.1175/JCLI-D-15-0389.1

Heinzeller D, Duda MG, Kunstmann H (2016) Towards convection-resolving, global atmospheric simulations with the Model for Prediction Across Scales (MPAS) v3.1: an extreme scaling experiment. Geoscientific Model Development 9(1):77–110, doi: 10.5194/gmd-9-77-2016

Henn B, Clark M, Kavetski D, Newman A, Hughes M, McGurk B, Lundquist J (2016) Spatiotemporal patterns of precipitation inferred from streamflow observations across the Sierra Nevada mountain range. Journal of Hydrology doi: 10.1016/j.jhydrol.2016.08.009

Hong SY, Lim JOJ (2006) The WRF single-moment 6-class microphysics scheme (WSM6). Asia-Pacific Journal of Atmospheric Sciences 42(2):129–151, URL http://www2.mmm.ucar.edu/wrf/users/phys_refs/MICRO_PHYS/WSM6.pdf

Hong SY, Noh Y, Dudhia J (2006) A new vertical diffusion package with an explicit treatment of entrainment processes. Monthly Weather Review 134(9):2318–2341, doi: 10.1175/MWR3199.1

Huang X, Ullrich PA (2016) Irrigation impacts on California's climate with the variable-resolution CESM. Journal of Advances in Modeling Earth Systems pp n/a–n/a, doi: 10.1002/2016MS000656

Huang X, Ullrich PA (2017) The changing character of twenty-first century precipitation over the western United States in the variable-resolution CESM. Journal of Climate In Review

Huang X, Rhoades AM, Ullrich PA, Zarzycki CM (2016) An evaluation of the variable-resolution CESM for modeling California's climate. Journal of Advances in Modeling Earth Systems pp n/a–n/a, doi: 10.1002/2015MS000559

Hurrell J, Meehl GA, Bader D, Delworth TL, Kirtman B, Wielicki B (2009) A unified modeling approach to climate system prediction. Bulletin of the American Meteorological Society 90(12):1819, doi: 10.1175/2009BAMS2752.1

Hurrell JW, Hack JJ, Shea D, Caron JM, Rosinski J (2008) A New Sea Surface Temperature and Sea Ice Boundary Dataset for the Community Atmosphere Model. Journal of Climate 21(19):5145–5153, doi: 10.1175/2008JCLI2292.1

Hurrell JW, Holland M, Gent P, Ghan S, Kay J, Kushner P, Lamarque JF, Large W, Lawrence D, Lindsay K, Lipscomb W, Long M, Mahowald N, Marsh D, Neale R, Rasch P, Vavrus S, Vertenstein M, Bader D, Collins W, Hack J, Kiehl J, Marshall S (2013) The community Earth system model: A framework for collaborative research. Bulletin of the American Meteorological Society 94:1339–1360, doi: 10.1175/BAMS-D-12-00121.1

Iacono MJ, Delamere JS, Mlawer EJ, Shephard MW, Clough SA, Collins WD (2008) Radiative forcing by long-lived greenhouse gases: Calculations with the AER radiative transfer models. Journal of Geophysical Research: Atmospheres 113(D13):n/a–n/a, doi: 10.1029/2008JD009944

Iorio JP, Duffy PB, Govindasamy B, Thompson SL, Khairoutdinov M, Randall D (2004) Effects of model resolution and subgrid-scale physics on the simulation of precipitation in the continental united states. Climate Dynamics 23(3):243–258, doi: 10.1007/s00382-004-0440-y

J L Kinter I, Cash B, Achuthavarier D, Adams J, Altshuler E, Dirmeyer P, Doty B, Huang B, Jin EK, Marx L, Manganello J, Stan C, Wakefield T, Palmer T, Hamrud M, Jung T, Miller M, Towers P, Wedi N, Satoh M, Tomita H, Kodama C, Nasuno T, Oouchi K, Yamada Y, Taniguchi H, Andrews P, Baer T, Ezell M, Halloy C, John D, Loftis B, Mohr R, Wong K (2013) Revolutionizing

Climate Modeling with Project Athena: A Multi-Institutional, International Collaboration. Bulletin of the American Meteorological Society 94(2):231–245, doi: 10.1175/BAMS-D-11-00043.1

Jordan R (1991) A one-dimensional temperature model for a snow cover: Technical documentation for SNTHERM. 89. Tech. rep., U.S. Army Corps of Engineers, URL `http://acwc.sdp.sirsi.net/client/en_US/search/asset/1011960;jsessionid=C717289426C0CE377628C955142D6D5C.enterprise-15000`

Kain JS (2004) The Kain-Fritsch convective parameterization: an update. Journal of Applied Meteorology 43(1):170–181, doi: 10.1175/1520-0450(2004)043⟨0170:TKCPAU⟩2.0.CO;2

Kapnick S, Hall A (2010) Observed ClimateSnowpack Relationships in California and their Implications for the Future. Journal of Climate 23:3446–3456, doi: http://dx.doi.org/10.1175/2010JCLI2903.1

Kapnick S, Hall A (2012) Causes of recent changes in western North American snowpack. Climate Dynamics 38(9):1885–1899, doi: 10.1007/s00382-011-1089-y

Kay JE, Deser C, Phillips A, Mai A, Hannay C, Strand G, Arblaster JM, Bates SC, Danabasoglu G, Edwards J, Holland M, Kushner P, Lamarque JF, Lawrence D, Lindsay K, Middleton A, Munoz E, Neale R, Oleson K, Polvani L, Vertenstein M (2015) The Community Earth System Model (CESM) Large Ensemble Project: A Community Resource for Studying Climate Change in the Presence of Internal Climate Variability. Bulletin of the American Meteorological Society 96(8):1333–1349, doi: 10.1175/BAMS-D-13-00255.1

Klos PZ, Link TE, Abatzoglou JT (2014) Extent of the rain-snow transition zone in the western U.S. under historic and projected climate. Geophysical Research Letters 41(13):4560–4568, doi: 10.1002/2014GL060500, 2014GL060500

Lawrence D, the Land Model Working Group (2016) Update on CLM5 progress. 2016 WINTER WG MEETING PRESENTATIONS - LMWG and BCGWG URL `https://www2.cesm.ucar.edu/events/meetings/20160208/presentations/lmwg-bcgwg`

Lawrence DM, Oleson KW, Flanner MG, Thornton PE, Swenson SC, Lawrence PJ, Zeng X, Yang ZL, Levis S, Sakaguchi K, Bonan GB, Slater AG (2011) Parameterization improvements and func-

tional and structural advances in version 4 of the Community Land Model. Journal of Advances in Modeling Earth Systems 3(1):n/a–n/a, doi: 10.1029/2011MS00045

Leung LR, Ghan SJ (1998) Parameterizing subgrid orographic precipitation and surface cover in climate models. Monthly Weather Review 126(12):3271–3291, doi: 10.1175/1520-0493(1998) 126⟨3271:PSOPAS⟩2.0.CO;2

Leung LR, Ringler T, Collins WD, Taylor M, Ashfaq M (2013) A Hierarchical Evaluation of Regional Climate Simulations. Eos, Transactions American Geophysical Union 94(34):297–298, doi: 10.1002/2013EO340001

Li R, Wang SY, Gillies RR (2016) A combined dynamical and statistical downscaling technique to reduce biases in climate projections: an example for winter precipitation and snowpack in the western united states. Theoretical and Applied Climatology 124(1):281–289, doi: 10.1007/s00704-015-1415-0

Li W, Forest CE (2014) Estimating the sensitivity of the atmospheric teleconnection patterns to SST anomalies using a linear statistical method. Journal of Climate 27(24):9065–9081, doi: 10.1175/JCLI-D-14-00231.1

Lute AC, Abatzoglou JT, Hegewisch KC (2015) Projected changes in snowfall extremes and inter-annual variability of snowfall in the western United States. Water Resources Research 51(2):960–972, doi: 10.1002/2014WR016267

Margulis SA, Corts G, Girotto M, Durand M (2016a) A Landsat-Era Sierra Nevada Snow Reanalysis (1985-2015). Journal of Hydrometeorology 17(4):1203–1221, doi: 10.1175/JHM-D-15-0177.1

Margulis SA, Corts G, Girotto M, Huning LS, Li D, Durand M (2016b) Characterizing the extreme 2015 snowpack deficit in the Sierra Nevada (USA) and the implications for drought recovery. Geophysical Research Letters pp n/a–n/a, doi: 10.1002/2016GL068520, 2016GL068520

Maurer E, Hidalgo H, Das T, Dettinger M, Cayan D (2010) Assessing climate change impacts on daily streamflow in California: the utility of daily large-scale climate data. Hydrology and Earth System Sciences Discussions 7(1):1209–1243, doi: 10.5194/hess-14-1125-2010

Maurer EP, Hidalgo HG (2008) Utility of daily vs. monthly large-scale climate data: an intercomparison of two statistical downscaling methods. Hydrology and Earth System Sciences 12(2):551–563, doi: 10.5194/hess-12-551-2008

Maurer EP, Brekke L, Pruitt T, Duffy PB (2007) Fine-resolution climate projections enhance regional climate change impact studies. Eos, Transactions American Geophysical Union 88(47):504–504, doi: 10.1029/2007EO470006

McCorquodale P, Ullrich P, Johansen H, Colella P (2014) An adaptive multiblock high-order finite-volume method for solving the shallow-water equations on the sphere. Communications in Applied Mathematics and Computer Science 10(2):121–162, doi: 10.2140/camcos.2015.10.121

McFarlane N (1987) The Effect of Orographically Excited Gravity Wave Drag on the General Circulation of the Lower Stratosphere and Troposphere. Journal of the Atmospheric Sciences 44(14):1775–1800, doi: 10.1175/1520-0469(1987)044⟨1775:TEOOEG⟩2.0.CO;2

Mearns LO, Gutowski WJ, Jones R, Leung R, McGinnis S, Nunes A, Qian Y (2009) A regional climate change assessment program for North America. EoS 90(36):311–312, doi: 10.1029/2009EO360002

Mearns LO, Arritt R, Biner S, Bukovsky MS, McGinnis S, Sain S, Caya D, Jr JC, Flory D, Gutowski W, Takle ES, Jones R, Leung R, Moufouma-Okia W, McDaniel L, Nunes AMB, Qian Y, Roads J, Sloan L, Snyder M (2012) The North American Regional Climate Change Assessment Program: Overview of Phase I Results. Bulletin of the American Meteorological Society 93(9):1337–1362, doi: 10.1175/BAMS-D-11-00223.1

Mearns LO, Sain S, Leung LR, Bukovsky MS, McGinnis S, Biner S, Caya D, Arritt RW, Gutowski W, Takle E, Snyder M, Jones RG, Nunes AMB, Tucker S, Herzmann D, McDaniel L, Sloan L (2013) Climate change projections of the North American Regional Climate Change Assessment Program (NARCCAP). Climatic Change 120(4):965–975, doi: 10.1007/s10584-013-0831-3

Menne, MJ, I Durre, RS Vose, BE Gleason, and TG Houston (2012) Global Historical Climatology Network - Daily (GHCN-Daily), Version 3.22. doi: http://doi.org/10.7289/V5D21VHZ, [assessed 2016 at `https://www.ncdc.noaa.gov/cdo-web/`]

Mesinger F, DiMego G, Kalnay E, Mitchell K, Shafran PC, Ebisuzaki W, Jovic D, Woollen J, Rogers E, Berbery EH, Ek MB, Fan Y, Grumbine R, Higgins W, Li H, Lin Y, Manikin G, Parrish D, Shi W (2006) North American Regional Reanalysis. Bulletin of the American Meteorological Society 87(3):343–360, doi: 10.1175/BAMS-87-3-343

Montoya E, Dozier J, Meiring W (2014) Biases of April 1 snow water equivalent records in the Sierra Nevada and their associations with large-scale climate indices. Geophysical Research Letters 41(16):5912–5918, doi: 10.1002/2014GL060588

Morrison H, Gettelman A (2008) A new two-moment bulk stratiform cloud microphysics scheme in the Community Atmosphere Model, version 3 (CAM3). Part I: Description and numerical tests. Journal of Climate 21(15):3642–3659, doi: 10.1175/2008JCLI2105.1

Mote PW (2003) Trends in snow water equivalent in the Pacific Northwest and their climatic causes. Geophysical Research Letters 30(12):n/a–n/a, doi: 10.1029/2003GL017258

Mote PW, Hamlet AF, Clark MP, Lettenmaier DP (2005) Declining mountain snowpack in Western North America. Bulletin of the American Meteorological Society 86(1):39–49, doi: 10.1175/ BAMS-86-1-39

National Climate Assessment (accessed 2016) Southwest. [Available online at `http://nca2014.globalchange.gov/report/regions/southwest`]

National Geophysical Data Center (2006) 2-minute Gridded Global Relief Data (ETOPO2) v2. National Geophysical Data Center, NOAA. Doi: 10.7289/V5J1012Q [2014]

Neale RB, Richter JH, Jochum M (2008) The impact of convection on ENSO: From a delayed oscillator to a series of events. Journal of Climate 21(22):5904–5924, doi: 10.1175/2008JCLI2244.1

Neale RB, Chen CC, Gettelman A, Lauritzen PH, Park S, Williamson DL, Conley AJ, Garcia R, Kinnison D, Lamarque JF, Marsh D, Mills M, Smith AK, Tilmes S, Vitt F, Cameron-Smith P, Collins WD, Iacono MJ, , Easter RC, Liu X, Ghan SJ, Rasch PJ, Taylor MA (2010) Description of the NCAR Community Atmosphere Model (CAM 5.0). NCAR Technical Note NCAR/TN-486+STR, National Center for Atmospheric Research, Boulder, Colorado

O'Brien TA, Collins WD, Kashinath K, Rbel O, Byna S, Gu J, Krishnan H, Ullrich PA (2016) Resolution dependence of precipitation statistical fidelity in hindcast simulations. Journal of Advances in Modeling Earth Systems 8(2):976–990, doi: 10.1002/2016MS000671

Oleson K, Lawrence D, Bonan G, Flanner M, Kluzek E, Lawrence P, Levis S, Swenson S, Thornton P, Dai A, Decker M, Dickinson R, Feddema J, Heald C, Hoffman F, Lamarque J, Mahowald N, Niu G, Qian T, Randerson J, Running S, Sakaguchi K, Slater A, Stockli R, Wang A, Yang Z, Zeng X, Zeng X (2010) Technical Description of version 4.0 of the Community Land Model (CLM). NCAR Technical Note NCAR/TN-478+STR, National Center for Atmospheric Research, Boulder, Colorado, doi: 10.5065/D6FB50WZ

Painter TH, Berisford DF, Boardman JW, Bormann KJ, Deems JS, Gehrke F, Hedrick A, Joyce M, Laidlaw R, Marks D, Mattmann C, McGurk B, Ramirez P, Richardson M, Skiles SM, Seidel FC, Winstral A (2016) The airborne snow observatory: Fusion of scanning lidar, imaging spectrometer, and physically-based modeling for mapping snow water equivalent and snow albedo. Remote Sensing of Environment 184:139 – 152, doi: 10.1016/j.rse.2016.06.018

Palmer PL (1988) The SCS snow survey water supply forecasting program: Current operations and future directions pp 43–51, URL https://westernsnowconference.org/sites/westernsnowconference.org/PDFs/1988Palmer.pdf

Pandey GR, Cayan DR, Georgakakos KP (1999) Precipitation structure in the Sierra Nevada of California during winter. Journal of Geophysical Research: Atmospheres (1984–2012) 104(D10):12,019–12,030

Park S, Bretherton CS (2009) The University of Washington shallow convection and moist turbulence schemes and their impact on climate simulations with the Community Atmosphere Model. Journal of Climate 22(12):3449–3469, doi: 10.1175/2008JCLI2557.1

Park S, Bretherton CS, Rasch PJ (2014a) Integrating cloud processes in the Community Atmosphere Model, Version 5. Journal of Climate 27(18):6821–6856, doi: 10.1175/JCLI-D-14-00087.1

Park SH, Klemp JB, Skamarock WC (2014b) A Comparison of Mesh Refinement in the Global

MPAS-A and WRF Models Using an Idealized Normal-Mode Baroclinic Wave Simulation. Monthly Weather Review 142(10):3614–3634, doi: 10.1175/MWR-D-14-00004.1

Pavelsky TM, Kapnick S, Hall A (2011) Accumulation and melt dynamics of snowpack from a multiresolution regional climate model in the central Sierra Nevada, California. Journal of Geophysical Research: Atmospheres 116, doi: 10.1029/2010JD015479

Pavelsky TM, Sobolowski S, Kapnick SB, Barnes JB (2012) Changes in orographic precipitation patterns caused by a shift from snow to rain. Geophysical Research Letters 39, doi: 10.1029/2012GL052741

Pierce DW, Cayan DR (2013) The uneven response of different snow measures to human-induced climate warming. Journal of Climate 26(12):4148–4167, doi: 10.1175/JCLI-D-12-00534.1

Pierce DW, Das T, Cayan DR, Maurer EP, Miller NL, Bao Y, Kanamitsu M, Yoshimura K, Snyder MA, Sloan LC, et al (2013) Probabilistic estimates of future changes in California temperature and precipitation using statistical and dynamical downscaling. Climate Dynamics 40(3-4):839–856, doi: 10.1007/s00382-012-1337-9

Pierce DW, Cayan DR, Maurer EP, Abatzoglou JT, Hegewisch KC (2015) Improved Bias Correction Techniques for Hydrological Simulations of Climate Change. Journal of Hydrometeorology 16(6):2421–2442, doi: 10.1175/JHM-D-14-0236.1

Qian Y, Ghan SJ, Leung LR (2010) Downscaling hydroclimatic changes over the Western US based on CAM subgrid scheme and WRF regional climate simulations. International journal of climatology 30(5):675–693, doi: 10.1002/joc.1928

Qu X, Hall A (2014) On the persistent spread in snow-albedo feedback. Climate Dynamics 42(1-2):69–81, doi: 10.1007/s00382-013-1774-0

Quaas J (2012) Evaluating the critical relative humidity as a measure of subgrid-scale variability of humidity in general circulation model cloud cover parameterizations using satellite data. Journal of Geophysical Research: Atmospheres 117(D9):n/a–n/a, doi: 10.1029/2012JD017495

Raleigh MS, Rittger K, Moore CE, Henn B, Lutz JA, Lundquist JD (2013) Ground-based testing of MODIS fractional snow cover in subalpine meadows and forests of the Sierra Nevada. Remote Sensing of Environment 128:44 – 57, doi: http://dx.doi.org/10.1016/j.rse.2012.09.016

Ralph FM, Neiman PJ, Wick GA (2004) Satellite and CALJET aircraft observations of atmospheric rivers over the eastern North Pacific Ocean during the winter of 1997/98. Monthly Weather Review 132(7):1721–1745, doi: http://dx.doi.org/10.1175/1520-0493(2004)132⟨1721:SACAOO⟩2.0.CO;2

Randall D, Khairoutdinov M, Arakawa A, Grabowski W (2003) Breaking the Cloud Parameterization Deadlock. Bulletin of the American Meteorological Society 84(11):1547–1564, doi: 10.1175/BAMS-84-11-1547

Rauscher SA, Ringler TD (2014) Impact of Variable-Resolution Meshes on Midlatitude Baroclinic Eddies Using CAM-MPAS-A. Monthly Weather Review 142(11):4256–4268, doi: http://dx.doi.org/10.1175/MWR-D-13-00366.1

Rauscher SA, Ringler TD, Skamarock WC, Mirin AA (2013) Exploring a Global Multiresolution Modeling Approach Using Aquaplanet Simulations. Journal of Climate 26(8):2432–2452, doi: http://dx.doi.org/10.1175/JCLI-D-12-00154.1

Reed DA, Dongarra J (2015) Exascale computing and big data. Commun ACM 58(7):56–68, doi: 10.1145/2699414

Rhoades AM, Huang X, Ullrich PA, Zarzycki CM (2016) Characterizing Sierra Nevada Snowpack Using Variable-Resolution CESM. Journal of Applied Meteorology and Climatology 55(1):173–196, doi: 10.1175/JAMC-D-15-0156.1

Rhoades AM, Ullrich PA, Zarzycki CM (2017) Projecting 21st Century Snowpack Trends in Western USA Mountains Using Variable-Resolution CESM. Climate Dynamics Accepted

Rupp DE, Mote PW, Bindoff NL, Stott PA, Robinson DA (2013) Detection and attribution of observed changes in Northern Hemisphere spring snow cover. Journal of Climate 26(18):6904–6914, doi: 10.1175/JCLI-D-12-00563.1

Saha S, Moorthi S, Wu X, Wang J, Nadiga S, Tripp P, Behringer D, Hou YT, Chuang Hy, Iredell M, et al (2014) The NCEP climate forecast system version 2. Journal of Climate 27(6):2185–2208, doi: http://dx.doi.org/10.1175/JCLI-D-12-00823.1

Sakaguchi K, Leung LR, Zhao C, Yang Q, Lu J, Hagos S, Rauscher SA, Dong L, Ringler TD, Lauritzen PH (2015) Exploring a Multiresolution Approach Using AMIP Simulations. Journal of Climate 28(14):5549–5574, doi: 10.1175/JCLI-D-14-00729.1

Salzmann N, Mearns LO (2012) Assessing the performance of multiple regional climate model simulations for seasonal mountain snow in the upper Colorado River basin. Journal of Hydrometeorology 13(2):539–556, doi: 10.1175/2011JHM1371.1

Schulzweida U, Kornblueh L, Quast R (2007) CDO User's Guide–Climate Data Operators. Tech. rep., Max Planck Institute, version 1.0.7, Tech. rep., online available at: `www.mpimet.mpg.de/fileadmin/software/cdo`

Seaber PR, Kapinos FP, Knapp GL (1987) Hydrologic unit maps. U.S. Geological Survey, URL `https://pubs.usgs.gov/of/1984/0708/report.pdf`

Serreze MC, Clark MP, Armstrong RL, McGinnis DA, Pulwarty RS (1999) Characteristics of the western United States snowpack from snowpack telemetry (SNOTEL) data. Water Resources Research 35(7):2145–2160, doi: 10.1029/1999WR900090

Skamarock WC, Klemp JB, Duda MG, Fowler LD, Park SH, Ringler TD (2012) A Multiscale Non-hydrostatic Atmospheric Model Using Centroidal Voronoi Tesselations and C-Grid Staggering. Monthly Weather Review 140(9):3090–3105, doi: 10.1175/MWR-D-11-00215.1

Small RJ, Bacmeister J, Bailey D, Baker A, Bishop S, Bryan F, Caron J, Dennis J, Gent P, Hsu Hm, Jochum M, Lawrence D, Muoz E, diNezio P, Scheitlin T, Tomas R, Tribbia J, Tseng Yh, Vertenstein M (2014) A new synoptic scale resolving global climate simulation using the Community Earth System Model. Journal of Advances in Modeling Earth Systems 6(4):1065–1094, doi: 10.1002/2014MS000363

Stewart IT (2009) Changes in snowpack and snowmelt runoff for key mountain regions. Hydrological Processes 23(1):78–94, doi: 10.1002/hyp.7128

Stewart WC (1996) Economic Assessment of the Ecosystem. Sierra Nevada Ecosystem Project: Final Report to Congress 3:973–1064, doi: https://pubs.usgs.gov/dds/dds-43/VOL_III/VIII_C23.PDF

Sun F, Hall A, Schwartz M, BWalton D, Berg N (2016) Twenty-First-Century Snowfall and Snowpack Changes over the Southern California Mountains. Journal of Climate 29(1):91–110, doi: 10.1175/JCLI-D-15-0199.1

Tanaka SK, Zhu T, Lund JR, Howitt RE, Jenkins MW, Pulido MA, Tauber M, Ritzema RS, Ferreira IC (2006) Climate warming and water management adaptation for California. Climatic Change 76(3-4):361–387, doi: 10.1007/s10584-006-9079-5

Tao WK, Lau W, Simpson J, Chern JD, Atlas R, Randall D, Khairoutdinov M, Li JL, Waliser DE, Jiang J, Hou A, Lin X, Peters-Lidard C (2009) A Multiscale Modeling System: Developments, Applications, and Critical Issues. Bulletin of the American Meteorological Society 90(4):515–534, doi: 10.1175/2008BAMS2542.1

Taylor KE, Stouffer RJ, Meehl GA (2012) An overview of CMIP5 and the experiment design. Bulletin of the American Meteorological Society 93(4):485–498, doi: http://dx.doi.org/10.1175/BAMS-D-11-00094.1

Taylor M, Tribbia J, Iskandarani M (1997) The Spectral Element Method for the Shallow Water Equations on the Sphere. Journal of Computational Physics 130:92–108, doi: 10.1006/jcph.1996.5554

Taylor MA, Fournier A (2010) A compatible and conservative spectral element method on unstructured grids. Journal of Computational Physics 229(17):5879–5895, doi: 10.1016/j.jcp.2010.04.008

Thornton P, Thornton M, Mayer B, Wilhelmi N, Wei Y, Devarakonda R, Cook R (2014) Daymet: Daily Surface Weather Data on a 1-km Grid for North America, Version 2. Data set. Available on-line [http://daac. ornl. gov] from Oak Ridge National Laboratory Distributed Active Archive Center, Oak Ridge, Tennessee, USA. Date accessed: 2014/11/01. Temporal range: 1980-2005. Tech. rep., http://dx. doi. org/10.3334/ORNLDAAC/1219

Toure AM, Rodell M, Yang ZL, Beaudoing H, Kim E, Zhang Y, Kwon Y (2016) Evaluation of the Snow Simulations from the Community Land Model, Version 4 (CLM4). Journal of Hydrometeorology 17(1):153–170, doi: 10.1175/JHM-D-14-0165.1

Ullrich (2014) SQuadGen: Spherical Quadrilateral Grid Generator. [Available online at `http://climate.ucdavis.edu/squadgen.php`]

Ullrich PA, Taylor MA (2015) Arbitrary-Order Conservative and Consistent Remapping and a Theory of Linear Maps: Part I. Monthly Weather Review 143(6):2419–2440, doi: 10.1175/MWR-D-14-00343.1

Ullrich PA, Devendran D, Johansen H (2016) Arbitrary-order conservative and consistent remapping and a theory of linear maps, Part 2. Monthly Weather Review 144(4):1529–1549, doi: 10.1175/MWR-D-15-0301.1

Varhola A, Coops NC, Weiler M, Moore RD (2010) Forest canopy effects on snow accumulation and ablation: An integrative review of empirical results. Journal of Hydrology 392(3):219–233, doi: 10.1016/j.jhydrol.2010.08.009

Velázquez JA, Troin M, Caya D, Brissette F (2015) Evaluating the Time-Invariance Hypothesis of Climate Model Bias Correction: Implications for Hydrological Impact Studies. Journal of Hydrometeorology 16(5):2013–2026, doi: 10.1175/JHM-D-14-0159.1

Wallace JM, Gutzler DS (1981) Teleconnections in the geopotential height field during the Northern Hemisphere winter. Monthly Weather Review 109(4):784–812, doi: 10.1175/1520-0493(1981)109⟨0784:TITGHF⟩2.0.CO;2

Wang SY, Hipps L, Gillies RR, Yoon JH (2014) Probable causes of the abnormal ridge accompanying the 2013–2014 California drought: ENSO precursor and anthropogenic warming footprint. Geophysical Research Letters 41(9):3220–3226, doi: 10.1002/2014GL059748

Wehner MF, Bala G, Duffy P, Mirin AA, Romano R (2010) Towards direct simulation of future tropical cyclone statistics in a high-resolution global atmospheric model. Advances in Meteorology 2010:1–13, doi: http://dx.doi.org/10.1155/2010/915303

Wehner MF, Reed KA, Li F, Bacmeister J, Chen CT, Paciorek C, Gleckler PJ, Sperber KR, Collins WD, Gettelman A, et al (2014) The effect of horizontal resolution on simulation quality in the Community Atmospheric Model, CAM5. Journal of Advances in Modeling Earth Systems 6:980–997, doi: 10.1002/2013MS000276

Weisman ML, Skamarock WC, Klemp JB (1997) The Resolution Dependence of Explicitly Modeled Convective Systems. Monthly Weather Review 125(4):527–548, doi: 10.1175/1520-0493(1997) 125⟨0527:TRDOEM⟩2.0.CO;2

van der Wiel K, Kapnick SB, Vecchi GA, Cooke WF, Delworth TL, Jia L, Murakami H, Underwood S, Zeng F (2016) The Resolution Dependence of Contiguous U.S. Precipitation Extremes in Response to CO2 Forcing. Journal of Climate 29(22):7991–8012, doi: 10.1175/JCLI-D-16-0307.1

Wise EK (2012) Hydroclimatology of the US Intermountain West. Progress in Physical Geography 36:458–479, doi: 10.1177/0309133312446538

Xia Y, Mitchell K, Ek M, Cosgrove B, Sheffield J, Luo L, Alonge C, Wei H, Meng J, Livneh B, et al (2012a) Continental-scale water and energy flux analysis and validation for North American Land Data Assimilation System project phase 2 (NLDAS-2): 2. Validation of model-simulated streamflow. Journal of Geophysical Research: Atmospheres 117(D3), doi: 10.1029/2011JD016051

Xia Y, Mitchell K, Ek M, Sheffield J, Cosgrove B, Wood E, Luo L, Alonge C, Wei H, Meng J, et al (2012b) Continental-scale water and energy flux analysis and validation for the North American Land Data Assimilation System project phase 2 (NLDAS-2): 1. Intercomparison and application of model products. Journal of Geophysical Research: Atmospheres 117(D3), doi: 10.1029/2011JD016048

Yang Q, Ruby Leung L, Lu J, Lin YL, Hagos S, Sakaguchi K, Gao Y (2017) Exploring the effects of a nonhydrostatic dynamical core in high-resolution aquaplanet simulations. Journal of Geophysical Research: Atmospheres pp n/a–n/a, doi: 10.1002/2016JD025287, 2016JD025287

Yang ZLY, Cai X, Zhang G, Tavakoly AA, Jin Q, Meyer LH, Guan X (2011) Technical Description of the Community Noah Land Surface Model with Multi-Paramterization Options (Noah-MP).

Tech. rep., Center for Integrated Earth System Science, The University of Texas at Austin, Boulder, Colorado, URL `http://www.jsg.utexas.edu/noah-mp/files/Noah-MP_Technote_v0.2.pdf`

Yen YC (1965) Heat transfer characteristics of naturally compacted snow. Tech. rep., Cold Regions Research and Engineering Laboratory, URL `https://erdc-library.erdc.dren.mil/xmlui/bitstream/handle/11681/5734/CRREL-Research-Report-166.pdf?sequence=1&isAllowed=y`

Yongjiu D, Qingcun Z (1997) A land surface model (IAP94) for climate studies part I: formulation and validation in off-line experiments. Advances in Atmospheric Sciences 14:433–460, doi: 10.1007/s00376-997-0063-4

Zarzycki CM (2016) Tropical cyclone intensity errors associated with lack of two-way ocean coupling in high-resolution global simulations. Journal of Climate 29(23):8589–8610, doi: 10.1175/JCLI-D-16-0273.1

Zarzycki CM, Jablonowski C (2014) A multidecadal simulation of Atlantic tropical cyclones using a variable-resolution global atmospheric general circulation model. Journal of Advances in Modeling Earth Systems 6(3):805–828, doi: 10.1002/2014MS000352

Zarzycki CM, Jablonowski C, Taylor MA (2014a) Using Variable Resolution Meshes to Model Tropical Cyclones in the Community Atmosphere Model. Monthly Weather Review 142(3):1221–1239, doi: 10.1175/MWR-D-13-00179.1

Zarzycki CM, Levy MN, Jablonowski C, Overfelt JR, Taylor MA, Ullrich PA (2014b) Aquaplanet Experiments Using CAM's Variable-Resolution Dynamical Core. Journal of Climate 27:5481–5503, doi: 10.1175/JCLI-D-14-00004.1

Zarzycki CM, Jablonowski C, Thatcher DR, Taylor MA (2015) Effects of Localized Grid Refinement on the General Circulation and Climatology in the Community Atmosphere Model. Journal of Climate 28(7):2777–2803, doi: 10.1175/JCLI-D-14-00599.1

Zarzycki CM, Reed KA, Bacmeister JT, Craig AP, Bates SC, Rosenbloom NA (2016) Impact of

surface coupling grids on tropical cyclone extremes in high-resolution atmospheric simulations. Geoscientific Model Development 9(2):779–788, doi: 10.5194/gmd-9-779-2016

Zender CS (2008) Analysis of self-describing gridded geoscience data with netCDF Operators (NCO). Environmental Modelling & Software 23(10):1338–1342, doi: 10.1016/j.envsoft.2008.03.004

Zhang GJ, McFarlane NA (1995) Sensitivity of climate simulations to the parameterization of cumulus convection in the Canadian Climate Centre general circulation model. Atmosphere-ocean 33(3):407–446, doi: http://dx.doi.org/10.1080/07055900.1995.9649539